Cosmic Bays, at Large Zenith iVngles.

Pattinison, J. B. M.

Abstract

The sea-level momentum spectrum and positive-negative ratio of cosmic ray muons incident at large zenith angles have been measured with a spectrograph comprising Geiger counters, neon flash-tubes and a solid iron magnet.

Precise differential momentum spectra have been derived in the momentum range 3 - 550 GeV/c over the zenith angular range $77.5^{\circ} - 90^{\circ}$. In the lower momentum region, 5-44 GeV/c, there is good agreement with the spectrum determined with the earlier Geiger counter spectrograph. Refined methods of measurement of the flash tube data for particles with momentum greater than 50 GeV/c lead to a maximum detectable momentum of the instrument, based on the probable error of deflection measurements, of (369 ± 16) GeV/c.

The positive-negative ratio of muons at production has been found to be consistent with the results of similar experiments in the vertical direction in that the charge ratio does not tend to unity at least before several hundred GeV/c, indicating that the fluctuation in the multiplicity of high energy collisions increases with increasing energy.

A determination is made of the expected ratio of the production spectra of muons from K-mesons and pions and this is compared with the measured ratios. No evidence is found for K-mesons playing an important role in the production of muons of energies above 100 GeV.

At low energies, the statistical accuracy of the measurements is too low to permit a conclusion to be drawn about the importance of

Frontispiece; The Durham Cosmic Ray Horizontal Spectrograph.

Cosmic Rays at Large Zenith Angles.

by J. B. M. Pattison, B.Sc.

A thesis submitted to the University of Durham, on an application for the degree of Master of Science.

August, 1963.

Contents

Page

Abstract

The sea-level momentum spectrum and positive-negative ratio of cosmic ray muons incident at large zenith angles have been measured with a spectrograph comprising Geiger counters, neon flash-tubes and a solid iron magnet.

Precise differential momentum spectra have been derived in the momentum range 3 - 550 GeV/c over the zenith angular range 77.5°-90°. In the lower momentum region, 5-44 GeV/c, there is good agreement with the spectrum determined with the earlier Geiger counter spectrograph. Refined methods of measurement of the flash tube data for particles with momentum greater than 50 GeV/c lead to a maximum detectable momentum of the instrument, based on the probable error of deflection measurements, of (369 ± 16) GeV/c.

The positive-negative ratio of muons at production has been found to be consistent with the results of similar experiments in the vertical direction in that the charge ratio does not tend to unity at least before several hundred GeV/c, indicating that the fluctuation in the multiplicity of high energy collisions increases with increasing energy.

A determination is made of the expected ratio of the production spectra of muons from K-mesons and pions and this is compared with the measured ratios. No evidence is found for K-mesons playing an important role in the production of muons of energies above 100 GeV.

At low energies, the statistical accuracy of the measurements is too low to permit a conclusion to be drawn about the importance of

K-meson production; it is found that the muon spectra at low energies are comparatively insensitive to the nature of the parent particles and very high statistical accuracy would be required in order to make an estimate of K-meson production.

The measurements have been combined with other data and used to estimate the ratio of production of charged K-mesons to pions in proton-air nucleus collisions and it is found that the upper limit of this ratio falls from 0.65 at a proton energy of 10^3 GeV to 0.2 at 2.10^4 GeV. It is concluded that there is no evidence for a rapid increase in the K/π ratio over a range of primary proton energies extending from a few GeV to some 500,000 GeV, and that the ratio is probably less than 0.4 over all energy ranges.

PREFACE

This thesis describes the work done by the author in the Cosmic Radiation Group of the Physics Department in the Durham Colleges, under the supervision of Dr. A. W. Wolfendale.

Whilst the recipient of a research studentship from the European Office, Aerospace Research, United States Air Force, the author was responsible for the second version of the Durham Cosmic Ray Horizontal Spectrograph by the addition of arrays of neon flash-tubes.

In addition to the construction of the mechanical and optical systems the author was responsible for the alignment of the instrument, its operation and the derivation of the muon spectrum at large zenith angles. The measurement of events was supervised by the author and the analysis was carried out jointly by Dr. F. Ashton and the author.

The final momentum spectra and the positive-negative ratios obtained from the data and their interpretation were reported briefly at the Conference on Ultra High Energy Nuclear Physics held at Bristol in January, 1963. A paper on the positive-negative ratio has been submitted by the author and his colleagues to Physics Letters.

Chapter I

INTRODUCTION

1.1 History of Cosmic Ray Research

Some sixty years ago it was shown that, in a closed vessel shielded from local radioactivity, there was a residual production of about two ions per second per cubic centimetre of air. In later experiments, balloons carrying ionization chambers showed evidence of an increase in this residual ionization above a height of about 700 metres from ground level, there having been a slight decrease up to this height. The decrease up to 700 metres could have been due to the reduction in effect of the earth's radioactivity, but the increase above this height could only be due to a radiation penetrating the earth's atmosphere from outside. That there was no significant diurnal variation in ionization pointed to the fact that the bulk of this radiation was not of solar origin, but originated further afield in the galaxy or indeed was of extra-galactic origin. Bothe and Kolhörster pointed out that if the radiation, which soon became known as the Cosmic Radiation, contained charged particles, the earth's magnetic field would prevent the less energetic particles from reaching equatorial regions, giving rise to a variation in intensity as a function of geomagnetic latitude, and successful experiments were carried out demonstrating that this is indeed the case. Recent rocket and balloon flights show that the primary flux (i.e. the flux outside the earth's atmosphere) of the cosmic radiation consists of 85-88% hydrogen nuclei (i.e. protons), $\sim$10% helium nuclei

(α-particles) and 1 or 2% of nuclei with $Z > 2$ up to Fe^{26}. It appears that the primary radiation is almost isotropic, the small anisotropies which arise being due to the effect of the earth's magnetic field and some solar effects.

1.2 Origin of Primary Cosmic Rays

Increases in the cosmic ray intensity have been observed at periods of intense solar flares indicating that here there is a mechanism for accelerating particles to the order of 10^{10} eV (10 GeV) in, or near, the sun. It is also known, however, that there are primaries of energies up to 10^{20} eV, these particles having been observed indirectly by a study of extensive air showers. Richtmeyer and Teller considered the problem of a storage mechanism, and concluded that such very energetic particles emitted by the sun could become isotropic after about 10^3 to 10^8 years. However, a grave problem arises: if one considers the usual relationship between the energy E eV of a particle of charge Z in a magnetic field H gauss then the radius of curvature ρ of the particle's orbit is given by

$$\frac{E}{Z} = 300\ H\rho$$

If the solar field $H = 10^{-5}$ gauss, and an orbit equal to twice the distance of Pluto, the outermost planet ($\rho = 10^{15}$ cm), is taken then

$$\frac{E}{Z} = 3 \times 10^{12}\ \text{eV}.$$

This, obviously, is far below the energy of the most energetic particle detected to date. The only possibility is an enhancement of particles of high Z, which is not shown to be the case. It is therefore thought that the more energetic primaries are of galactic origin on the basis

Type of particle	Symbol	Rest mass (m_e)	Principal Modes of Decay	Relative abundance of alternative decay modes	Lifetime secs.
Photon	γ	0	Stable	-	
Neutrino	$\nu(\bar{\nu})$	0	Stable	-	
Electron	$e^{\pm}$	1	Stable	-	
Mu-meson	$\mu^{\pm}$	206.9	$\mu^{\pm} \to e^{\pm} + \nu + \bar{\nu}$	-	$(2.212 \pm 0.001) \times 10^{-6}$
Pi-meson	$\pi^{\pm}$	273.2	$\pi^{+} \to \mu^{+} + \nu$	1	
			$\to e^{+} + \nu$	10^{-4}	$(2.55 \pm 0.03) \times 10^{-8}$
			$\pi^{-} \to \mu^{-} + \bar{\nu}$		
	π^{0}	264	$\pi^{0} \to \gamma + \gamma$	98.8%	$(2.2 \pm 0.8) \times 10^{-16}$
			$\to \gamma + e^{+} + e^{-}$	1.2%	
			$\to 2e^{+} + 2e^{-}$	~0.004%	

Table 1.1 The properties of leptons and π-mesons

Type of particle	Symbol	Rest mass (m_e)	Principal Modes of Decay	Relative abundance of alternative decay modes	Lifetime secs.
K-mesons (charged)	$K^{\pm}$	967	$K^+ \to \mu^+ + \nu$	58% ($K_{\mu 2}$)	$(1.22 \pm 0.013) \times 10^{-8}$
			$\to \pi^+ + \pi^0$	26% ($K_{\pi 2}$)	
			$\to \pi^+ + \pi^+ + \pi^-$	6% ($K_{\pi 3}$)	
			$\to \pi^+ + \pi^0 + \pi^0$	2% ($K_{\pi 3}$)	
			$\to \mu^+ + \pi^0 + \nu$	4% ($K_{\mu 3}$)	
			$\to e^+ + \pi^0 + \nu$	~4% ($K_{\beta 3}$)	

K^- decays in similar modes to K^+ with appropriate anti-particle as decay products

Type of particle	Symbol	Rest mass (m_e)	Principal Modes of Decay	Relative abundance of alternative decay modes	Lifetime secs.
K-meson (neutral)	K_1^0	973	$K_1^0 \to \pi^+ + \pi^-$	34.5%	$(1.000 \pm 0.038) \times 10^{-10}$
			$\to \pi^0 + \pi^0$	15.5%	
	K_2^0	973	$K_2^0 \to \pi^+ + \mu^- + \bar{\nu}$	16%	$6.1(+1.6/-1.1) \times 10^{-8}$
			$\to \pi^- + \mu^+ + \nu$		
			$\to \pi^+ + e^- + \bar{\nu}$	17%	
			$\to \pi^- + e^+ + \nu$		
			$\to \pi^+ + \pi^- + \pi^0$	6.5%	
			$\to \pi^0 + \pi^0 + \pi^0$	~10.5%	

$\bar{K}^0$ decays in similar modes to K^0

Table 1.2 The properties of $\bar{K}$-mesons

Type of particle	Symbol	Rest mass (m_e)	Principal Modes of Decay	Relative abundance of alternative decay modes	Lifetime secs.
Proton	$p(\bar{p})$	1836	Stable		
Neutron	$n(\bar{n})$	1839	$n \rightarrow e^- + p + \bar{\nu}$		$(1.013 \pm 0.029) \times 10^{+3}$
Lambda-Hyperon	$\Lambda^0(\bar{\Lambda}^0)$	2182	$\Lambda^0 \rightarrow p + \pi^-$	65%	$(2.51 \pm 0.09) \times 10^{-10}$
			$\rightarrow n + \pi^0$	35%	
Sigma-Hyperon	$\Sigma^+(\bar{\Sigma}^+)$	2328	$\Sigma^+ \rightarrow n + \pi^+$	~50%	$8.1(+0.6/-0.5) \times 10^{-11}$
			$\rightarrow p + \pi^0$	~ 50%	
	$\Sigma^-(\bar{\Sigma}^-)$	2342	$\Sigma^- \rightarrow n + \pi^-$		$1.61(+0.1/-0.09) \times 10^{-10}$
	$\Sigma^0(\bar{\Sigma}^0)$	2326	$\Sigma^0 \rightarrow \Lambda^0 + \gamma$		$<10^{-11}$
Xi-Hyperon	$\Xi^-(\bar{\Xi}^-)$	2585	$\Xi^- \rightarrow \Lambda^0 + \pi^-$		$1.28(+0.38/-0.30) \times 10^{-10}$
	$\Xi^0(\bar{\Xi}^0)$	2571	$\Xi^0 \rightarrow \Lambda^0 + \pi^0$		$\sim 1.5 \times 10^{-10}$ (1 event)

Table 1.3 The properties of Baryons

of this argument, and that there is also a contribution from outside the galaxy.

The composite theory due to Cocconi and Morrison (cf Handbuch der Physik, Vol. 46/1, page 1, 1961) is regarded as the most promising at the present time. Essentially, it postulates that there are three main sources of cosmic rays, giving rise to various energy bands, as follows:

(i) Low energy ($<10^{13}$eV) particles originate in the spiral arms of the galaxy. (i.e. within $\sim$1000 light years from the solar system),

(ii) Particles of medium energy (10^{13} - 10^{16}eV) come from the galaxy as a whole, arising mainly from regions of high density near the galactic centre (remembering that the diameter of the galaxy is $\sim$50,000 light years and that the solar system is some 33,000 light years from the galactic centre). These particles diffuse into the halo and are 'reflected' isotropically,

and (iii)High energy ($>10^{16}$eV) particles originate outside the galaxy.

On entering the earth's atmosphere the primary cosmic rays can interact with the nuclei of the atmosphere, in particular the nuclei of oxygen and nitrogen, producing secondary particles such as π-mesons (the most common secondaries), K-mesons, nucleons, and the other baryons. The properties of the various elementary particles are shown in Tables 1.1, 1.2, 1.3 (after Powell et al). It is seen that most of them are unstable, decaying with a certain characteristic lifetime. It is of interest to note that some of these particles (for example, the K-mesons) have alternative modes of decay. Where this occurs the branching ratio

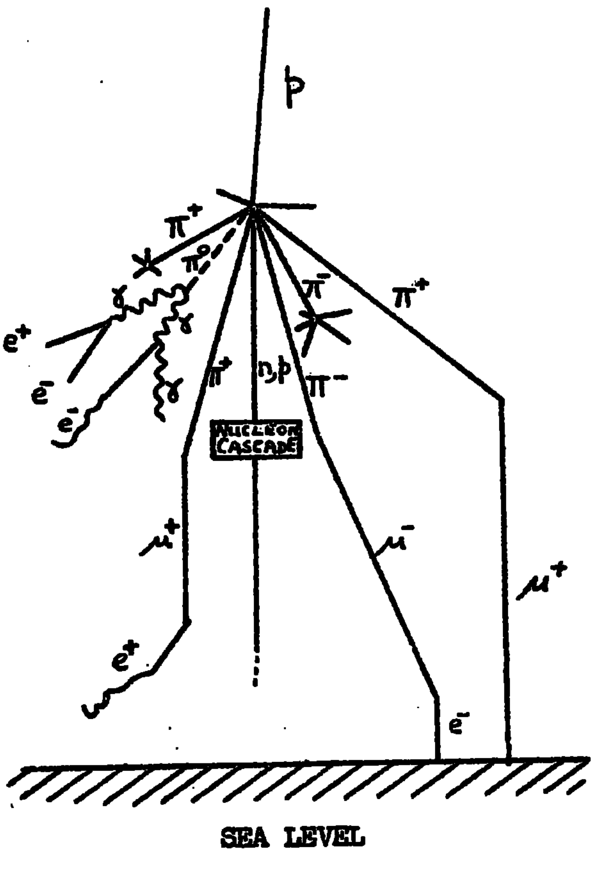

Fig. 1.1 The propagation of Cosmic Rays through the atmosphere.

for each mode is shown. One further important observation to be made from this table is that the K-mesons, Λ-hyperons, Σ and Ξ baryons can all decay either directly or indirectly to charged π-mesons (or pions) which have the μ-meson (or muon) as the predominant decay product. The result is that the muon is the most common cosmic ray particle at ground level.

It is with the μ-meson component at ground level that the work described in this thesis is concerned.

1.3 Propagation through the atmosphere

As mentioned in section 1.2, the particles comprising the primary flux of the cosmic radiation have a certain probability of undergoing collisions with a nucleus of oxygen or nitrogen, the result of which is the production of secondary particles. The primary particles and pions are strongly interacting particles and their numbers are attenuated exponentially in the atmosphere with an attenuation length of about 120 $gm.cm^{-2}$. Since the vertical thickness of the atmosphere is 1033 $gm\ cm^{-2}$ it will be appreciated that the intensity of primaries and of secondary pions will fall rapidly as one proceeds down through the atmosphere. A typical sequence of events is shown in figure 1.1. The primary particle considered will be of energy $\sim$ 50 GeV. A variety of particles are produced in this first interaction. Two positive pions are shown to decay into positive muons (each associated with a neutrino, not shown). One of these muons survives to sea level without decaying whereas the slower muon decays into a positron (and two neutrinos, not shown). On the other hand the third positive pion and the negative pion interact with an air nucleus emitting further secondaries. The neutral pion decays very rapidly into two photons, one of which materializes into an electron-positron pair, whilst the other undergoes Compton scattering. These electrons and photons cascade down through the atmosphere producing a cascade of electrons and photons. For higher primary energies, the number of particles becomes very great and the event is known as an extensive air shower. Lastly, the primary particle continues as either a proton or neutron depending on the type of interaction. This nucleon cascades down through the atmosphere producing further interactions.

1.4 The sea-level component at large zenith angles

If one now considers the sea-level flux of particles at large zenith angles (i.e. near the horizontal) consideration of interaction and decay lengths of particles shows that the only particles arriving are muons and the 'tails' of extensive air showers. This is mainly due to the fact that the thickness of the atmosphere from a point on the earth and in a tangential direction is 36,000 $gm.cm^{-2}$, i.e. some 36 times that in the vertical direction. Here, therefore, is an excellent opportunity for a determination of the sea level intensity of high energy μ-mesons without having to go underground and having recourse to the somewhat uncertain range-energy relations in determining the sea-level intensity.

The usual method of measuring spectra is by the use of a magnetic lens (cf chapter 2) with detectors above and below the magnet. Extremely high energoes can only be measured by making the arms of such magnet spectrographs quite long or by using very high magnetic fields. The latter being very difficult it is therefore a case of having spectrographs of large longitudinal dimensions. Obviously this can be more easily achieved using a "horizontal" spectrograph. As pointed out above, another advantage of studying particles at large zenith angles is that one has a pure beam of muons, thus enabling the interactions of high energy muons to be studied at the same time as the momentum measurements are made, by "parasite" equipment.

Whilst there have been many precise measurements of the vertical cosmic ray intensity at sea-level, there have only been a few attempts at large zenith angles (i.e. $\gtrsim 60^{\circ}$). It has been shown that the intensity at large zenith angles should exceed that in the vertical direction at very high energy. For example, whereas at 100 GeV/c the ratio of vertical muon intensity to that at 90° zenith angle is expected to be 8.04, at 350 GeV/c it is unity and at 1000 GeV/c the ratio is 0.32 (i.e. the 90° intensity exceeds the vertical intensity by a factor 3.1). This emphasises the fact that in order to study very energetic muons it is better to work at large zenith angles rather than in the vertical direction.

When an analysis is made of the propagation of the various cosmic ray components through the atmosphere, it is found that the sea-level muon flux is sensitive to the mass and lifetime of the parent particles, and one of the objects of the present investigation is to attempt to identify the parent particle (i.e. whether it is the π-meson or the K-meson, the other heavier hyperons and baryons being thought to be unlikely).

Starting with the measured vertical muon spectrum as a datum, the sea-level intensities of muons at large zenith angles are predicted from a knowledge of the pion production spectrum assuming that all muons are the decay products of pions. A similar prediction is made assuming the K-meson to be the producing particle. This meson has several modes of decay, the most important of which is the mode

$$K_{\mu 2} \rightarrow \mu + \nu$$

with a lifetime of 1.22 x 10^{-8}sec.

These predicted spectra are then compared with experimental results and conclusions made as to the origin of muons.

As mentioned above it is an obvious consequence that such a horizontal spectrograph will be useful as a "source" of a clean beam of fast muons which can be used to study interactions in targets placed at the output end of the instrument and consideration is given to the "accelerator characteristics" of the spectrograph. It is in this respect that for many years to come this type of instrument will reign supreme over the largest particle accelerators, the biggest of which is the proton-synchrotron at the European Organization for Nuclear Research (C.E.R.N.) in Geneva, accelerating protons to 30 GeV. A 2 GeV muon beam is being built at the present time at this machine but this is extremely low in comparison to cosmic ray energies!

A discussion follows in chapter 2 of the design and construction of the horizontal spectrograph, details of the magnetic induction measurements, the neon flash tube characteristics, the electronics and the method of alignment. The measuring techniques are considered in chapter 3, where the basic data are to be found. Consideration also is given there to the use of the instrument as a source of high energy muons for studies of the interactions of muons. The acceptance characteristics and the theoretical momentum spectra are considered in chapter 4 and the momentum spectra derived for various zenith angular ranges are given in chapter 5. The positive-negative ratio is then derived from the measured data. Finally, the interpretation of the present results as regards the origin of the sea-level muon flux at large zenith angles is given in chapter 6, and mention is made of future work with the instruments.

Chapter II

THE SPECTROGRAPH

2.1 Introduction

Previous techniques available for measuring the sea-level flux have involved the determination of range, multiple scattering or momentum. A great disadvantage in obtaining the sea-level flux of cosmic rays by minimum ranges in condensed materials or multiple scattering in nuclear emulsions or multiplate cloud chambers is that the maximum detectable momentum (m.d.m.) is quite low ($\sim$10 GeV/c) in comparison to cosmic ray energies. (In the relativistic region, momentum and energy are numerically equal since in the relation

$$E^2 = m^2c^4 + p^2c^2$$

where m, E, p are respectively the mass, energy and momentum of the particle in question,

$$m^2c^4 \ll p^2c^2$$

and therefore $E \approx pc$.)

Further, a theory of the range-energy relationship etc. must be known, reducing the accuracy of determining particle energies.

The most widely used technique for determining particle momenta is that of magnetic deflection. Most previous workers have deflected the particles in the gap of a large electromagnet, the particles being detected by either counter controlled cloud chambers or Geiger counter hodoscopes. For example Pine et al (1959) used three cloud chambers, controlled by Geiger counter arrays, in the Cornell spectrograph, the geometry of the cloud chambers being one above and one below the electromagnet with the third chamber in the magnetic field. This arrangement gave an m.d.m. of 176 GeV/c. Holmes et al (1961) using two electromagnets and three cloud chambers in the Manchester spectrograph obtained an m.d.m. of 356 GeV/c. In more recent work Hayman et al (1962) using the Durham vertical spectrograph have incorporated an array of "Conversi" tubes (now more usually called "neon flash tubes") with an electromagnet. Using very refined measuring techniques these workers have obtained an m.d.m. of 657 $\pm$ 112 GeV/c.

The work to be described here is a study of the cosmic ray flux at large zenith angles at Durham (latitude 54°47'N, longitude 1°35'W, 200 feet above sea-level). Because of the closeness of Durham to sea-level this flux will often be referred to as the sea-level flux. As previously mentioned the great thickness of atmosphere in inclined directions filters out virtually all particles except the mu-meson. Since the mu-meson (or muon) is of the leptonic class (i.e. it has a very small cross-section for interaction with matter) and the rate of events would be expected to be considerably lower at large zenith angles than in the vertical direction, it was decided to deflect the particles in magnetized iron as distinct from the gap of an air-cored magnet. Obvious advantages are seen immediately in that the collecting volume can be made very large and high inductions can be achieved for low powers of excitation. This principle was first used by Rossi (1931), and later by Bernardini et al (1945) and Conversi et al (1945) who all used magnetic lenses to separate positive and negative mesons; the present work, however, seems to be the first to develop the technique of the 'solid iron magnet' for the precise determination of particle momenta.

Although the probability of a muon suffering a large deflection through it's short range interaction with nuclei is small, there will be a finite deflection in a thick absorber resulting from multiple Coulomb scattering. This results in a limit being set to the accuracy with which the momentum of a single particle may be determined. Although the root mean square angle of scatter increases with length of trajectory, L, as $L^{\frac{1}{2}}$, the magnetic deflection increases at a faster rate, proportional to L, and the fractional error in momentum falls accordingly as $L^{-\frac{1}{2}}$. In practice, then, L is made as large as possible.

Previous work with this instrument (Ashton and Wolfendale 1963) used a Geiger counter hodoscope but this has now been considerably improved by the addition of an array of flash tubes.

2.2 The Magnet

The magnet construction is described by O'Connor and Wolfendale (1960), but since it has been moved to the new laboratory entailing dismantling and reassembling with new windings, extensive measurements have been made to measure the magnetic induction.

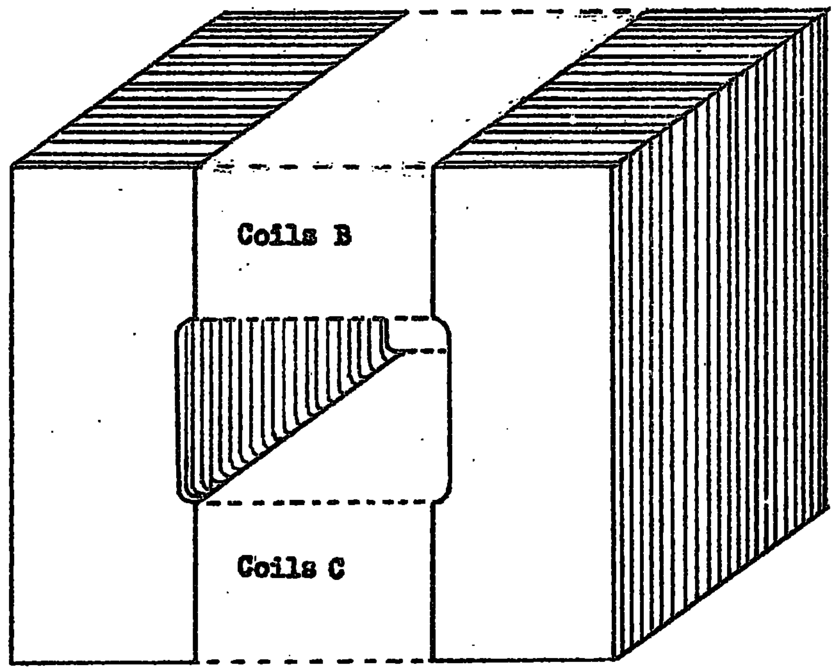

Fig. 2.1 The solid iron magnet.

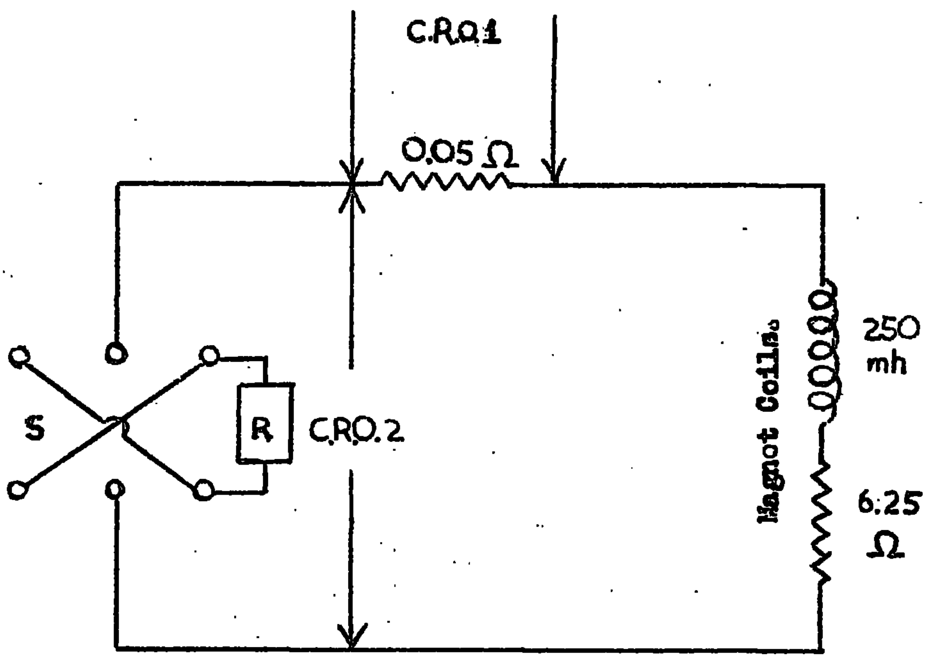

Fig.2.2 Circuit used to examine the characteristics of the power supply to the magnet coils.(R is the rectifier, and S the reversing switch.)

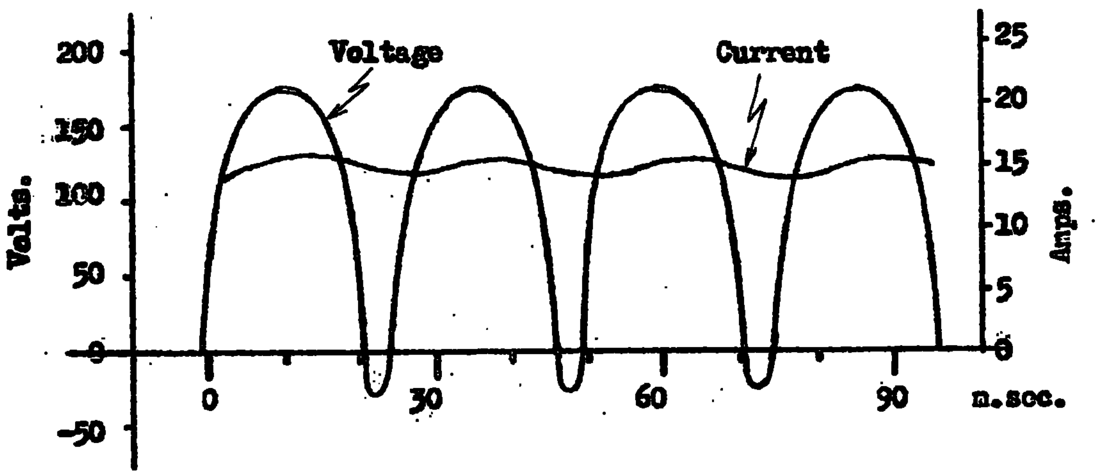

Fig.2.3 Characteristics of the current and voltage supplies to the magnet windings.

The fifty laminations are mounted vertically in an iron framework and are held in the vertical position by two horizontal steel pegs through opposite corners. The coils consist of 250 turns of 14 SWG double cotton covered copper wire on each of the yokes B and C (cf fig. 2.1). The total resistance is 6.25 ohms when cold and the self-inductance 250 mH. In the previous arrangement of O'Connor and Wolfendale the coils were split to enable search coils to be inserted at the centre of the deflecting volume, but in the present arrangement the coils are continuous. Current is supplied to the coils by a mains rectifier, and a reversing switch is incorporated for field reversals.

2.2(a) Characteristics of the power supply to the magnet windings

A standard resistance of value 0.05 ohm was placed in series with the magnet windings (fig. 2.2) and a double beam oscilloscope used to examine the current (C.R.O.1) and voltage (C.R.O.2) supplies. The resulting display is shown in fig. 2.3.

In the study state it was seen that the current lags behind the voltage by ~ 3 m sec. and that the r.m.s. variation of the ripple in the excitation current is 3.4%, corresponding to a variation in induction of 0.6%.

It was also observed that when the current supply to the magnet coils was switched on and off at the reversing switch, the rise and decay times to two-thirds and one-third peak height were one second and a tenth of a second respectively. This was, by far, much quicker than

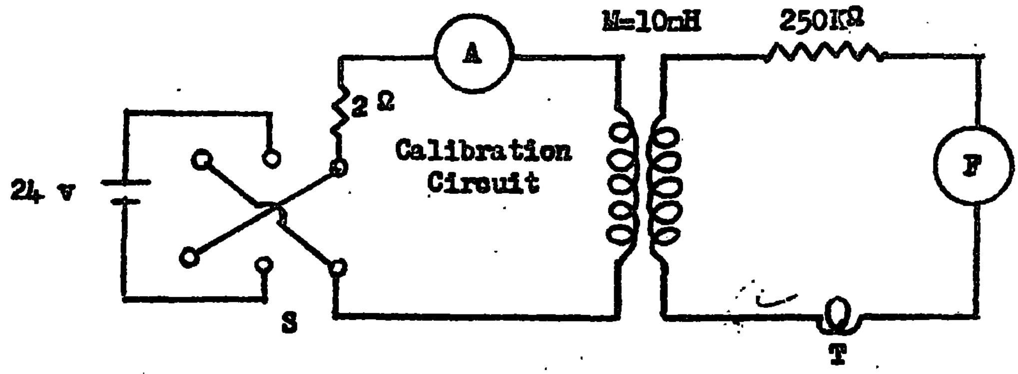

Fig. 2.4 Circuit used to calibrate the fluxmeter F and measure the magnetic induction. (S is the reversing switch).

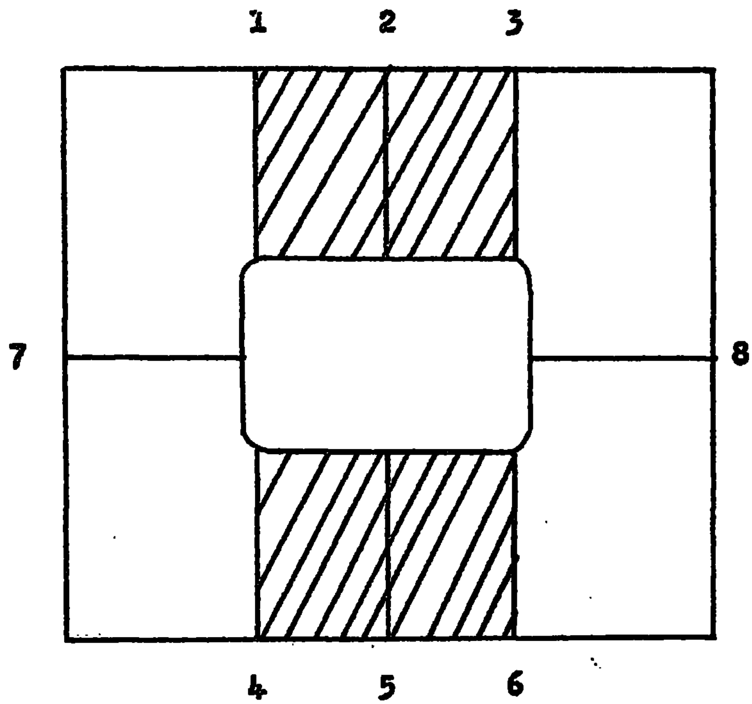

Position	B (K gauss)
1	15.04
2	15.48
3	14.97
4	15.37
5	15.38
6	15.32
7	14.92
8	15.09

Fig. 2.5 The measured magnetic inductions as a function of position on the solid iron magnet.

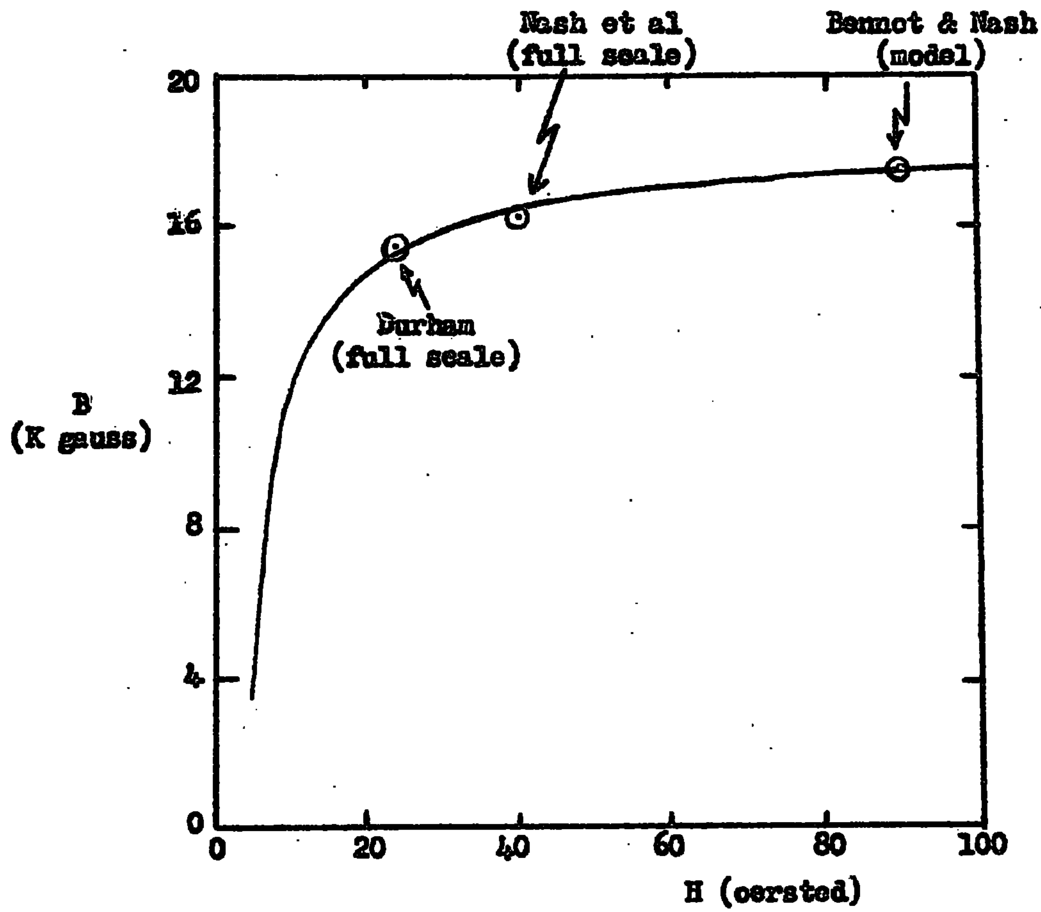

Fig. 2.6 Comparison of the operating values for the various solid iron magnets.

when the rectifier was controlled at the mains switch, the corresponding times being 1.9 and 1.3 seconds respectively. Compared with the period of the Cambridge Fluxmeter used (40 and 34 seconds when in circuit and out of circuit respectively) this is ideal for induction measurements.

2.2(b) Measurement of the magnetic induction

In order to measure the magnetic induction, the circuit shown in fig. 2.4 was used, T being a single turn of wire wrapped round the magnetized iron in various places (fig. 2.5 not to scale). The measured inductions are also shown in fig. 2.5. Good agreement (.06%) was obtained when the measurements were checked using a variable inductometer in place of the 10 m H mutual inductance. A comparison of the operating values for the various solid iron magnets is shown in fig. 2.6.

2.3 The Neon Flash Tubes

A brief summary of the characteristics of the neon flash tubes is shown in figures 2.7, 2.8, 2.9, and Table 2.1 (Coxell Ph.D. Thesis). The tubes used in the apparatus were $\sim$ 80 cm. in length, and 1.5 cm. in diameter containing neon (98% Ne, 2% He, $<$ 200 vpm A, O_2, N_2) to a pressure of about 60 cm. They were painted black, except for the plane end window, with a lower white layer over the 20 cm. nearest the window. As can be seen from the figures 2.7 to 2.9 and Table 2.1 the necessary conditions for maximum efficiency and visibility are:

(i) The highest voltage pulse consistent with an insignificant rate of spurious flashing.

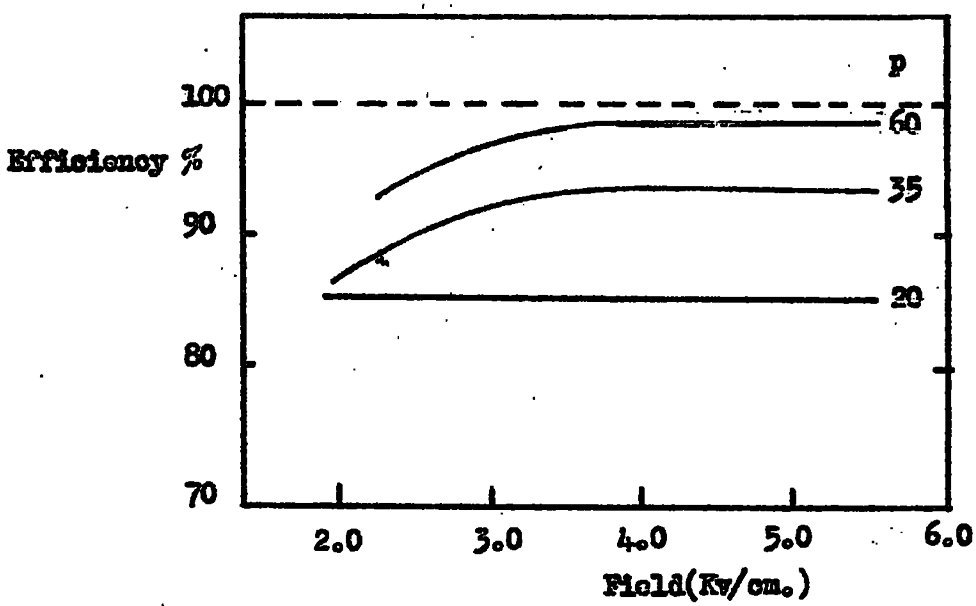

Fig. 2.7(a) The efficiency, field characteristics, with gas pressure (cm.Hg) as parameter. T_D=3.2 μsec, T_R= 0.5 μsec, τ = 4 μsec.

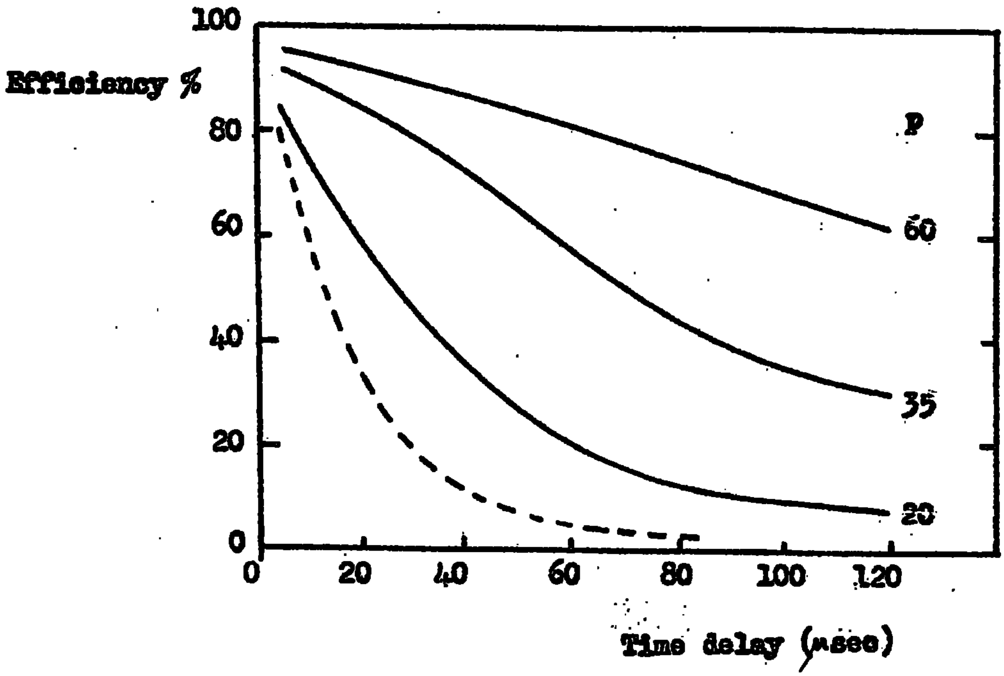

Fig. 2.7(b) The efficiency, time delay characteristics, with gas pressure (cm.Hg) as parameter. E_{max} = 3.7 Kv/cm, T_R= 0.5 μsec, τ = 4 μsec.
(Dotted line: p= 60 cm.Hg, clearing field = 3.6 Kv/cm.)

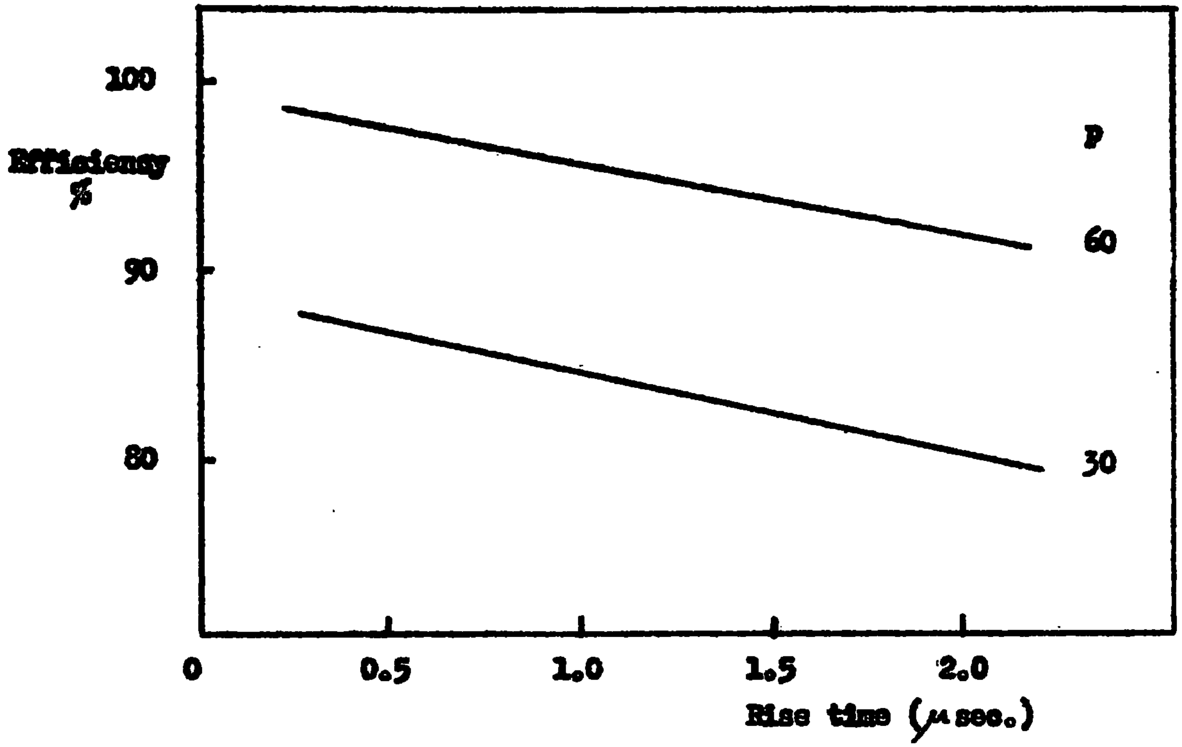

Fig. 2.8 (a) The efficiency, rise time characteristic, with gas pressure (cm.Hg)as parameter. E_{max} = 3.0 Kv/cm, T_D = 3.2 μsec, τ = 4 μsec.

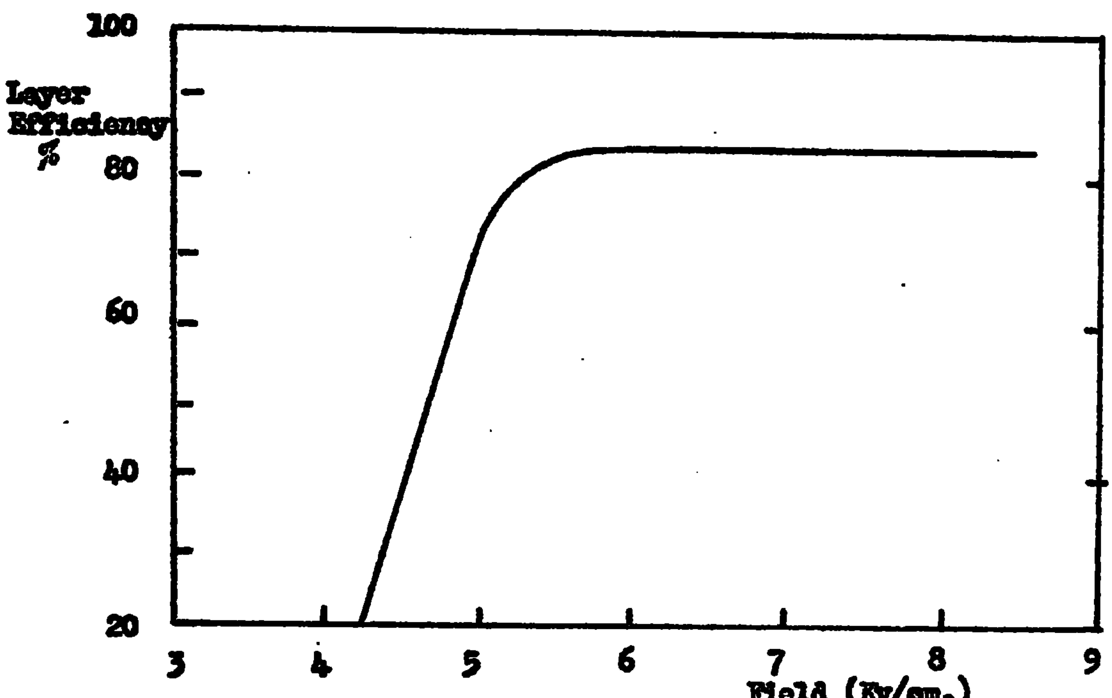

Fig 2.8 (b) The layer efficiency, field characteristics for the tubes used in the horizontal spectrograph.

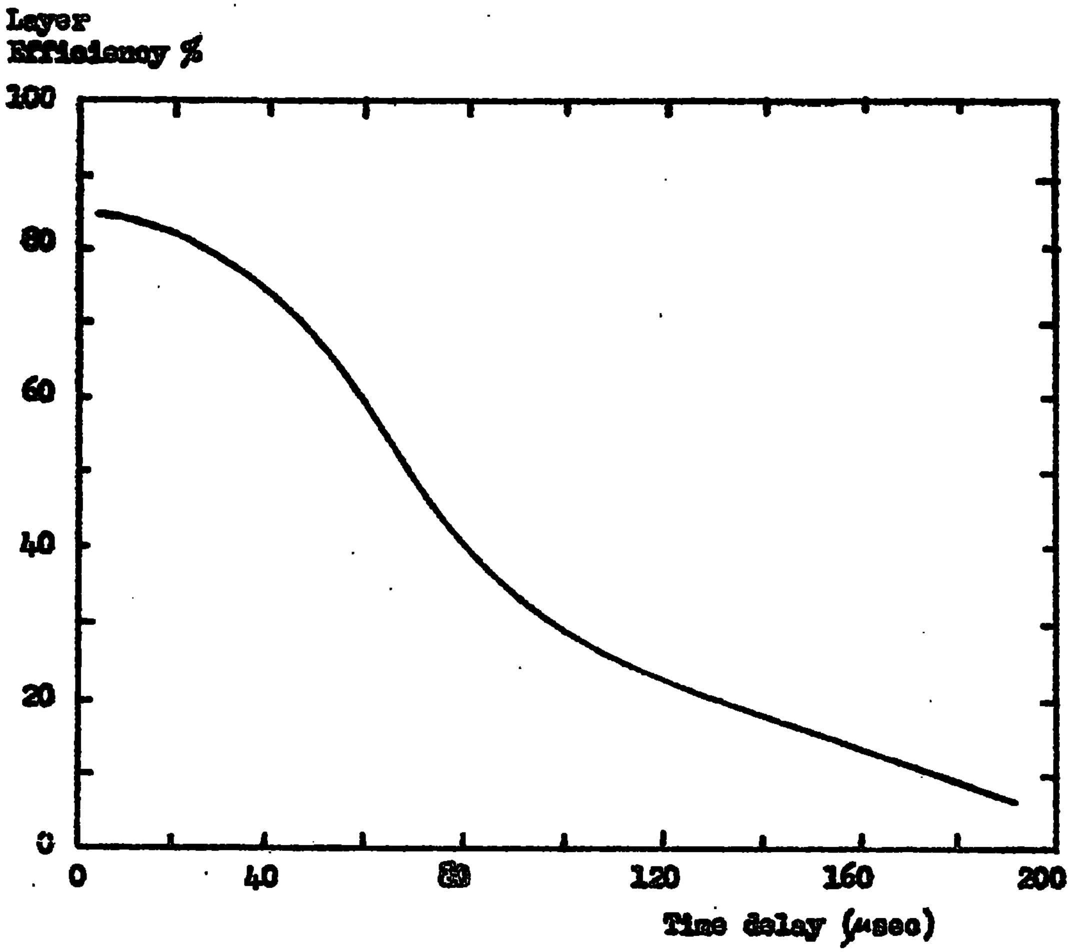

Fig.2.9 (a) The efficiency, time delay characteristic for the tubes used in the horizontal spectrograph.

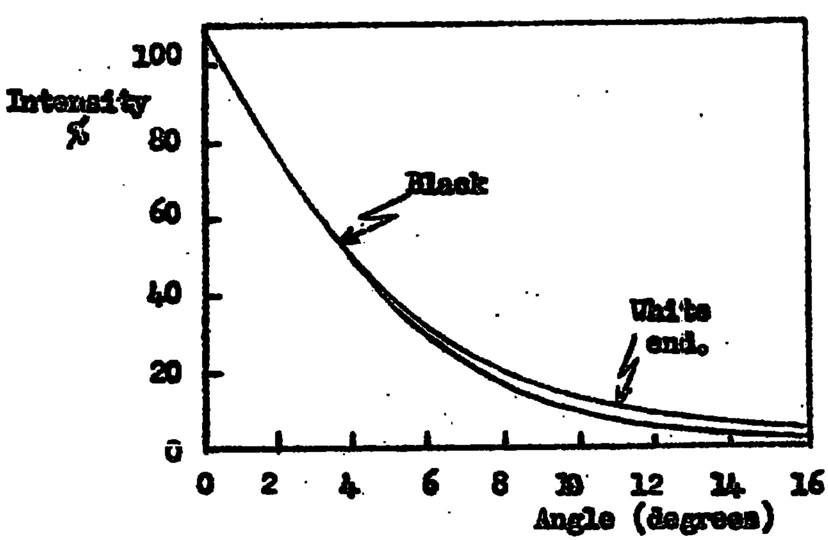

Fig. 2.9 (b) Polar diagram for light output from the flash-tubes.

Table 2.1

Spurious Flashing

The ratios are per tube per 1000 pulses

Pressure \ Field	2.1	2.8	3.5	4.2	4.9	5.6 Kv/cm
60 cm Hg	0.18	0.54	0.37	0.6	0.6	0.6
35 cm Hg	0.0	0.18	0.0	0.18	0.2	0.8
20 cm Hg	0.18	0.18	0.18	0.2	1.2	4.0

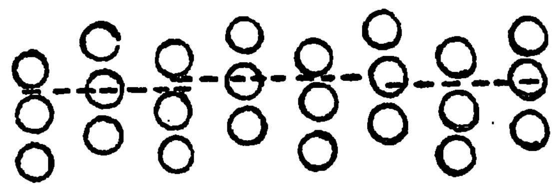

a) A section of a flash-tube array.

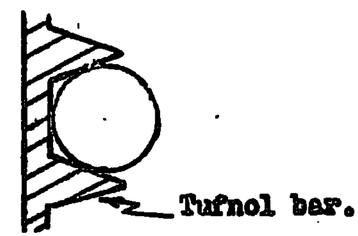

b) Flash-tube support.

Fig. 2.10 The arrangement of the flash tube arrays.

Plate 1 A tray of neon flash tubes, showing the track of a cosmic ray muon.

(ii) Short rise time of the applied pulse.

(iii) Short delay between the passage of a particle and the application of the pulse.

(iv) A direction of photography making the smallest possible angle with the axes of the flash tubes.

There are four trays (each having eight layers of tubes) of flash tubes contained in the spectrograph, the tubes in each tray being staggered in such a way that a single particle passing through a tray must traverse at least four tubes (fig. 2.10(a), plate 21). Thin aluminium electrodes are placed between each layer of tubes. The tubes are supported in slots milled in 'Tufnol' square section rod (fig. 2.10(b)) and placed in such a manner that any small bowing of the tube is in the horizontal plane since accurate measurements are required in the vertical direction in each tray. The tubes within a tray are accurately parallel to one another, and the trays are aligned so that all the tubes in the spectrograph are parallel. The vertical separation of the centres of adjacent tubes is (1.905 $\pm$ 0.001 cm.) which will be referred to as one tube separation or "t.s." The horizontal separation of tubes in adjacent layers of tubes in a tray is 2.8 cm.

2.4 Detection of particles

The passage of an ionizing particle through the spectrograph was detected by means of five trays of 20th Century Electronics G60 Geiger counters each of sensitive length 60 cm. and internal diameter 3.28 cm.

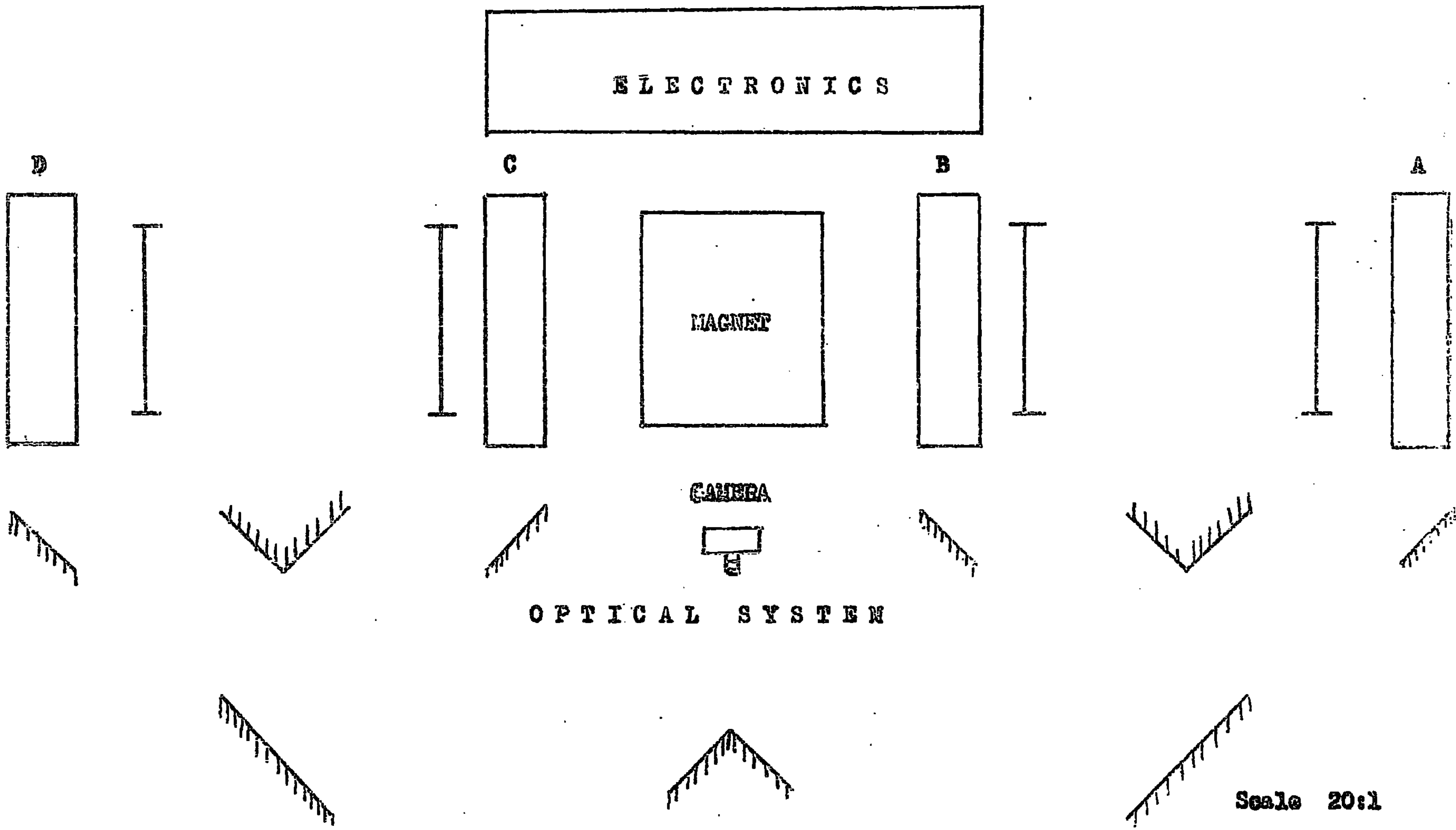

Fig. 2.11 Plan view of the horizontal spectrograph.

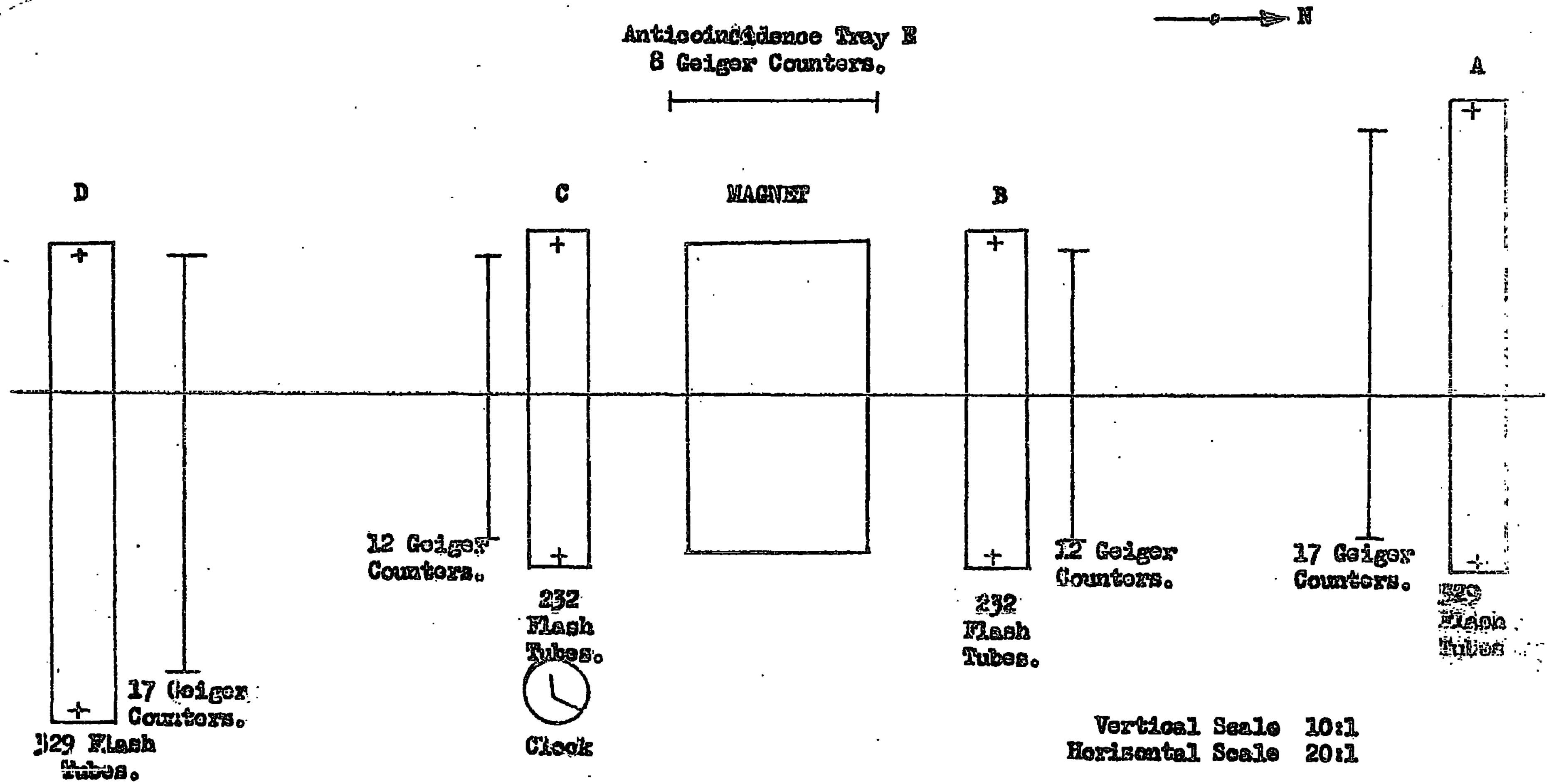

Fig. 2.12 Side elevation of the horizontal spectrograph.
(+ are fiducial bulbs.)

Four of these trays were close to, and parallel to, the four trays of flash tubes whilst the fifth tray was situated above the apparatus to act as an anticoincidence tray for the rejection of extensive air showers.

2.5 The general arrangemant of the horizontal spectrograph

The general arrangement of the spectrograph is shown in figures 2.11, 2.12, and an aerial photograph of the apparatus is shown as the frontpiece. The axis of the spectrograph is orientated at an angle of N9^{o}E, this being the most suitable position in order that firstly the particle flux should not be affected by the thick sandstone walls of Durham Cathedral nor by the copper covered Applebey lecture theatre, and secondly the axis may be as close as possible to geomagnetic north.

The requirement for an event to be accepted is a four-fold coincidence pulse ABCD without a coincidence pulse from the counters in the tray E of Geiger counters above the apparatus. When this requirement is satisfied, a high voltage pulse is applied to the flash tube electrodes and a photograph of the flashed tubes is taken through the mirror system. The mirrors are so arranged that the camera views all four trays of flash tubes. At the same time a cycling system is triggered which firstly illuminates a clock under tray C and two fiducial marks on each flash tube tray, and secondly moves on the film.

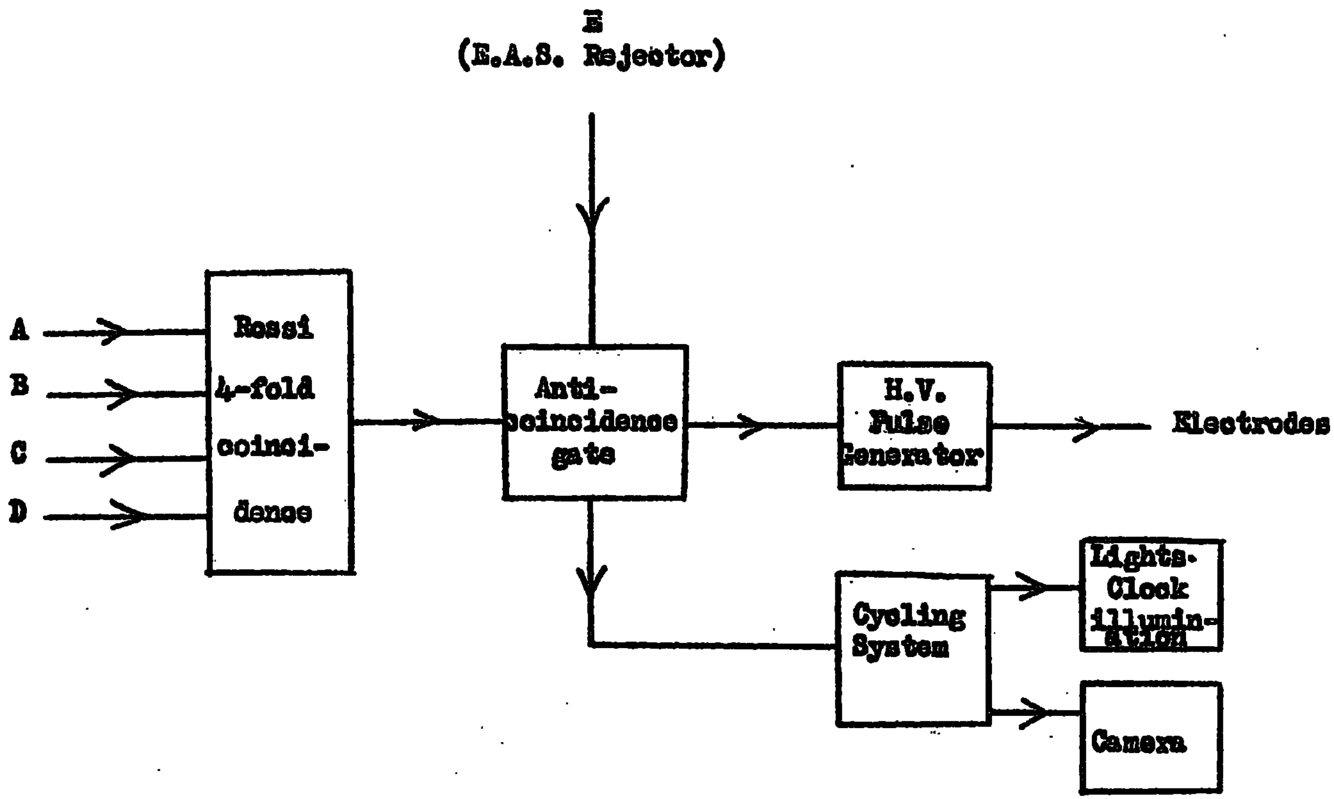

Fig. 2.13 Block diagram of the electronic circuits.

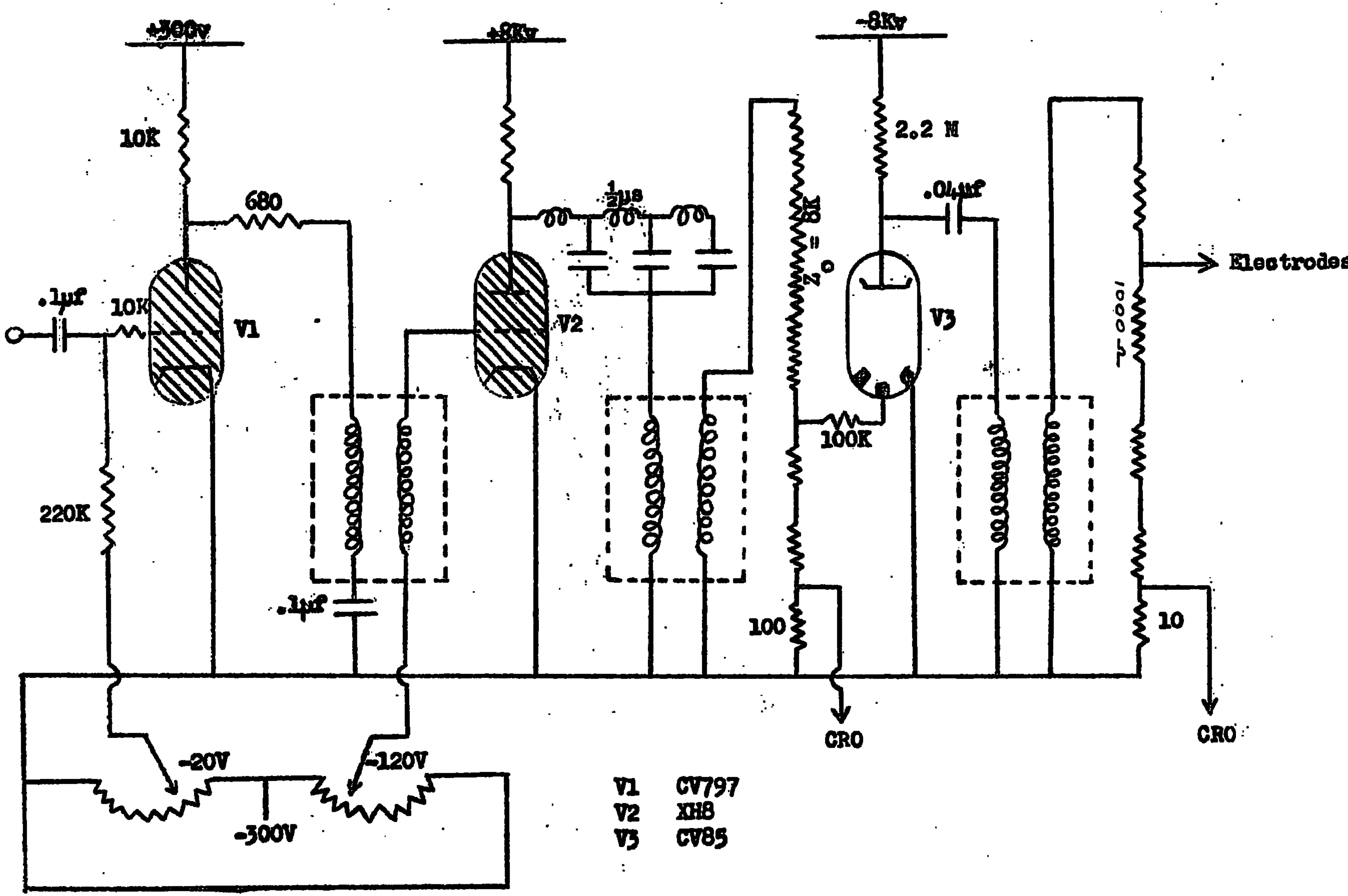

Fig. 2.14 The high voltage pulsing unit.

Plate 2 The Electronics.

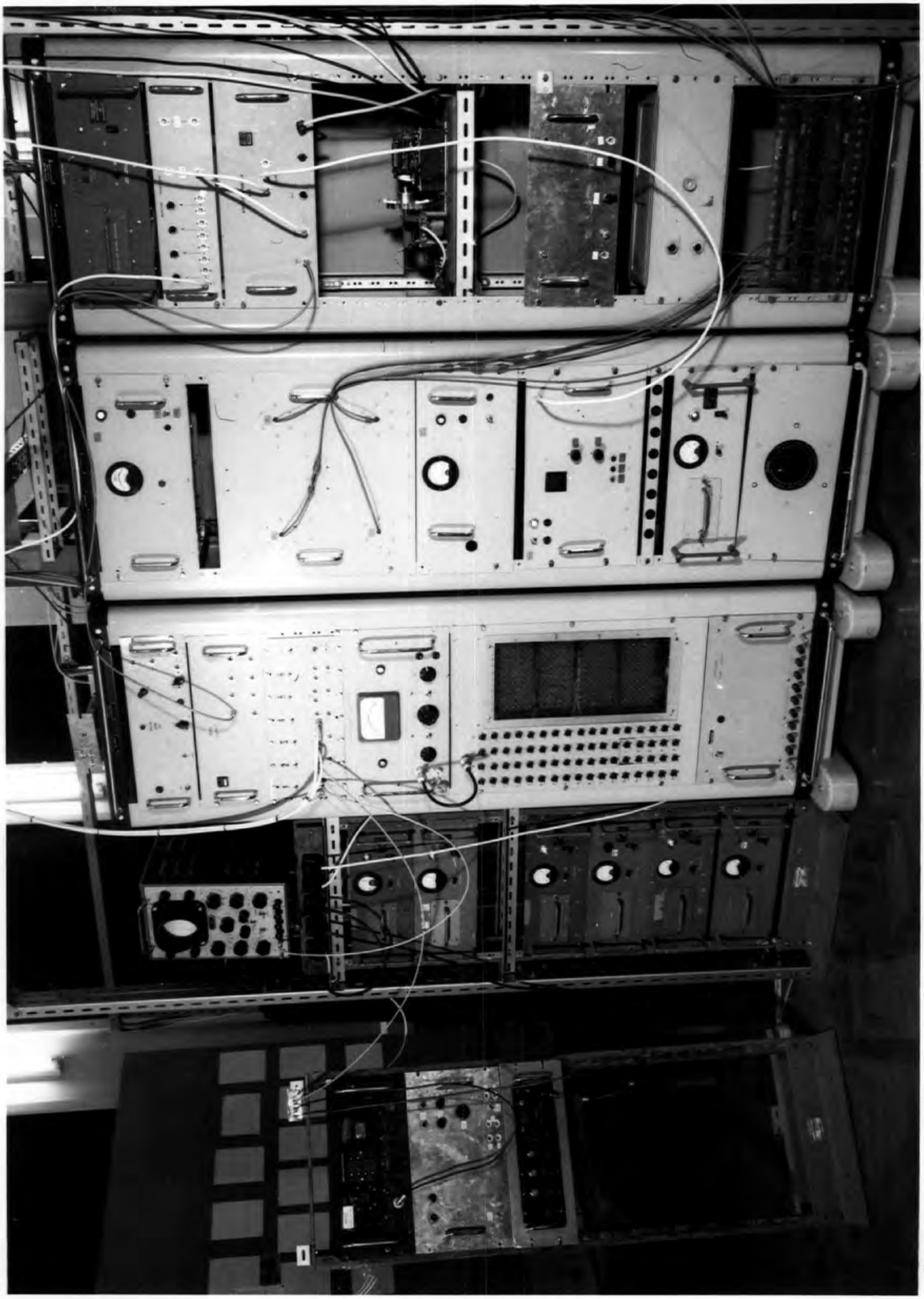

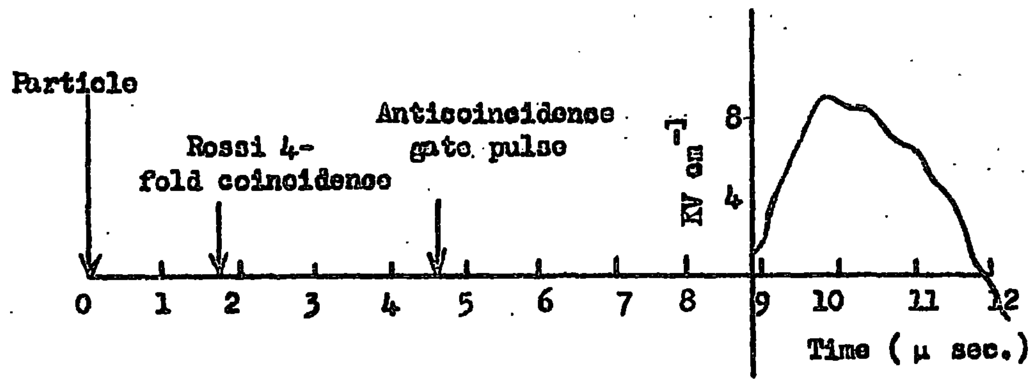

Fig. 2.15 Time sequence from the passage of an ionising particle to the application of the high voltage pulse.

2.6 The Electronic Circuits

A block diagram of the electronic system is shown in fig. 2.13. As has been mentioned already, the requirement for an event to be accepted by the instrument is a four-field coincidence pulse ABCD without a pulse from the anticoincidence tray of Geiger counters. A thyratron is then triggered by the output pulse from the anticoincidence gate. This in turn triggers the high voltage unit which comprises an 8 KV hydrogen thyratron and pulse transformer. Four further units are triggered by this latter unit: each of these units consist of an enclosed spark gap ('trigatron' - CV85) and a pulse transformer. The output of each of these units is fed to a flash tube tray. The high voltage pulsing unit is shown in fig. 2.14. The arrangement of the electronics is shown in plate II.

The time sequence of the events following the traversal of an ionizing particle through the spectrograph is shown in fig. 2.15. From this it is seen that a pulse of rise time 0.8μsec. is applied to the electrodes 8.8μsec. after the passage of the particle through the apparatus. The measured rate of spurious flashes, i.e. flashes not associated with an accepted particle, is $\sim 6 \times 10^{-4}$ per tube per pulse.

From a typical sample of 259 events, the layer efficiency was found to be 78%. This figure and that for the rate of spurious flashes are in good agreement with the values reported by Coxell (1961) for the same conditions of applied pulse.

2.7 Alignment of the spectrograph

The alignment of the instrument and the determination of the geometrical constants are subjects of great importance and a detailed discussion follows.

Each flash tube tray is fitted with four plates through each of which a single hole is bored, the plates being in identical positions on each tray. The trays B and C are supported on arms fixed to the pillars of the magnet framework and the trays A and D are supported on frames bolted to the laboratory floor. Adjusting screws in the top cross-member in each tray are located kinematically on the frameworks allowing for rotation in the two directions parallel to and at right angles to the spectrograph axis. After the correct positions are found the trays can be bolted rigidly to the frameworks.

In the alignment process the four trays were adjusted so that

(a) cotton fibres were able to pass through the centre of the hole in each plate at both sides, and

(b) each tray was in the vertical plane and the tubes in it were horizontal, the degree of horizontal levelling being checked in three ways viz:

(i) optically with a cathetometer and telescope.

(ii) directly using a sensitive spirit level.

(iii) by using a straight glass tube, of the same diameter as the flash tubes, containing a small amount of mercury (effectively a large spirit level).

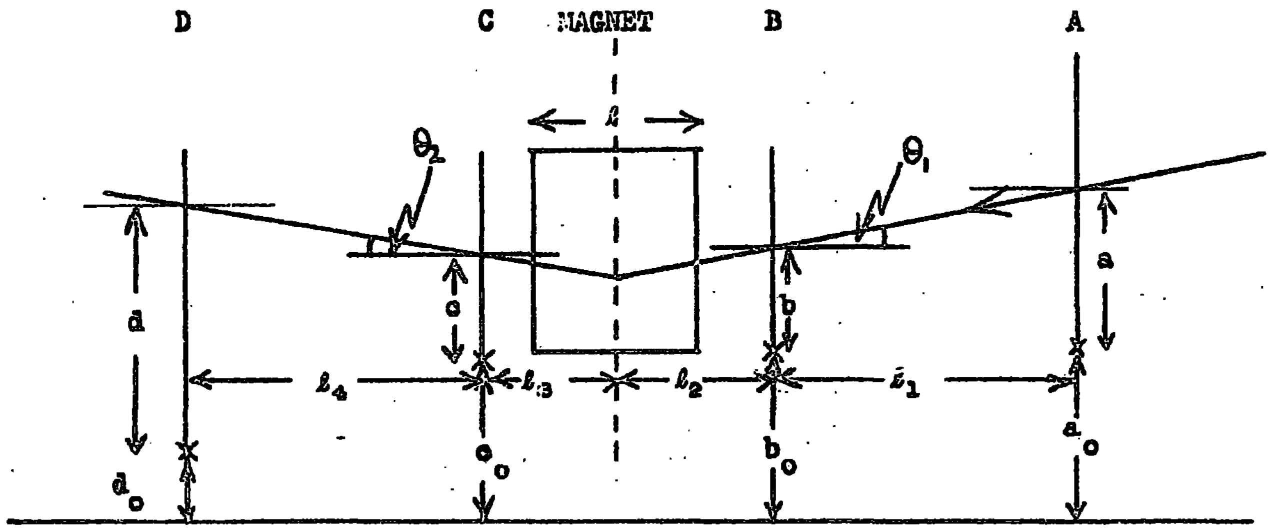

Fig. 2.16 The experimental arrangement.

Table 2.2

Adopted Values of Geometrical Constants (c.f. fig. 2.16)

Dimension	cm	t.s.	
ℓ_1	149.15 ± 0.02	78.29 ± 0.01	
ℓ_2	74.54 ± 0.04	39.13 ± 0.02	
ℓ_3	71.95 ± 0.03	37.77 ± 0.02	
ℓ_4	150.44 ± 0.05	78.97 ± 0.03	
ℓ	63.5	33.33	
a_o	25.643 ± 0.003	13.461 ± 0.002	Normalised to $d_o = 0$
b_o	25.864 ± 0.002	13.577 ± 0.001	
c_o	25.512 ± 0.002	13.392 ± 0.001	
d_o	0 ± 0.002	0 ± 0.001	

1 t.s. = 1.905 cm.

The constants of the spectrograph (fig. 2.16) were determined using cotton fibres stretched along the length of the spectrograph from knife edges at each end, one pair on the east and one pair on the west. A cathetometer was then used to set the knife edges in the horizontal plane and to measure the distance from the fibre to a reference tube in each tray. In each tray the reference tube is the bottom tube in the fourth layer. The vertical and horizontal separation of adjacent tubes within a tray were also measured at the same time. The vertical separation of the centres of adjacent tubes in a particular level is called the tube separation (t.s.). Use is made of this quantity in the method of measurement of the accepted events. The horizontal dimension of the spectrograph were measured with an accurate steel tape.

Corrections to the vertical measurements were made for the catenary effect and all the measurements were repeated by two other independent observers. The final adopted values are shown in Table 2.2.

The quantities a_o, b_o, c_o, d_o and the various l's are found from the alignment measurements and the measurements on the photographs (to be discussed later) give the coordinates a, b, c, d. With a knowledge of these constants and the coordinates a, b, c, d the momentum of a particle traversing the apparatus can be calculated.

If a charged particle of momentum p(eV/c) passes through a magnetic field of H gauss, the radius of curvature ρ (cm) of the track of the particle is given by

$$p = 300 H \rho z$$

where z is the charge. In the case of the μ-meson, $z = 1$

$$\therefore \quad p = \frac{300 \int H \, dl}{\theta}$$

where θ is the angular deflection of the particle track in passing through an element of magnetic field of thickness dl.

$$\text{i.e.} \quad p\,\theta = 300 \int H \, dl$$

From table 2.2 the thickness of the magnetized iron 1 is 63.5 cm. giving $p\theta = 17.47$ GeV/c degree for H = 16 K gauss.

In fig. 2.16,

$$\theta_1 = \left\{ (a + a_0) - (b + b_0) \right\} \ell_1^{-1}$$

$$\theta_2 = \left\{ (d + d_0) - (c + c_0) \right\} \ell_4^{-1}$$

in the small angle approximation. The angular deflection, θ, of the particle in the magnetic field is given by

$$\theta = \theta_1 + \theta_2$$

$$\therefore \ell_1 \theta = \left\{ (a - b) - \frac{\ell_1}{\ell_4} (c - d) \right\} + \left\{ (a_0 - b_0) - \frac{\ell_1}{\ell_4} (c_0 - d_0) \right\}$$

$$\text{ie} \quad \ell_1 \theta = \Delta + \Delta_0$$

Thus Δ_0 is a constant of the instrument and has a value -13.39 t.s. in the present arrangement, and Δ is determined directly from the measured quantities a, b, c, d for each accepted particle. Details of the method of measuring these quantities is given in chapter 3.

Thus for the above case where H = 16 K gauss,

$$p (\Delta + \Delta_0) \ell_1^{-1} = 17.47 \text{ GeV/c}$$

$$\text{and} \quad p (\Delta + \Delta_0) = 23.87 \text{ GeV/c (t.s.)}$$

Chapter III

THE EXPERIMENTAL DATA

3.1 Introduction

The data under analysis were collected over a running time of 169 hours 4 minutes. During this period the mean magnet current was 15.50 ampères giving a mean value for the magnetic induction of 15.85 K gauss. To obviate any bias introduced by the experimental arrangement the magnetic field was reversed for half the running time. Once again, using the relation

$$p\theta = 300\int H\,dl,$$

$$p\theta = 17.3 \text{ GeV/c. deg.}$$

$$\text{and } p(\Delta+\Delta_0) = 23.6 \text{ GeV/c. (t.s.)} \quad \text{for } H = 15.85 \text{ Kgauss.}$$

3.2 The measured rate of events

During the running time the measured rate of events was as follows:

Coincidences ABCD : 38.8 ± 1.0 hour^{-1}

Coincidences ABCD$\bar{E}$: 16.4 ± 0.4 hour^{-1}

Rate of single particle events observed on film: 7.9 ± 0.4 hour^{-1}. These figures demonstrate the large contribution to the counting rate from extensive air showers (ABCD - single particle rate, ~ 30 hr^{-1}). The overwhelming majority of the showers comprise electrons and have an intensity distribution which varies with zenith angle, θ, as $\cos^8\theta$ (e.g. Coxell et al., 1962). They are thus collimated near the vertical direction and in consequence do not cause confusion in the analysis of greatly inclined particles. It is considered that the number of muons lost through their being accompanied by showers is very small. As it is,

Plate 3 The track of a 36.3 GeV/c negative muon incident at 89.8° to the zenith.

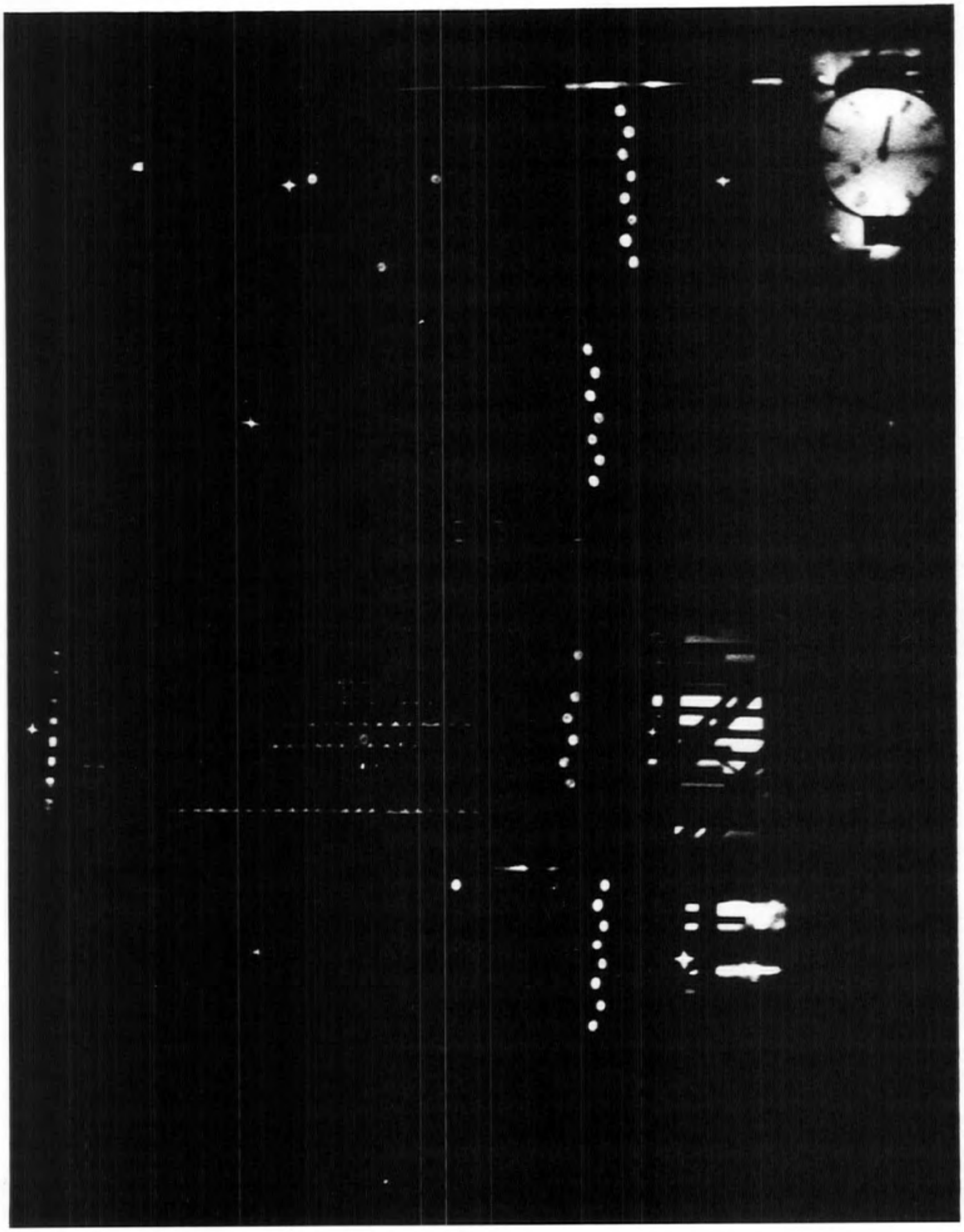

Plate 4 The track of a 23 GeV/c positive muon incident at 87.4^{o} to the zenith, with the track of a knock-on electron in tray C.

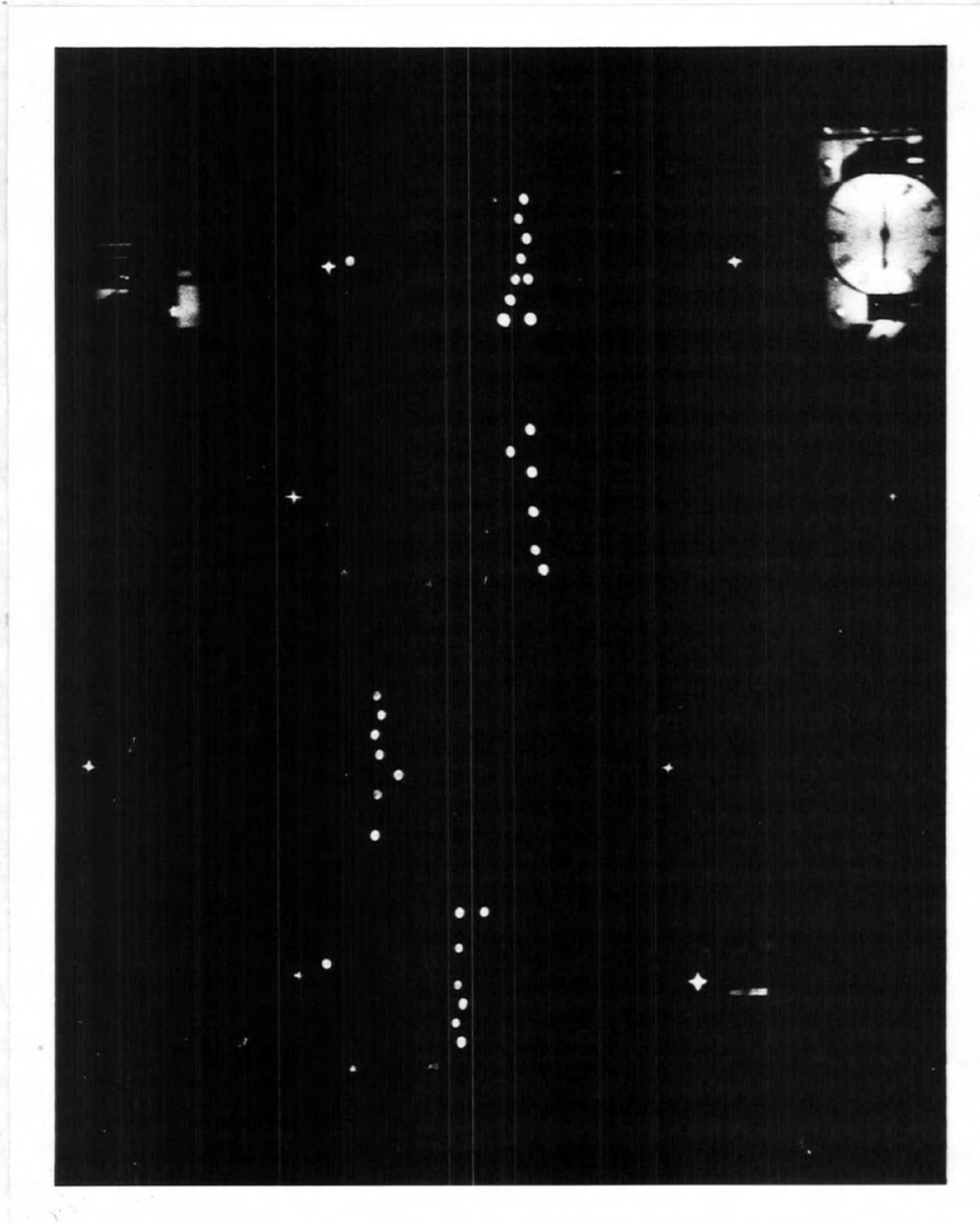

Plate 5 The track of a 337 GeV/c positive muon incident at 83.4° to the zenith. Also shown are the tracks of knock-on electrons in trays C and D.

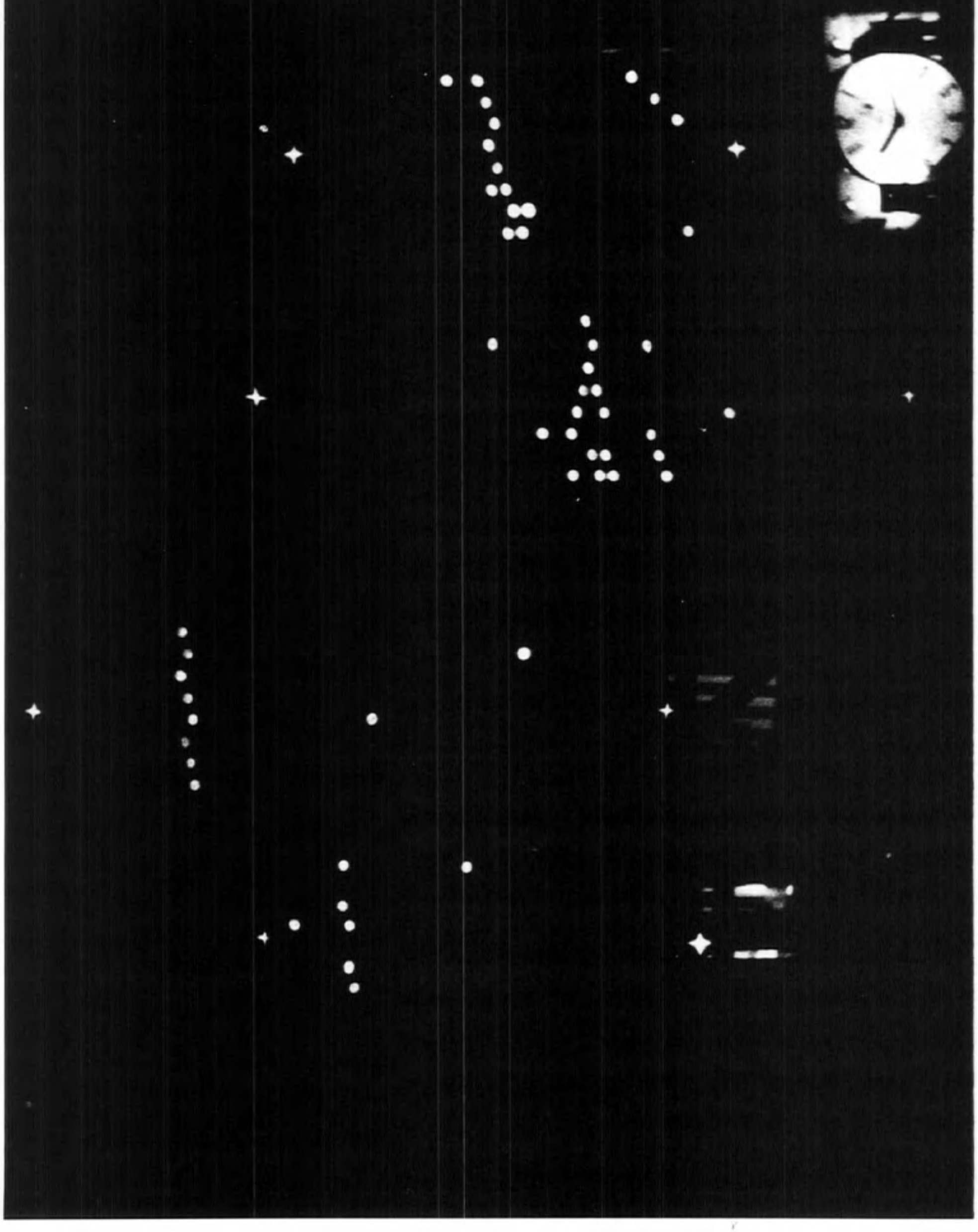

Plate 6 The track of a 1180 GeV/c (approx) positive muon incident at 87.5° to the zenith, with a knock-on electron in tray A.

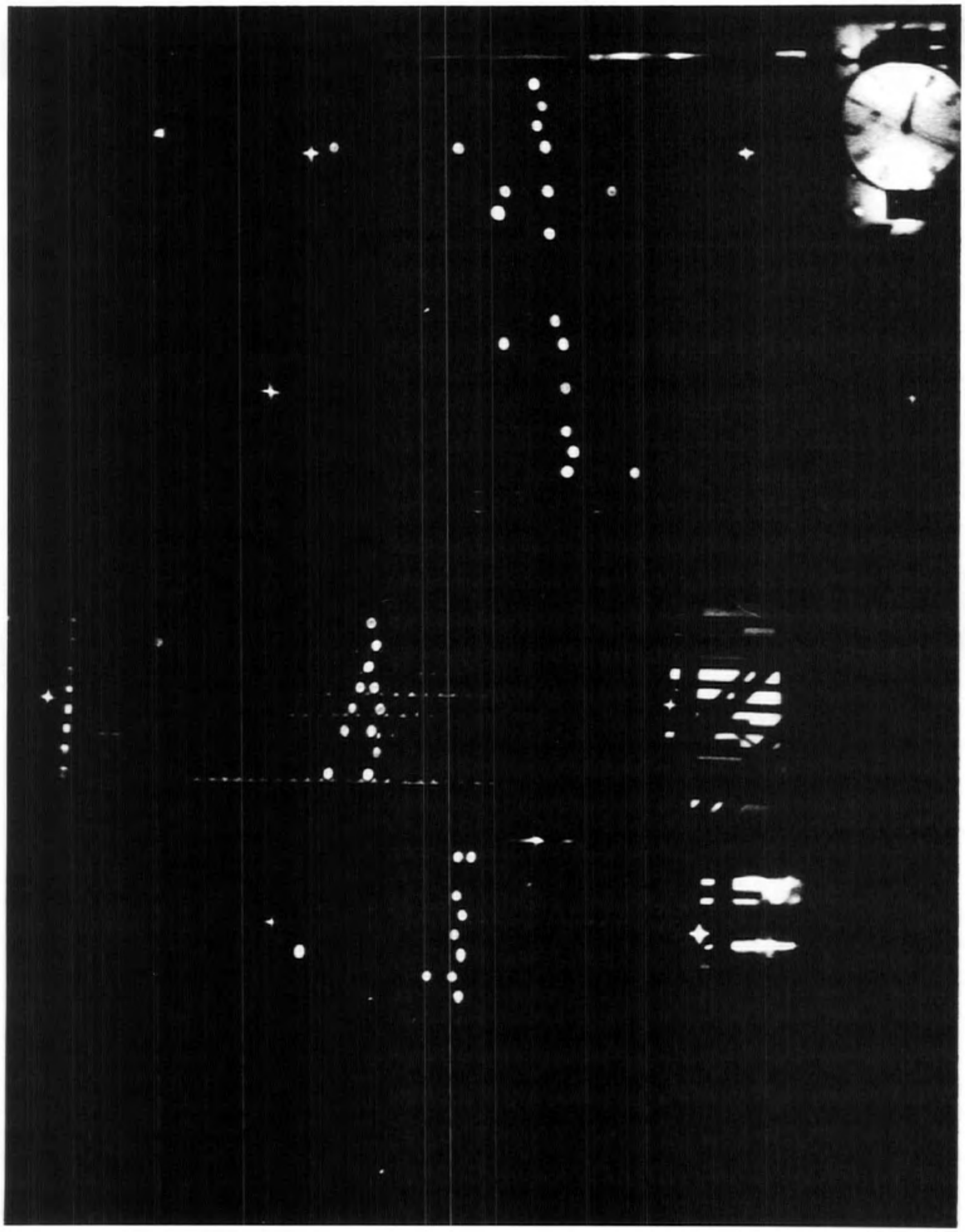

Plate 7 The track of a 112 GeV/c negative muon incident at 89^{o} to the zenith.

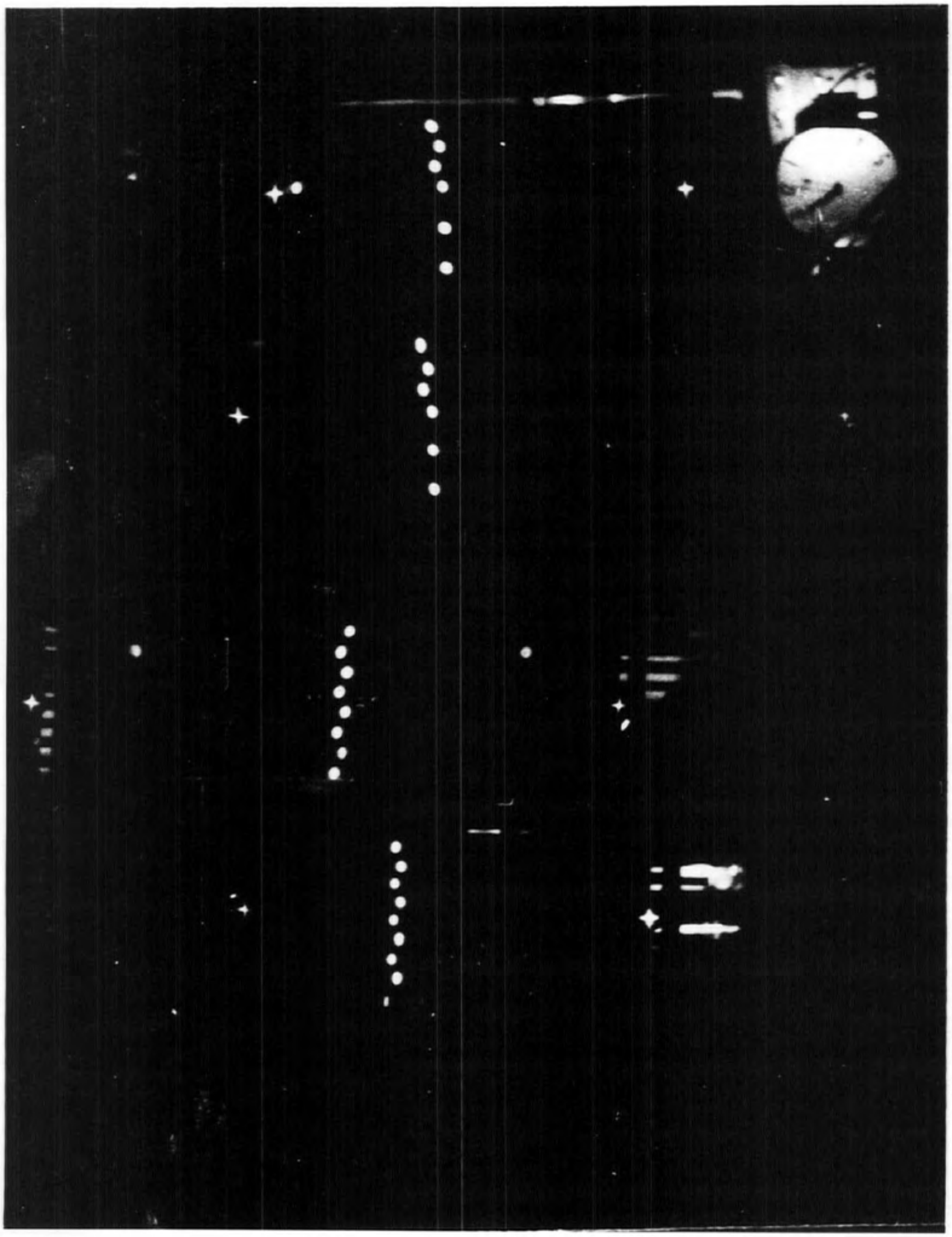

Plate 8 A dense extensive air shower detected
by the instrument.

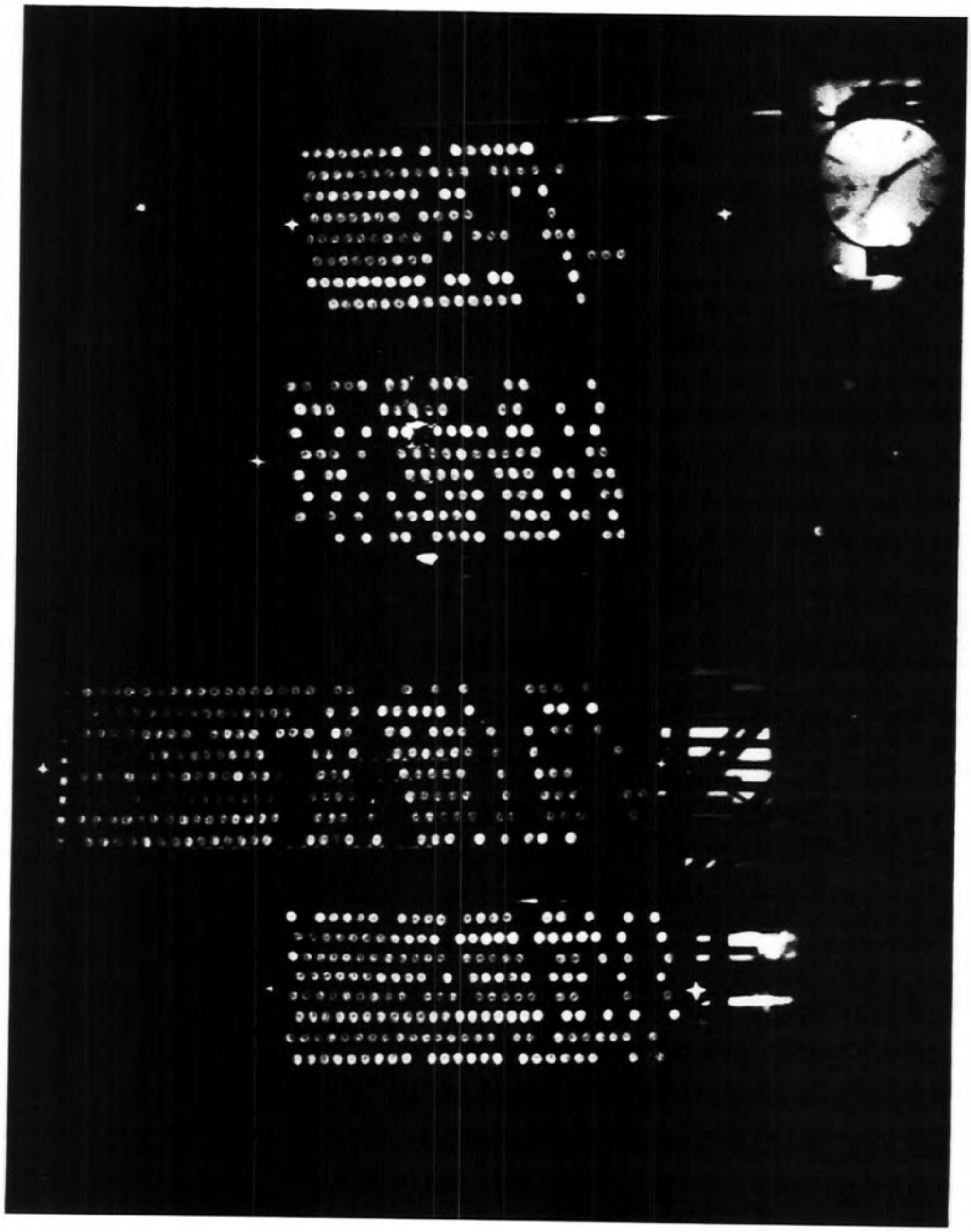

it is easily seen from the above figures that even with the anti-coincidence arrangement about one half of the events recorded photographically consist of extensive air showers. These showers have a low density and do not trigger the anti-coincidence tray of Geiger counters by virtue of statistical fluctuation of density.

3.3 The measurement technique

In order to derive a momentum spectrum it is necessary to know the angular deflection for each particle passing through the magnetic field. The momentum can then be calculated using the relationship between p and θ. However, since the deflections considered are small it is more convenient to work with the linear dimension $\ell_1\theta = \Delta + \Delta_0$ and use the relation $p(\Delta+\Delta_0) = 23.6$ GeV/c t.s. As mentioned earlier, Δ_0 is a constant of the spectrograph and Δ is determined directly from the measured quantities for each accepted particle.

Each photograph was projected on to a screen on which was marked the outline of each flash tube in each tray together with the pairs of fiducial marks. A cursor was then adjusted over the images corresponding to the passage of the particle through a single tray of flash tubes and the best estimate made of the position of the track. A scale, in units of tube separation (t.s.), was marked on the screen at the centre of the fourth row of flash tubes in each tray. The coordinate where the reference level and cursor cross was noted for each tray, giving the values of a, b, c, d. The error in these measurements has a root mean square value of 1.49 mm at each level.

A selection of recorded events is shown in Plates 3-8. Reading from

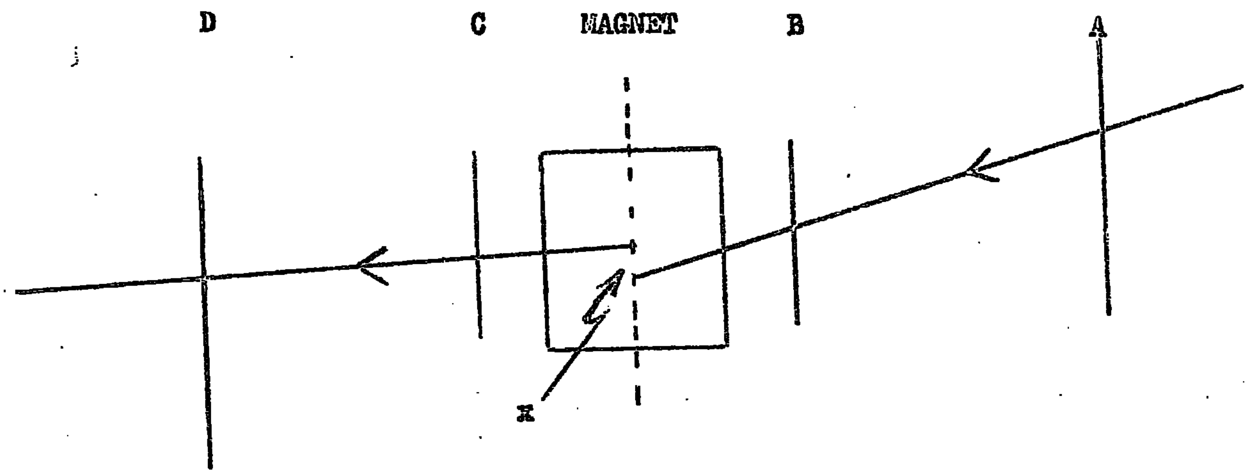

Fig. 3.1 The discrepancy, x, at the centre of the magnet.

Deflection Interval (t.s.)	Momentum Interval at Centre of Magnet (GeV/c)	Mean Incident Momentum (GeV/c)	Observed Number of Particles as a function of Zenith Angle					
			77.5°-80°	80°-82.5°	82.5°-85°	85°-87.5°	87.5°-90°	Total
15.1-6.45	1.56-3.66	3.2	27	24	20	3	6	80
6.45-4.1	3.66-5.76	5.3	27	26	24	10	1	83
4.1-2.4	5.76-9.83	8.4	29	44	25	13	7	118
2.4-1.16	9.83-20.3	15.1	65	84	59	32	11	251
1.16-0.76	20.3-31.1	25.7	51	62	57	20	15	205
0.76-0.46	31.1-51.3	41.2	32	58	51	37	15	193
0.46-0.32	51.3-73.8	62.6	14	24	30	20	13	101
0.32-0.23	73.8-103	88.4	9	22	13	18	13	75
0.23-0.11	103-215	143	17	13	29	20	20	99
0.11	>215	*	9	17	15	19	9	69
		Total	275	374	323	192	110	

*This varies with zenith angle, the values being:

Zenith Angle	77.5°-80°	80°-82.5°	82.5°-85°	85°-87.5°	87.5°-90°
Mean Incident Momentum (GeV/c)	446	464	468	518	561

Grand Total of accepted muons 1274

Table 3.1: The basic data for the projection measurements

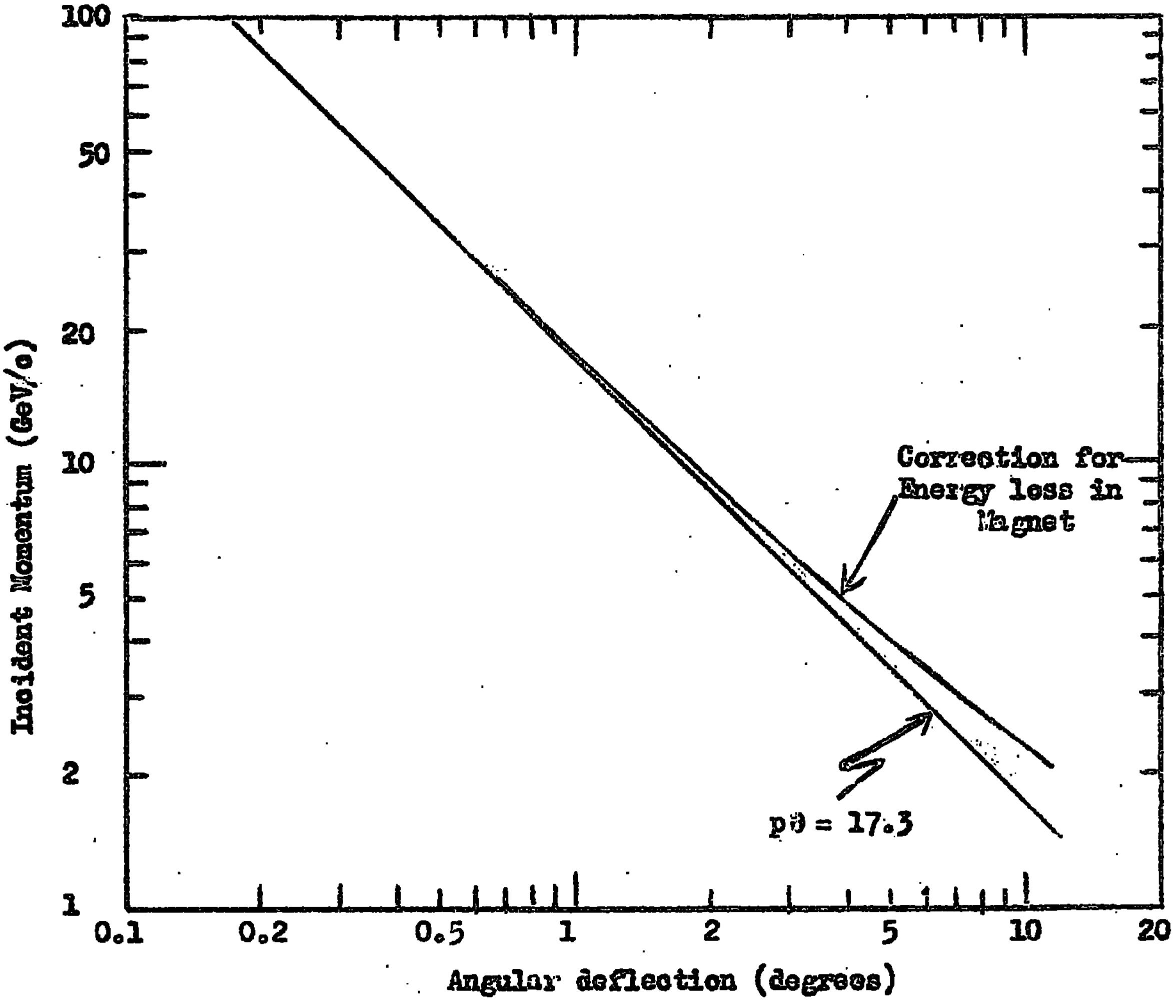

Fig. 3.2 The relationship between the incident momentum and angular deflection for the present experimental arrangement.

right to left, the flash tube traysare respectively C, D, A and B (a peculiarity of the optical system used) and particles moving in a North-South direction traverse each tray from right to left.

3.4 The basic data

During the period in which the spectrograph was in operation, some 1305 single particles were recorded.

From the measured data, comprising a, b, c, and d for each particle, the angles of incidence and emergence, the displacement $\Delta + \Delta_0$ and the discrepancy, x (fig. 3.1), at the centre of the magnet were calculated. Events where the zenith angle of incidence was less than 77.5°, or with $|\Delta+\Delta_0| > 15.1$ t.s. were rejected.

Table 3.1 gives the number of accepted events for the various momentum and zenith angular ranges. The momenta shown in this table are corrected for momentum loss in the iron of the magnet according to the relation

$$\Delta\theta = -\frac{300\,B}{\alpha}\ln\left(1-\frac{\alpha\ell}{p}\right)$$

where $\Delta\theta$ is the angular deflection

B is the magnetic induction

α is the mean momentum loss per unity path length in the iron

ℓ is the thickness of the magnet

and p is the incident momentum of the muon.

Figure 3.2 shows the relationship between the incident momentum and angular deflection for the present experimental arrangement. Also shown is the straight line

$$p\theta = 17.3 \text{ GeV/c . deg.}$$

which assumes that there is no momentum loss in the magnet. As can be seen, the correction is significant for slow muons, being 30% for a 2 GeV/c muon.

Although the accuracy of track measurements resulting from the simple observations on the projected images is sufficient for particles of comparatively low momentum ($p \lesssim$ 100 GeV/c), an improved technique is necessary for particles of higher momenta to give the necessary higher degree of accuracy. Consequently the fast particles were re-examined using the following method. The positions of the flashed tubes in each tray were noted and this information was transferred to a scale diagram (track simulator) (fig. 3.3) of a portion of a stack of flash tubes. To improve the accuracy of location the scale diagram was enlarged by a factor 2.5 in the vertical direction and by a factor 0.716 in the horizontal direction. A cursor was placed on this scale diagram at an angle corresponding to the angle of incidence or emergence of the particle, depending on which tray of tubes was being examined, this angle being obtained from a knowledge of the first projection measurements. Consider a particular tray (A say) where it is observed that the following tubes had flashed (Row 1 is the North face of each stack):

Row No.	8	7	6	5	4	3	2	1
Tubes flashed	10	10	-	10	11	-	11	11

and (a-b) = + 8.5 t.s.

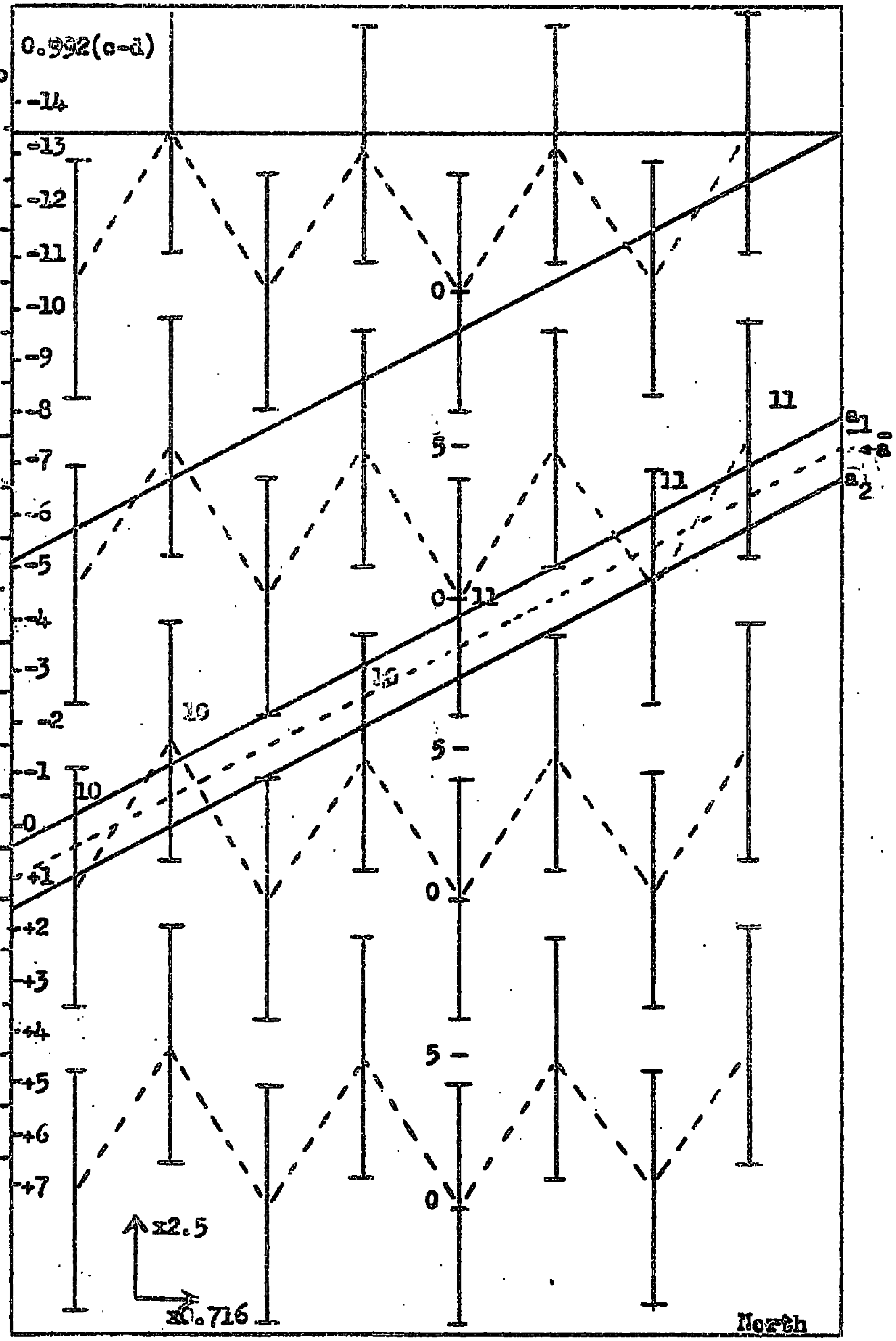

Fig. 3.3 The track simulator (Only part of the scale is shown in the reference layer. Upper limit $a_1 = 10.94$, Lower limit $a_2 = 10.74$ Mean value $\hat{a} = 10.84$ t.s. Estimated best line shown dotted).

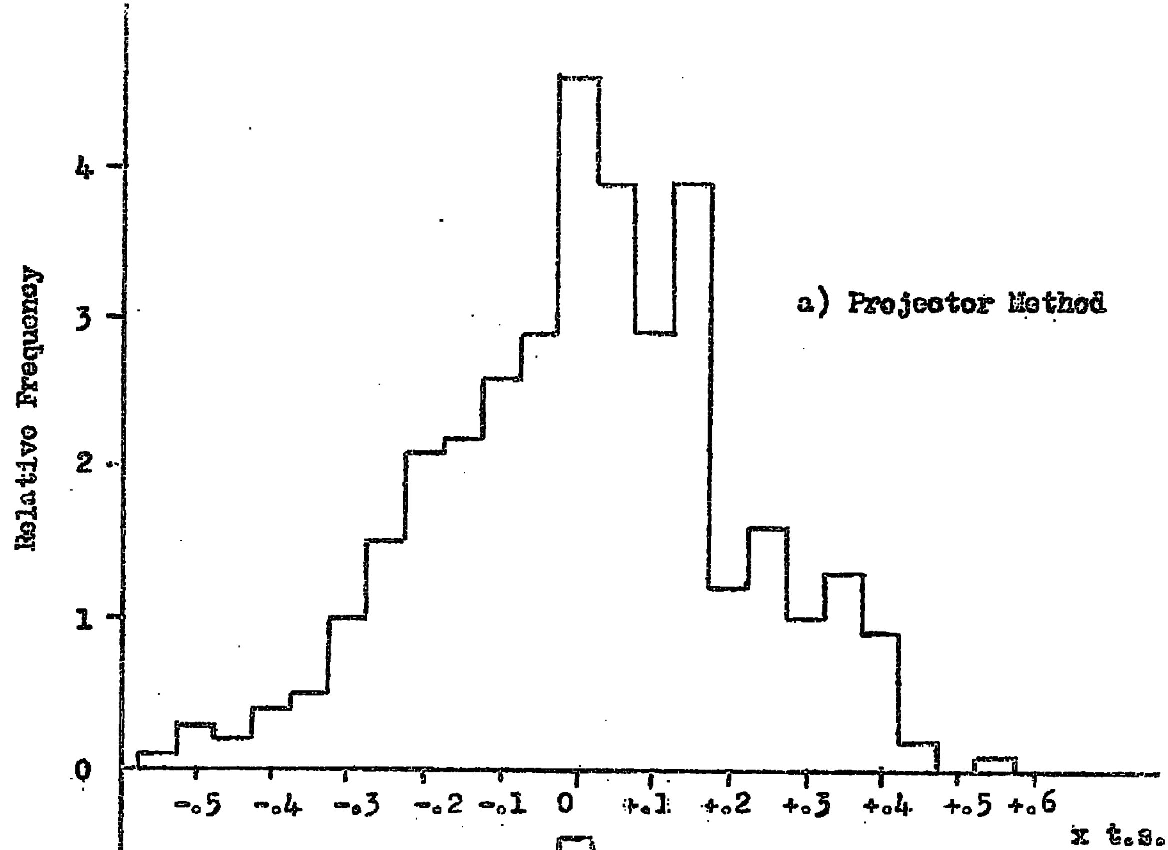

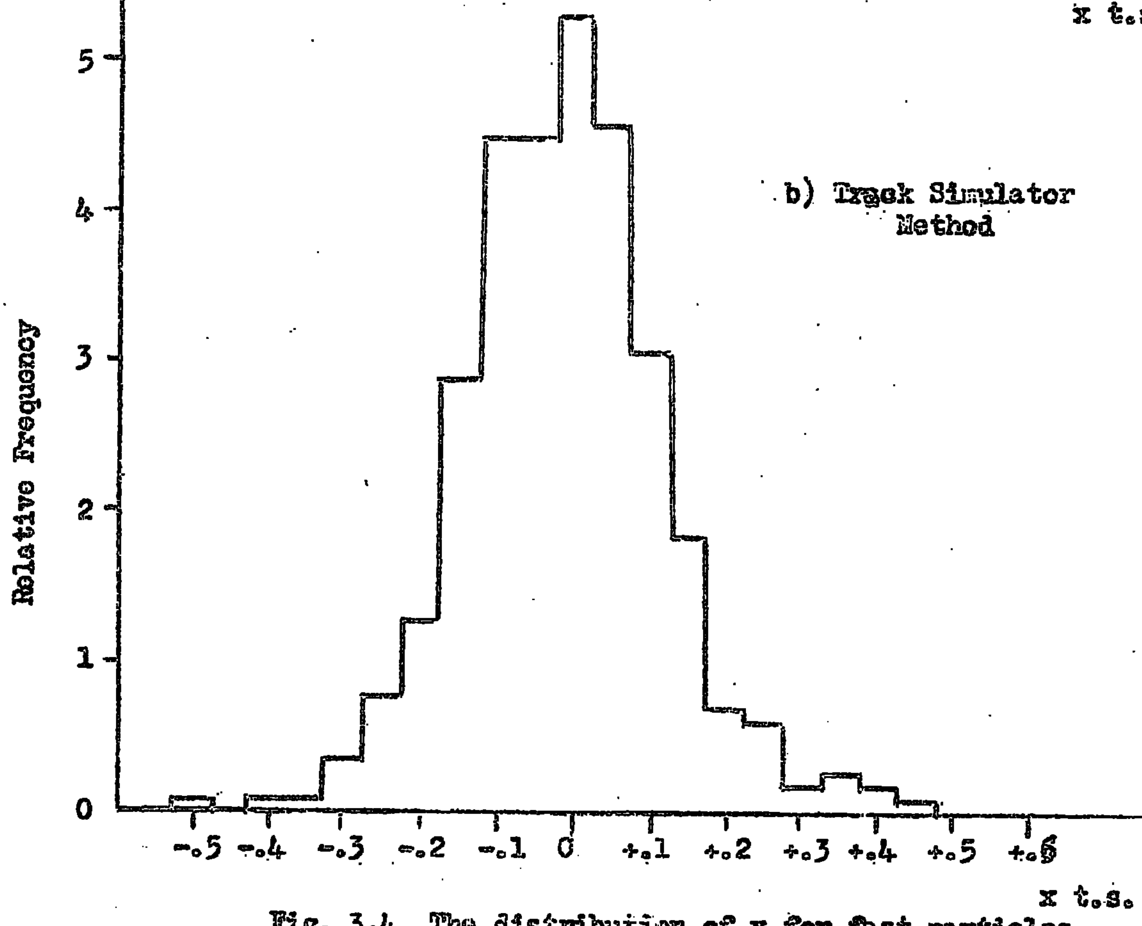

Fig. 3.4 The distribution of x for fast particles.

The procedure to obtain the best value for <u>a</u> is as follows:

1) Mark on the diagram the flashed tubes.

2) Place the diagram on the cursor baseboard and line up the cursor along the horizontal line near the top of the scale diagram.

3) Swing the cursor about its axis until it crosses the scale for (a-b) where (a-b) = + 8.5 t.s. and clamp it in this position.

4) Slide the cursor down the scale and obtain the two extreme limits of the track which satisfy the above information.

5) Note the coordinates in flash tube row 4 of these limits and obtain the mean value of <u>a</u>.

6) Repeat for trays B, C, D, using the emergent angular displacement (c-d) for trays C and D.

7) Recalculate the deflection $\Delta + \Delta_o$ and the discrepancy x at the centre of the magnet.

In order to provide a wide overlap with the data scanned normally, all particles with $|\Delta+\Delta_o| \leq 0.46$ t.s. (i.e. $p \gtrsim 50$ GeV/c) were re-measured.

A very sensitive indicator of the accuracy with which the measurements are made is the magnitude of the discrepancy, x, at the centre of the magnetic field. The frequency distributions for x for the two methods of analysis are shown in figure 3.4. That there is an improvement in the accuracy for the track simulator data shows up as a reduction in the width of the distribution. For the normal scanning technique, x has a mean value +(0.014 $\pm$ 0.010) t.s., whilst for the track simulator technique the mean value of x is $-(0.008 \pm 0.006)$ t.s.

There are two sources of x:

i) errors in track location in each tray of flash tubes

and ii) the effect of Coulomb scattering in the magnet.

Ashton et al (1961) showed that the magnetic displacement, Δ, at a detecting level a distance L ($> \ell$, the thickness of the magnet) below the top (i.e. incident face) of the magnet is

$$\Delta \simeq \delta + (L-\ell)(\theta_2-\theta_1)$$

where the magnetic displacement, δ, at the bottom (i.e. emergent face) of the magnet is given by

$$\delta = -\frac{300\,B}{\alpha}\int_0^{\ell} \ln\left(1-\frac{\alpha x}{p_1}\right)dx$$

and The magnetic angular deflection $(\theta_2-\theta_1)$ is

$$-\frac{300\,B}{\alpha}\ln\left(1-\frac{\alpha\ell}{p_1}\right)$$

where B is the magnetic induction,

α is the mean momentum loss per unit path length of the muon in the iron,

p_1 is the incident momentum.

They also showed that the mean square projected displacement $\langle y^2\rangle$ at the same detecting level is given by

$$\langle y^2\rangle = \langle y_0^2\rangle + \frac{K^2}{2X_0 p_1^2}\sum_{n=2}^{\infty}\left(\frac{\alpha\ell}{p_1}\right)^{n-1}\ell\left\{(L-\ell)^2+\frac{2(L-\ell)\ell}{n+1}+\frac{2\ell^2}{(n+1)(n+2)}\right\}$$

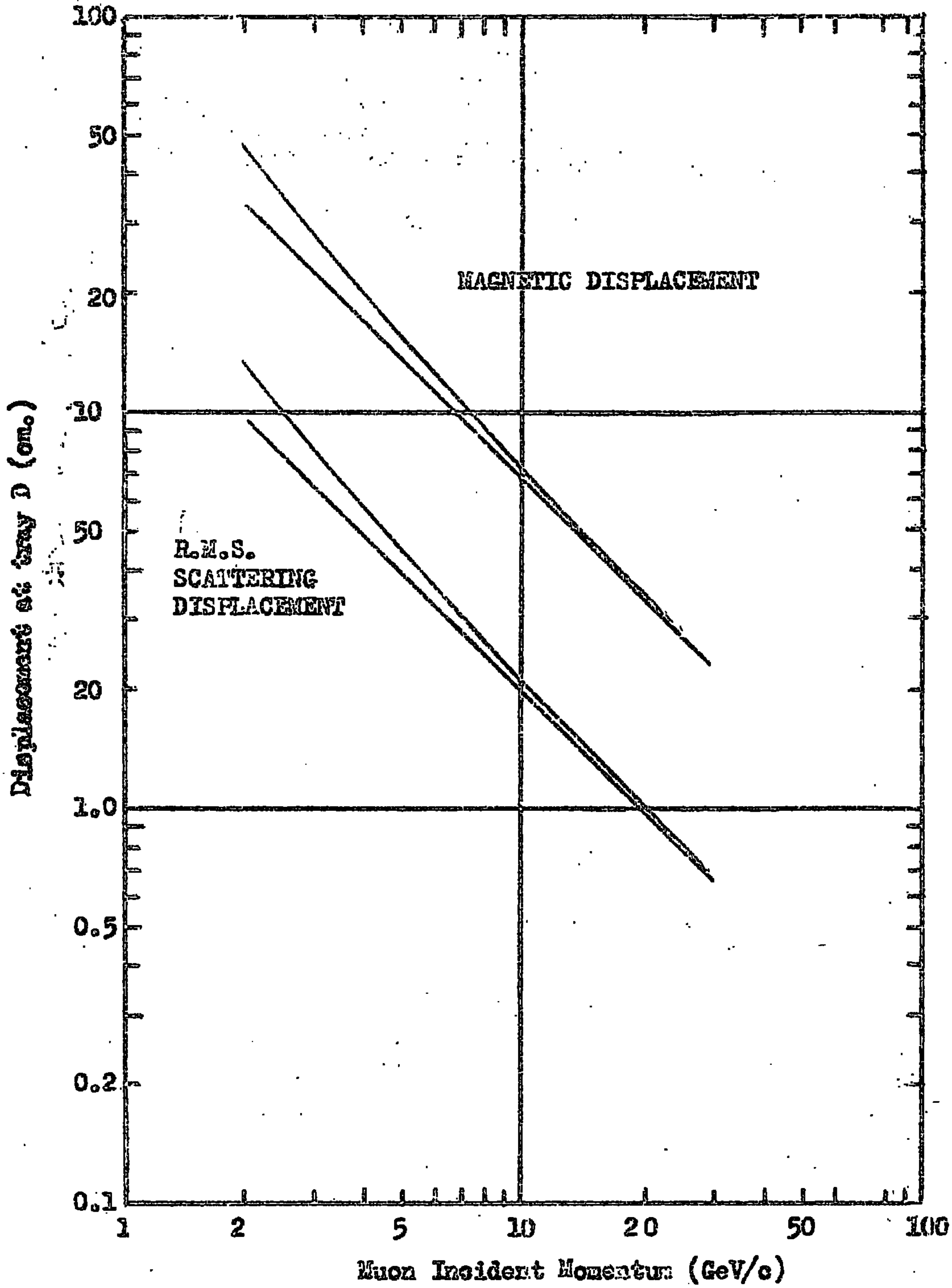

Fig. 3.5 The magnetic and r.m.s. projected scattering displacements at tray D as a function of momentum. The straight lines correspond to the case where energy loss in the iron is neglected.

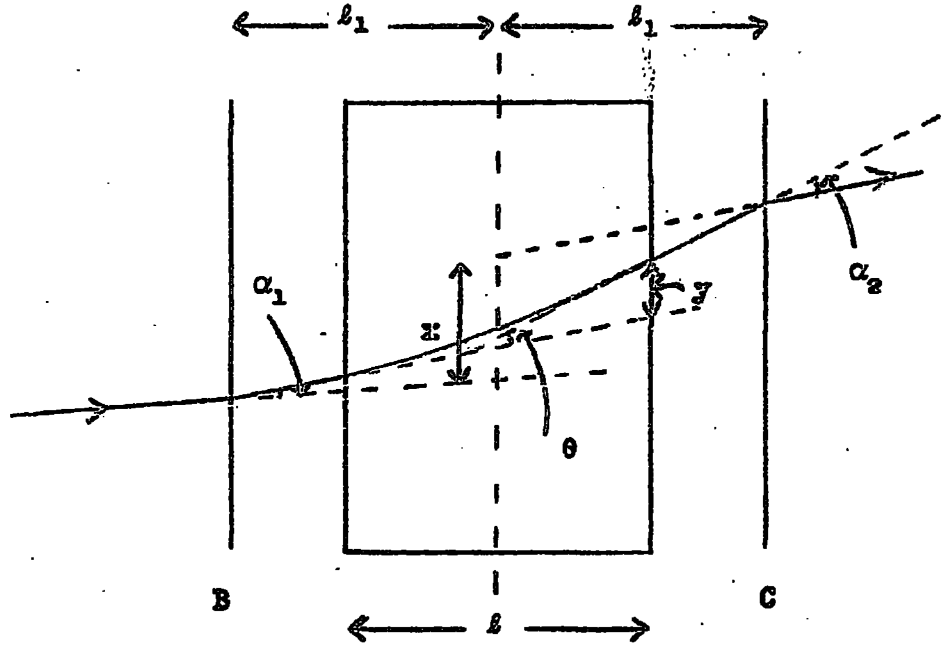

Fig. 3.6 Scattering of a particle in the magnet and flash-tube trays.

where $\langle y_o^2 \rangle$ is the mean square projected displacement for no energy loss, K = 21 MeV and X_o is the radiation length in iron. Δ and $\langle y^2 \rangle$ have been obtained for the magnet in use, the resulting curves being shown in fig. 3.5. From these curves it is seen that the ratio of r.m.s. scattering deflection to magnetic deflection is 0.30. It is possible to check this value experimentally, and to determine the magnitude of the accuracy of track location by studying the r.m.s. value of the discrepancy, x, at the centre of the magnet, with momentum. In fig. 3.6, x is given by

$$x = \ell_1 \alpha_1 + \ell_1 \alpha_2 + \left(y - \tfrac{1}{2} \ell \theta\right)$$

where the first two terms arise from scattering in flash tube trays B and C, and the bracketed term from scattering in the magnet.

The distribution in α_1, α_2 are Gaussian with standard deviation ($7.7 \times 10^{-3}\, p^{-1}$) radians with the momentum p of the particle in units of GeV/c.

The probability P(t, y, θ) that a particle of momentum p, suffers an angular deflection, θ (projected angle), and a projected displacement y in traversing t radiation lengths is given by:

$$P(t, y, \theta)\, dy\, d\theta = \frac{\sqrt{3}}{2\pi} \cdot \frac{\omega^2}{t^2} \exp\left[-\omega^2 \left(\frac{\theta^2}{t} - \frac{3 y \theta}{t^2} + \frac{3 y^2 \theta}{t^3} \right) \right] dy\, d\theta$$

where $\omega = \frac{2 p \beta}{E_s}$ and E_s = 21 MeV/c. (Rossi and Greisen, 1941). From this equation, the distribution in $\left(y - \frac{1}{2}\ell\theta\right)$ is found to be Gaussian with standard deviation $\frac{\ell}{\sqrt{12}} \langle \theta \rangle$ where $\langle \theta \rangle$ is the r.m.s. projected angle of scattering in the magnet. It follows that the distribution in x is a Gaussian with standard deviation

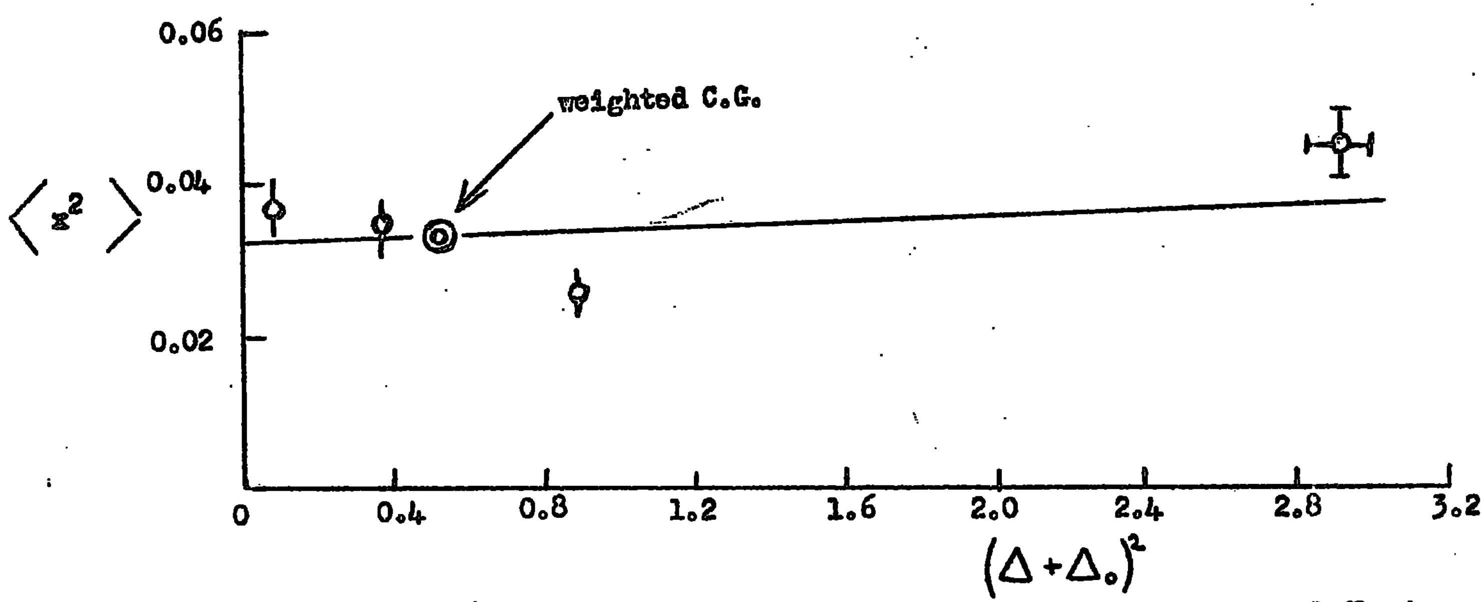

Fig. 3.7 The variation of mean square discrepancy with mean square deflexion.

$$\langle x_{\Delta+\Delta_0}\rangle^2 = 2\ell_1^2\sigma_\alpha^2 + \frac{\ell^2}{12}\langle\theta^2\rangle + x_0^2$$

$$= (\Delta+\Delta_0)^2\left(0.0157K^2 + 0.00032\right) + x_0^2 \quad (\text{t.s.})^2$$

The quantity x_0 is related to the r.m.s. uncertainty in track location, σ, at each flash tube tray through the geometrical constants of the instrument and is given by

$$x_0^2 = 4.913\,\sigma^2$$

The variation of $\langle x_{\Delta+\Delta_0}\rangle^2$ with $(\Delta+\Delta_0)^2$ for particles of sufficient energy for the energy loss in the magnet to be neglected is shown in figure 3.7. The theoretical line, assuming K = 0.30, is drawn through the weighted mean value. The fit to the experimental points is regarded as satisfactory.

For small displacements, $\langle x_{\Delta+\Delta_0}\rangle^2 = 4.913\sigma^2$, and the value of σ can be found from figure 3.4. The resulting values of σ are

(0.078 $\pm$ 0.003) t.s. for the projector method

and (0.047 $\pm$ 0.002) t.s. for the track simulator method.

An important quantity follows from the value of σ (or, more usually, from the value of the most probable error, P, given by P = 0.674 σ).

This quantity is termed the maximum detectable momentum (m.d.m.) and the corresponding probable error values of the m.d.m. for the present instrument are:

(224 $\pm$ 9) GeV/c for the projector method

and (369 $\pm$ 16)GeV/c for the track simulator method.

Table 3.2 The overall momentum distribution of particles.

Momentum Interval at centre of magnet. (GeV/c)	Total number of particles.	Rate (day^{-1})
1.56-3.66	78	11.1
3.66-5.76	82	11.6
5.76-9.83	113	16.0
9.83-20.3	250	35.5
20.3-31.1	202	28.7
31.1-51.3	190	27.0
51.3-73.8	100	14.2
73.8-215	173	24.6
>215	69	9.8
Total:	1257	178.5

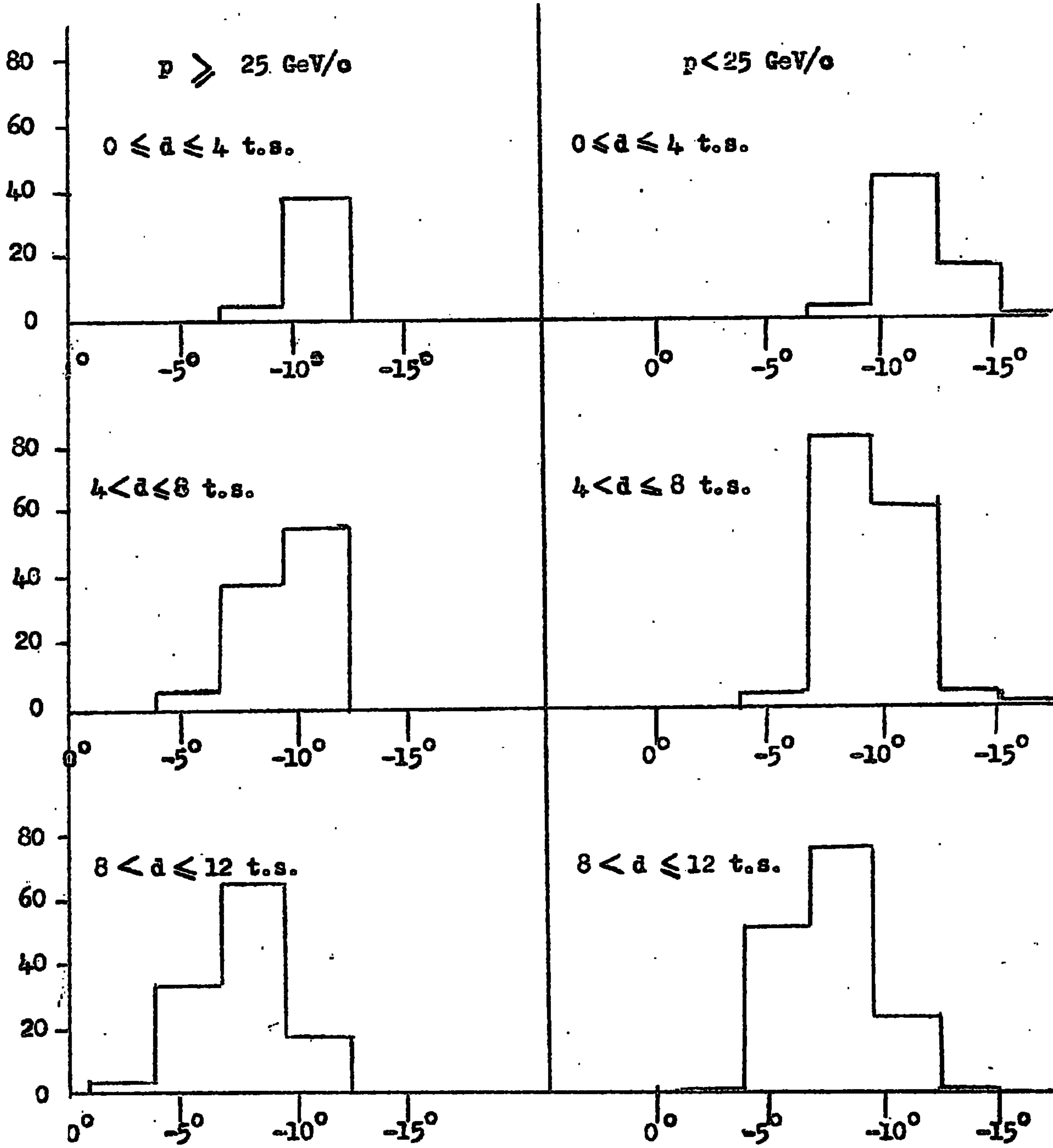

Fig. 3.8 Angular distribution of particles on emergence at D (d⩽12 t.s.)

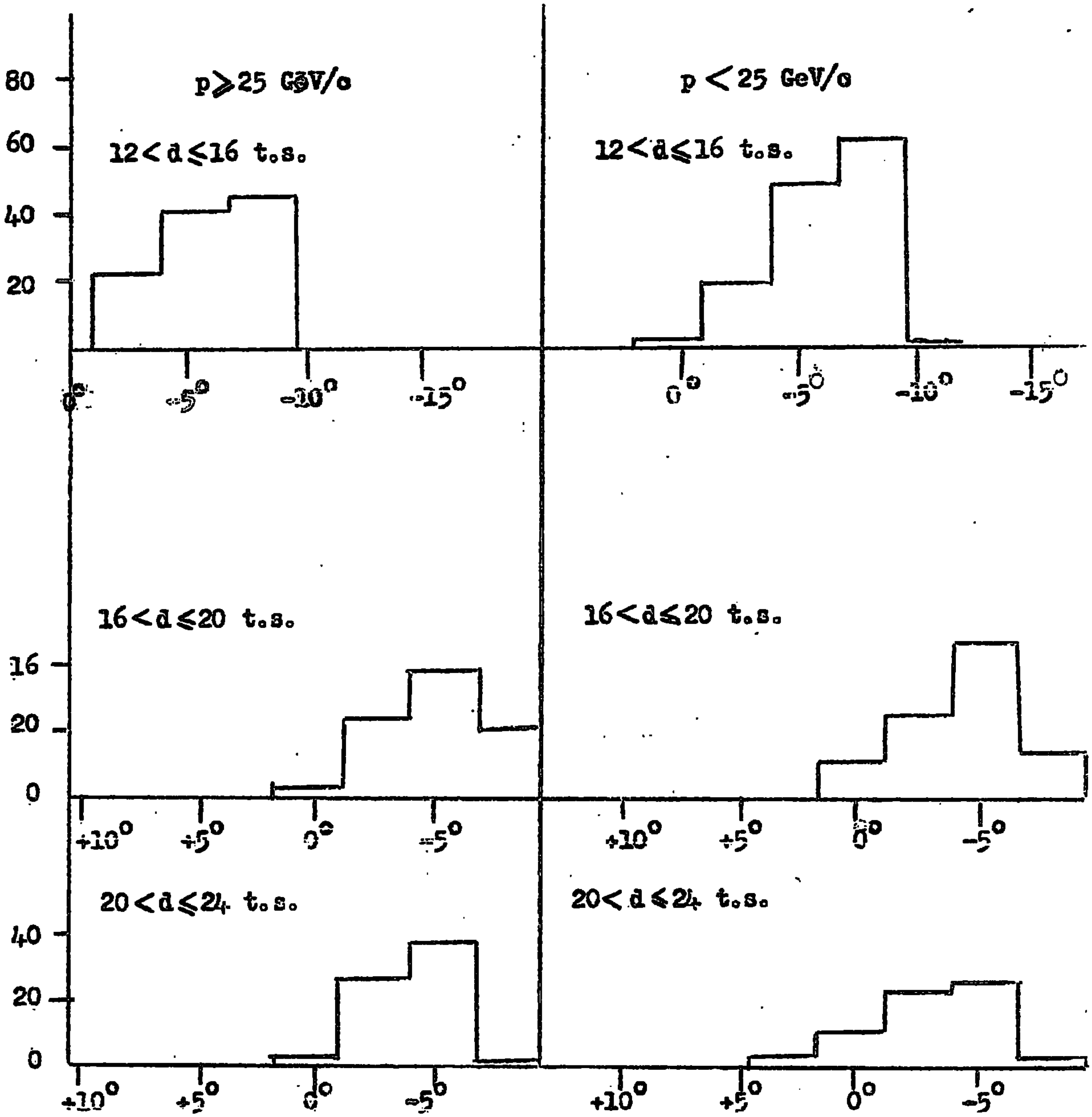

Fig. 3.9 Angular distribution of particles on emergence at D

($12 < d \leq 24$ t.s.)

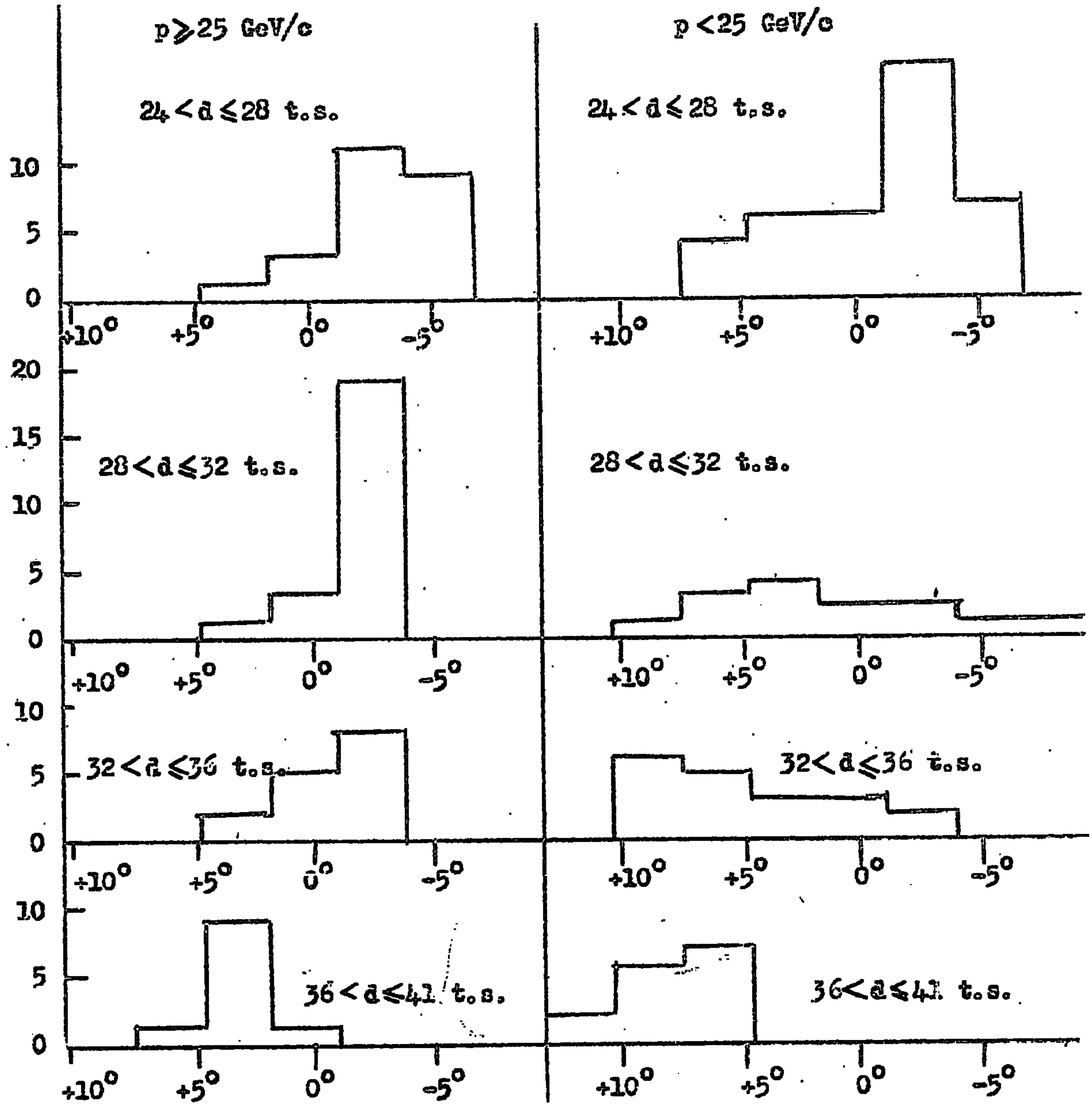

Fig. 3.10 Angular distribution of particles on emergence at D
($24 < d \leq 41$ t.s.)

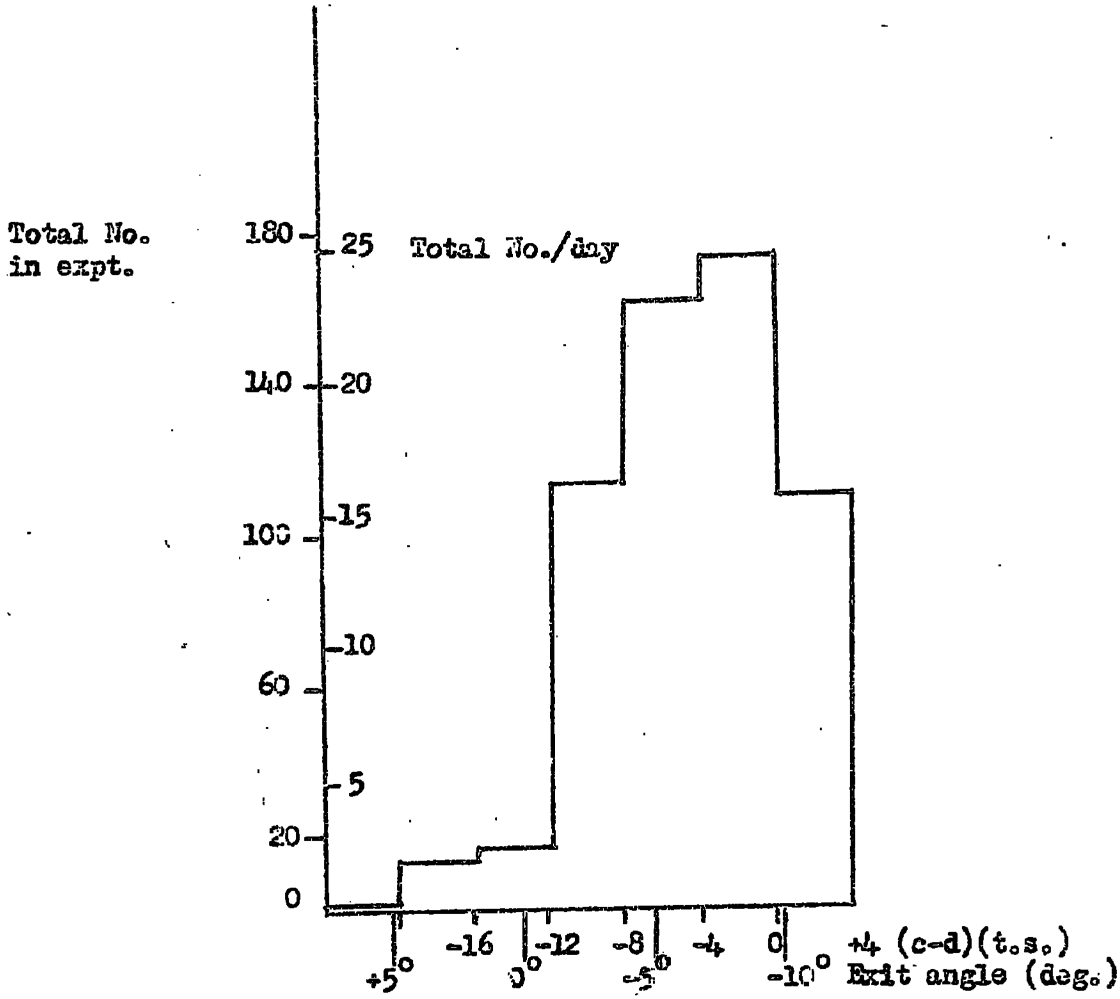

Fig. 3.11 Total angular distribution.

The simplest way in which the m.d.m. can be increased to higher values for this instrument is by increasing the values of ℓ_1 and ℓ_4.

3.5 The Accelerator Characteristics of the Spectrograph

As previously mentioned, the spectrograph is designed, not only to measured the spectrum of muons at large zenith angles, but also to act as a "source" of very fast particles (i.e. muons) in order that experiments investigating the interactions of these particles with matter can be carried out, and this section concerns what is loosely termed the 'accelerator characteristics' of the instrument.

It is thus necessary to know the momentum and spatial distribution of the emergent particles. The overall momentum distribution is shown in Table 3.2, where the total number of particles in the running time of the experiment and the particle rates are given.

The spatial distribution has been examined by analyzing the events with respect to angle of trajectory on emergence at the measuring level in flash tube tray D as a function of position at this level. The data are given in figures 3.8, 3.9, and 3.10 where division has been made between particles with momentum above and below 25 GeV/c. The sign convention is negative for downward directed tracks and positive for upward tracks.

The total distribution of exit angle is shown in figure 3.11, and Table 3.3. shows how the total is achieved as one progresses up tray D.

It is evident that the majority of particles emerge from tray D with angles between -1° and $-9^\circ 37'$ to the horizontal, and leave the tray between

Table 3.3 Distribution of particles with exit angle at D as a function of position in D.

Position in D. (t.s.)	+7°39' +4°47'	+4°47' +1°53'	+1°53' -1°0'	-1°0' -3°54'	-3°54' -6°47'	-6°47' -9°37'	-9°37' -12°25') Exit Angle
0 - 4						4	38
4 - 8					5	38	55
8 - 12				4	34	66	18
12 - 16				22	40	45	
16 - 20			3	24	38	21	
20 - 24			2	26	37	1	
24 - 28		1	3	11	9		
28 - 32		1	3	19			
32 - 36		2	5	8			
36 - 41	1	9	1				

flash tube numbers 8 and 28. The angular spread on emergence both in the plane under consideration and in the perpendicular plane dictates that a detector used to study interactions must be placed as close to tray D as possible.

For studies on the interactions of particles of the highest energies, as long a path length in subsequent detectors as possible is required. With the present arrangement some 5 metres is immediately available, with a possible extension to about 8 metres if a temporary partition is removed.

Chapter IV

THE THEORETICAL MOMENTUM SPECTRA OF SEA-LEVEL MUONS AT LARGE ZENITH ANGLES

4.1 The method of calculation

The objects of the experiment are two-fold:

i) to examine the validity of the model used for studying the propagation of particles through the atmosphere, and

ii) to examine the nature of the particles which give rise to the muons penetrating to sea-level.

It will be shown that at low energies ($E_\mu \lesssim 30$ GeV) the expected spectra of muons at sea-level are not sensitive to the nature of the parent particles so that object (i) is attained by analysing the low energy results. At higher energies the spectra are sensitive and it is in this region that the relative contributions of the various parents can, in principle, be determined.

As was pointed out in §1.4, the form of analysis is to take the vertical sea-level muon spectrum and, assuming in turn that the parents are either pions or K-mesons, determine the pion and K-meson spectra at production, and thence derive the expected sea-level muon spectra at large zenith angles.

4.2 The expected sea-level spectra of muons from pions only

On the basis that muons are the progeny of pions only, the muon differential energy spectrum at production, $M(E,\theta)$, at a zenith angle,

θ deg.	(x/ρ) km.	$B_{\pi}(\theta)$ GeV.	$B_K(\theta)$ GeV.
0	6.36	90	509
60	13	184	987
70	18	255	1445
80	32	453	2590
82	38	538	3090
84	44	623	3590
86	51	722	4130
88	57	807	4580
90	61	863	4950

Table 4.1 The variation of the function $B(\theta)$ with zenith angle.

θ, is given by the following expression:

$$M(E,\theta) = \frac{F_\pi(E/r)}{r} \cdot \frac{\lambda_\pi}{\lambda_p} \cdot \frac{B_\pi(\theta)}{E} \sum_{n=0}^{\infty} \frac{(-\lambda_\pi/\lambda')^n}{(n+1) + B_\pi(\theta)/E} \qquad 4.1$$

(Barrett et al (1952)), where

$$r = \frac{\text{mass of muon}}{\text{mass of pion}} = 0.76,$$

$F_\pi(E/r)$ is the pion differential spectrum at production,

λ_π, λ_p are the absorption mean free paths for pions and non-pion producers of pions respectively,

$B_\pi(\theta)$ is a function of zenith angle and is given by the relation $B_\pi(\theta) = \frac{B(x/\rho)_\theta}{6.36}$, where ρ is the density of the atmosphere in units of gm.cm^{-3} at a depth x gm.cm^{-2}, and $(\lambda')^{-1} = \lambda_p^{-1} - \lambda_\pi^{-1}$

The $\pi \rightarrow \mu$ decay kinematics are simplified to the extent that the pion energy, E_π, is assumed proportional to the muon energy, E, the constant of proportionality being r^{-1}. (The effect of 'decay spread' - the fact that muons of a certain energy come from pions of a range of energies - is neglected.)

If $\lambda_p = \lambda_\pi$, equation 4.1 simplifies to the form

$$M(E,\theta) = F_\pi(E/r) . r^{-1}\left[1 + E/B_\pi(\theta)\right]^{-1} \qquad 4.2$$

The justification for $\lambda_p = \lambda_\pi$ is given in the reviews by Sitte (1961) and Perkins (1961). Further, it is assumed that production of muons takes place at a unique depth in the atmosphere (83 gm.cm^{-2}). The values of the function, $B_\pi(\theta)$, used are shown in Table 4.1. Also shown are the

E_μ (GeV)	$M(E_\mu)$ ($cm^{-2} st^{-1} sec^{-1} GeV^{-1}$)
10	2.50×10^{-4}
20	3.30×10^{-5}
50	2.20×10^{-6}
100	2.50×10^{-7}
200	2.55×10^{-8}
500	1.11×10^{-9}
1000	1.03×10^{-10}

Table 4.2. The vertical muon differential intensity at production.

E_π (GeV)	$F_\pi(E_\pi)$ ($cm^{-2}st^{-1}sec^{-1}GeV^{-1}$)	E_K (GeV)	$F_K(E_K)$ ($cm^{-2}st^{-1}sec^{-1}GeV^{-1}$)
13.2	2.10×10^{-4}	12	4.90×10^{-4}
26.3	3.06×10^{-4}	20	1.08×10^{-4}
65.7	2.59×10^{-6}	50	7.00×10^{-6}
132	4.01×10^{-7}	100	8.30×10^{-7}
264	6.21×10^{-8}	250	5.10×10^{-8}
657	5.51×10^{-9}	500	6.30×10^{-9}
1320	9.50×10^{-10}	1000	7.90×10^{-10}

Table 4.3. The pion and K-meson differential intensities at production.

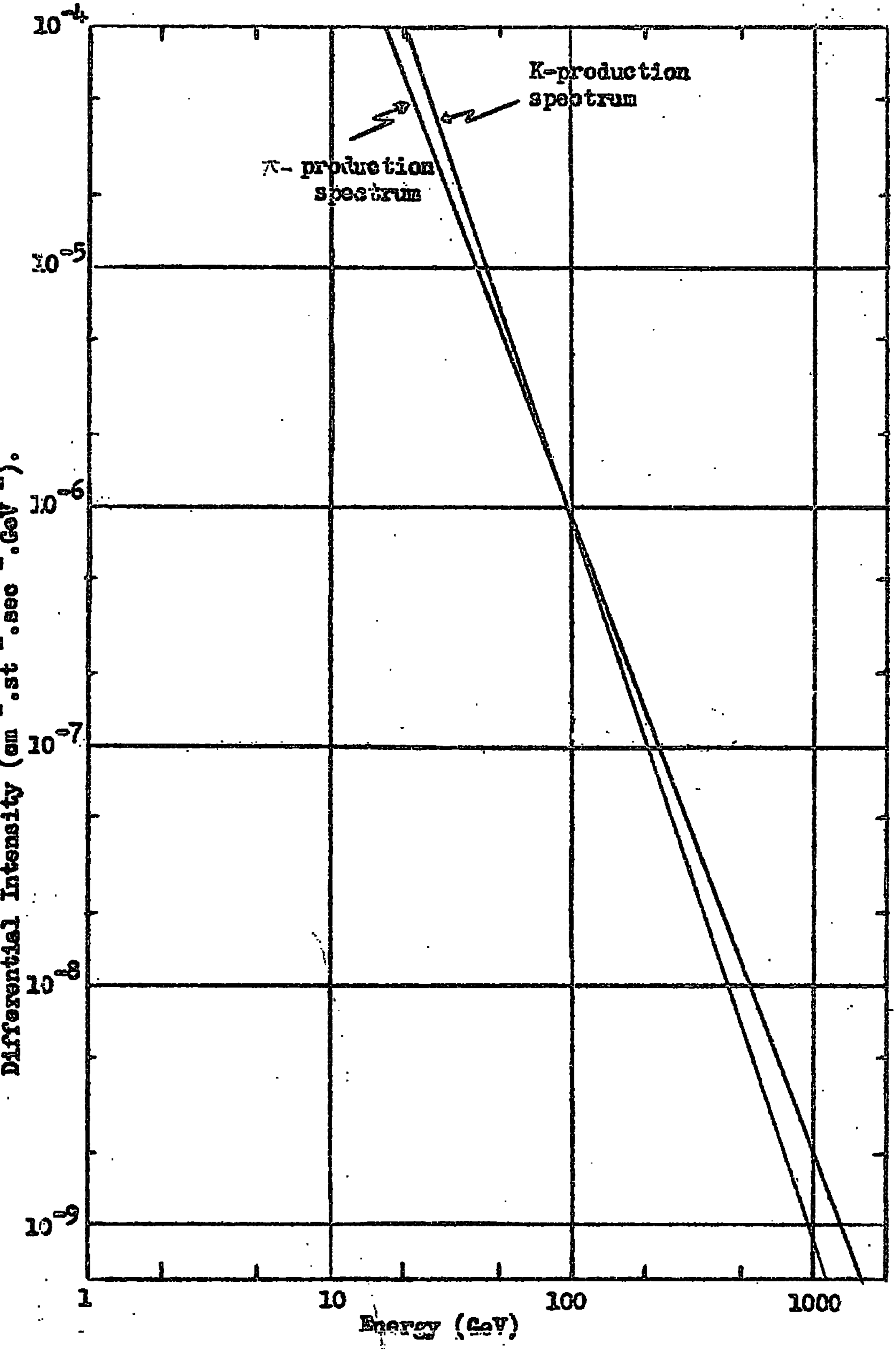

Fig. 4.1 The pion and K-meson production spectra.

θ (deg)	E_μ (GeV)	$M(E_\mu,\theta)$ ($cm^{-2}st^{-1}sec^{-1}GeV^{-1}$)	θ (deg)	E_μ (GeV)	$M(E_\mu,\theta)$ ($cm^{-2}st^{-1}sec^{-1}GeV^{-1}$)
60	5.60	1.12×10^{-3}	70	8.00	4.34×10^{-4}
	6.80	6.73×10^{-4}		9.30	2.86×10^{-4}
	8.90	3.20×10^{-4}		11.6	1.54×10^{-4}
	13.7	9.92×10^{-5}		16.0	6.81×10^{-5}
	21.9	3.12×10^{-5}		24.5	2.02×10^{-5}
	38.0	5.78×10^{-6}		41.0	5.33×10^{-6}
	70.0	1.03×10^{-6}		73.0	9.83×10^{-7}
	134	1.41×10^{-7}		138	1.45×10^{-7}
	300	1.07×10^{-8}		305	1.22×10^{-8}
	800	3.94×10^{-10}		804	5.07×10^{-10}
80	15.8	7.24×10^{-5}	82	19.0	4.32×10^{-5}
	17.0	5.83×10^{-5}		20.8	3.35×10^{-5}
	19.1	4.29×10^{-5}		23.1	2.52×10^{-5}
	23.8	2.25×10^{-5}		27.5	1.54×10^{-5}
	32.5	9.70×10^{-6}		36.2	7.40×10^{-6}
	48.7	3.27×10^{-6}		52.8	2.73×10^{-6}
	82.0	8.03×10^{-7}		85.8	7.26×10^{-7}
	145	1.49×10^{-7}		148	1.44×10^{-7}
	318	1.43×10^{-8}		320	1.44×10^{-8}
	830	6.97×10^{-10}		858	6.84×10^{-10}

Table 4.4. Muon differential spectra at production at large zenith angles.

θ (deg)	E_μ (GeV)	$M(E_\mu,\theta)$ ($cm^{-2}st^{-1}sec^{-1}GeV^{-1}$)	θ (deg)	E_μ (GeV)	$M(E_\mu,\theta)$ ($cm^{-2}st^{-1}sec^{-1}GeV^{-1}$)
84	25.0	2.05×10^{-5}	86	36.0	7.63×10^{-6}
	27.0	1.64×10^{-5}		38.1	6.38×10^{-6}
	29.9	1.24×10^{-5}		42.0	5.08×10^{-6}
	34.1	8.86×10^{-6}		46.5	3.91×10^{-6}
	43.0	4.74×10^{-6}		56.0	2.38×10^{-6}
	60.4	1.98×10^{-6}		74.2	1.11×10^{-6}
	93.0	5.72×10^{-7}		107	3.42×10^{-7}
	155	1.32×10^{-7}		172	9.96×10^{-8}
	332	1.40×10^{-8}		350	1.22×10^{-8}
	860	7.48×10^{-10}		880	7.43×10^{-10}
88	58.0	2.15×10^{-6}	90	116	3.13×10^{-7}
	61.0	1.90×10^{-6}		117	3.07×10^{-7}
	65.0	1.60×10^{-6}		118	3.02×10^{-7}
	71.0	1.28×10^{-6}		125	2.59×10^{-7}
	81.0	9.00×10^{-7}		132	2.17×10^{-7}
	99.0	4.56×10^{-7}		152	1.46×10^{-7}
	143	1.71×10^{-7}		190	7.67×10^{-8}
	205	6.09×10^{-8}		270	2.80×10^{-8}
	388	9.61×10^{-9}		450	6.19×10^{-9}
	935	6.53×10^{-10}		1000	5.46×10^{-10}

Table 4.5. Muon differential spectra at production at large zenith angles.

values of $(x/p)_\theta$ at the production level.

The muon production spectrum in the vertical direction, M(E,0), has been derived in a straightforward way from the sea-level muon spectrum of Hayman and Wolfendale (1962), and the intensities are given in Table 4.2.

Using equation 4.2, with $B_\pi(\theta) \doteq 90$ GeV, and the muon production spectrum, M(E,0), the pion production spectrum, $F_\pi(E/r)$, has been evaluated under the assumption that pions alone are the parents of muons. The intensities are given in Table 4.3, and the spectrum is plotted in figure 4.1.

Starting with this pion production spectrum, the muon differential spectrum at production was calculated for various angles between 60° and 90° to the zenith using equation 4.2 and the appropriate values for The intensities are given in Tables 4.4 and 4.5. The momenta at production were converted to sea-level momenta by use of figure 4.2 (Allen and Apostolakis 1961) which shows the variation with zenith angle of the effect of the total energy loss on the energy at sea-level for muons.

Corrections were applied to the sea-level intensity for μ-e decay using the survival probability curves shown in figure 4.3 (Allen and Apostolakis 1961). A correction for cell width was also taken into account according to the relation

$$N(p)_{s.l} = N(p)_{83} \frac{(dp/dx)_{83}}{(dp/dx)_{s.l.}}$$

where the subscripts refer to sea-level and production level (83 gm.cm^{-2}). Figure 4.4 demonstrates the importance of this correction, particularly

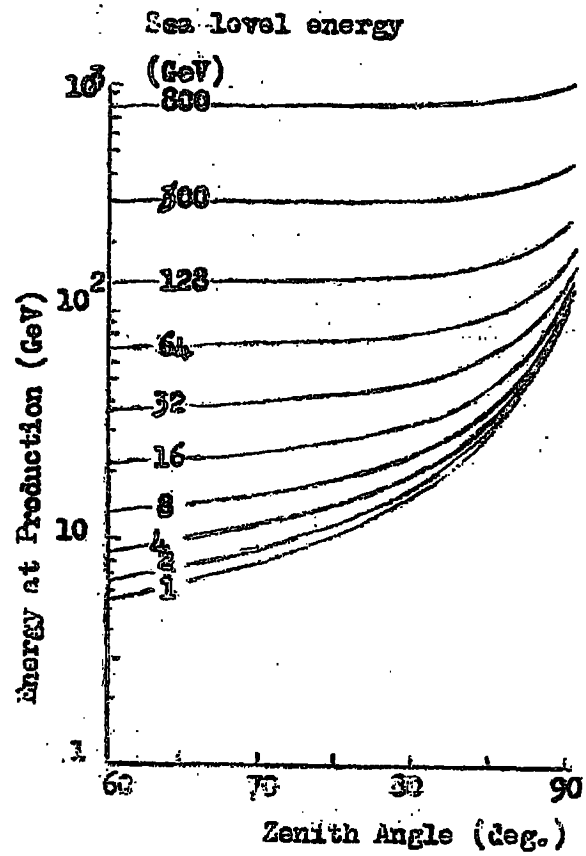

Fig. 4.2 The variation with zenith angle of the energy at production of muons of a given energy at sea-level.

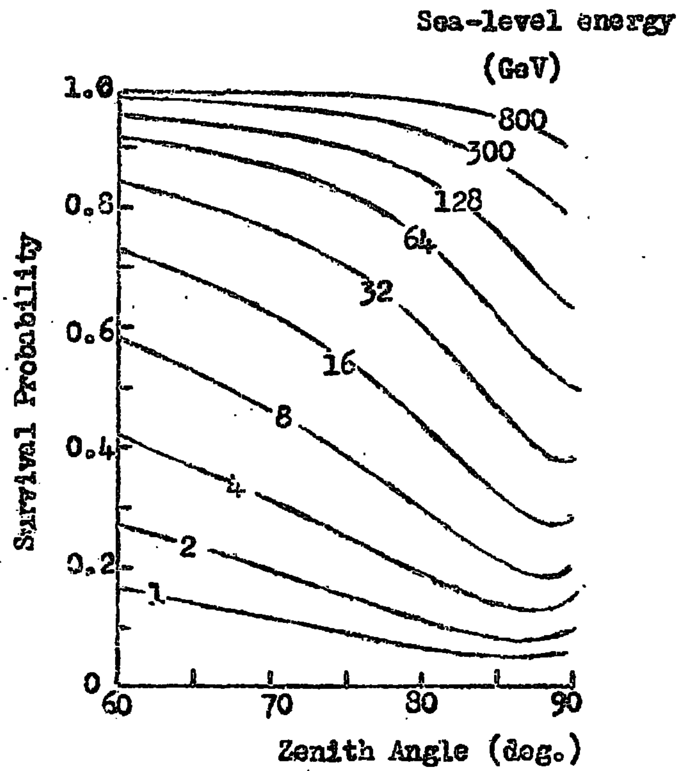

Fig. 4.3 The variation with zenith angle of the survival probability of muons of a given energy at sea-level.

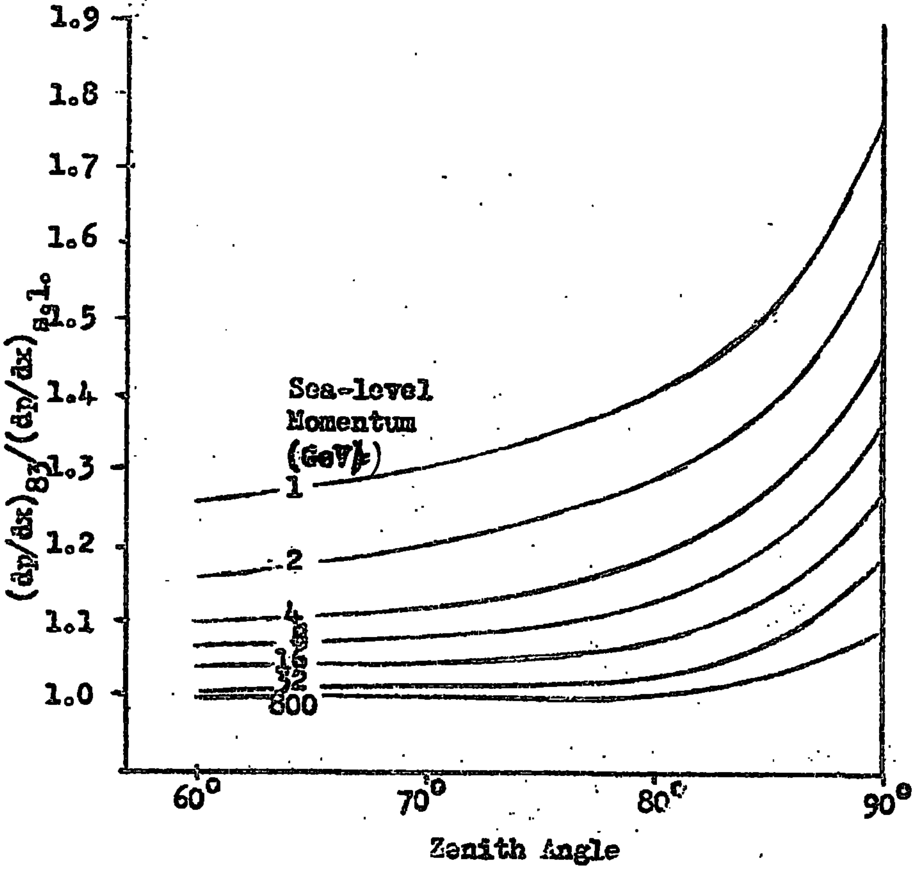

Fig. 4.4 The correction factor due to cell width, with sea-level momentum as parameter.

between 80° and 90° to the zenith. A further correction to take into consideration the effect of scattering of muons in the atmosphere is extremely important particularly for low momentum particles ($<$(15-20) GeV/c) incident at the larger zenith angles. The ratio of corrected to uncorrected distributions is given approximately by the following expression:

$$\frac{g(\varphi_0)}{f(\varphi_0)} = \exp\left(\frac{K^2\sigma^2}{2}\right)$$

(Lloyd and Wolfendale 1955) where K can be derived from the variation with zenith agle of the intensity, I, of particles of a particular energy. This variation can be approximated to an expression of the form

$$I = I_0 \exp(-K\theta)$$

The variation of the r.m.s. angle of scattering, σ, with zenith angle as a function of sea-level momentum is shown in figure 4.5 (Allen and Apostolakis 1961). Figure 4.6 shows the variation of $\exp(+\frac{K^2\sigma^2}{2})$ with zenith angle as a function of sea-level momentum.

The angular spread of pions at production and the $\pi\to\mu$ angle of decay have been ignored as has the effect of geomagnetic deflection (this latter is justified because the spectrograph axis lies almost along the direction of geomagnetic north).

The predicted sea-level muon momentum spectra are shown in figure 4.7, together with the measured vertical spectrum (Hayman and Wolfendale 1962). The dotted lines are intensities uncorrected for scattering in the atmosphere whilst the solid lines are corrected for scattering.

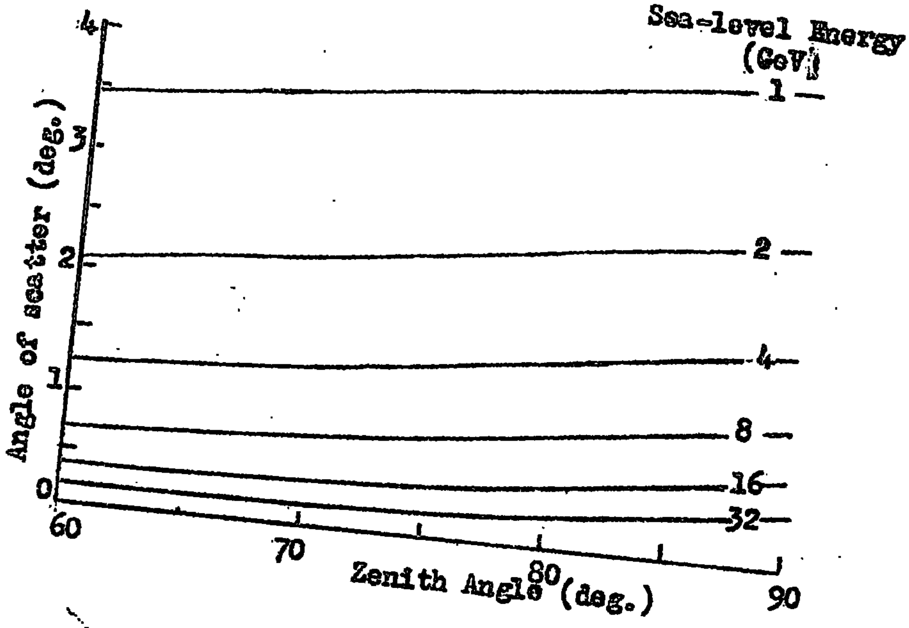

Fig. 4.5 The r.m.s. angle of scattering plotted as a function of zenith angle of muons of a given energy at sea-level.

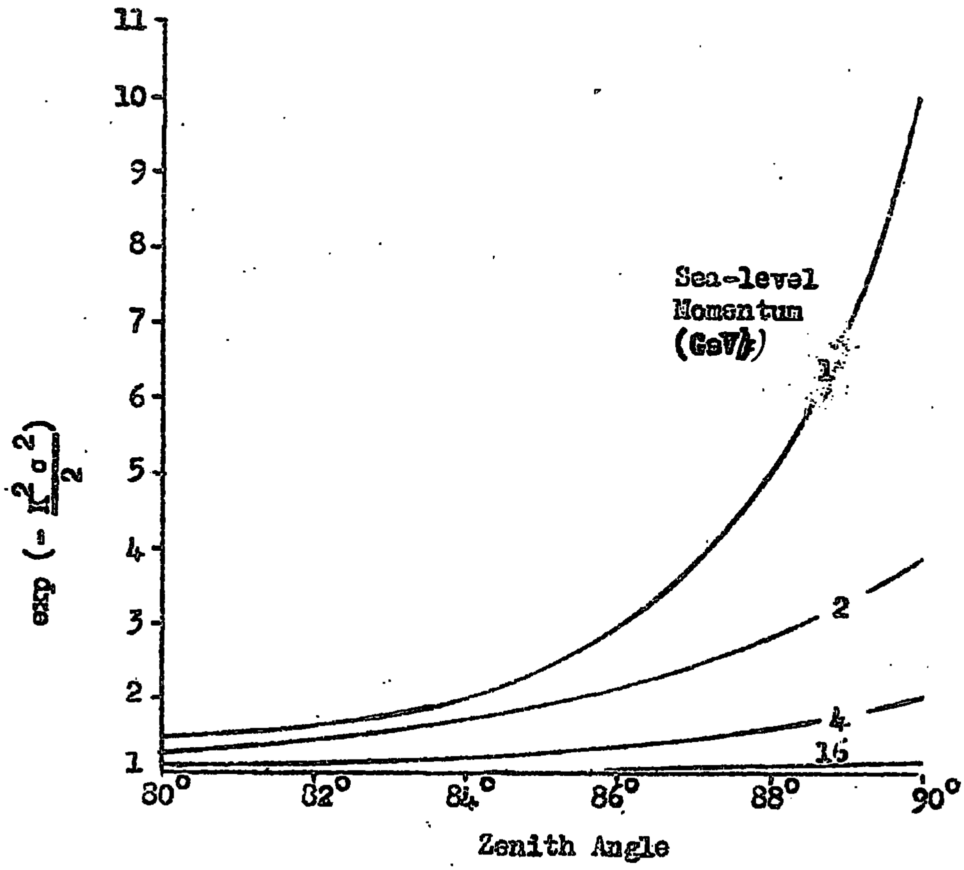

Fig. 4.6 The variation of $\exp\left(-\frac{K^2\sigma^2}{2}\right)$ with zenith angle, with sea-level momentum as parameter.

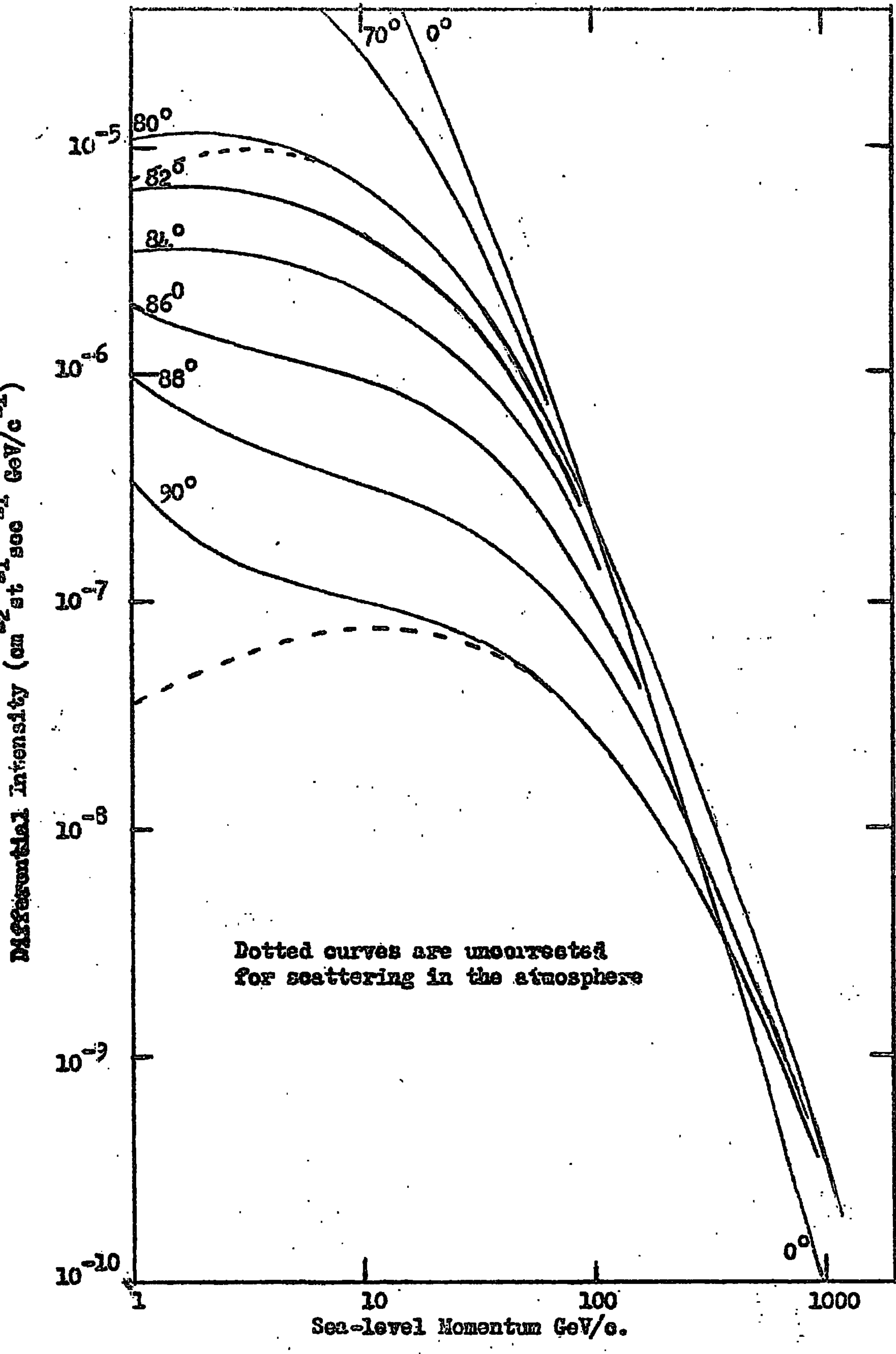

Fig. 4.7 The theoretical muon sea-level spectra at large zenith angles. Also shown in the measured vertical spectrum (Hayman and Wolfendale, 1962).

As can be seen it is expected that the vertical spectrum will cross the 80° spectrum at about 100 GeV/c, and the 90° spectrum at about 350 GeV/c. The 80° and 90° spectra are expected to cross at about 1000 GeV/c., thus emphasising the importance of using cosmic ray muons at large zenith angles to study high energy phenomena.

4.3 <u>The expected sea-level spectra of muons of K-meson origin only</u>

Using the same approach as in § 4.2, the muon production spectra were derived assuming that muons comefrom the $K_{\mu 2}$ decay mode only. The K-meson production spectrum is shown in figure 4.1 and the intensities are given in Table 4.3. The values for $B_K(\theta)$ used to evaluate equation 4.2 are shown in Table 4.1.

The ratio of the inclined muon spectra at production, derived from the $K_{\mu 2}$-production spectrum and the π-production spectrum are shown in figure 4.8. The ratio of the observed to expected rates of events (on the basis of pion origin alone) converted to the production level will then givenan indication of the origin (pions or K-mesons) of muons detected at sea-level when plotted on this graph.

However, whilst the $K_{\mu 2}$ mode of decay has a branching ratio of 58% and will therefore produce more muons than any other mode for K-mesons, it is thought that the other decay modes will also be important (e.g. $K^{\pm}_{\pi 2}$ with branching ratio 26%, and $K^{0}_{\pi 2}$ with branchingratio 34.5%). The effect of other decay modes has been considered by Osborne (private communication). The decay schemes considered are shown in Table 4.6.

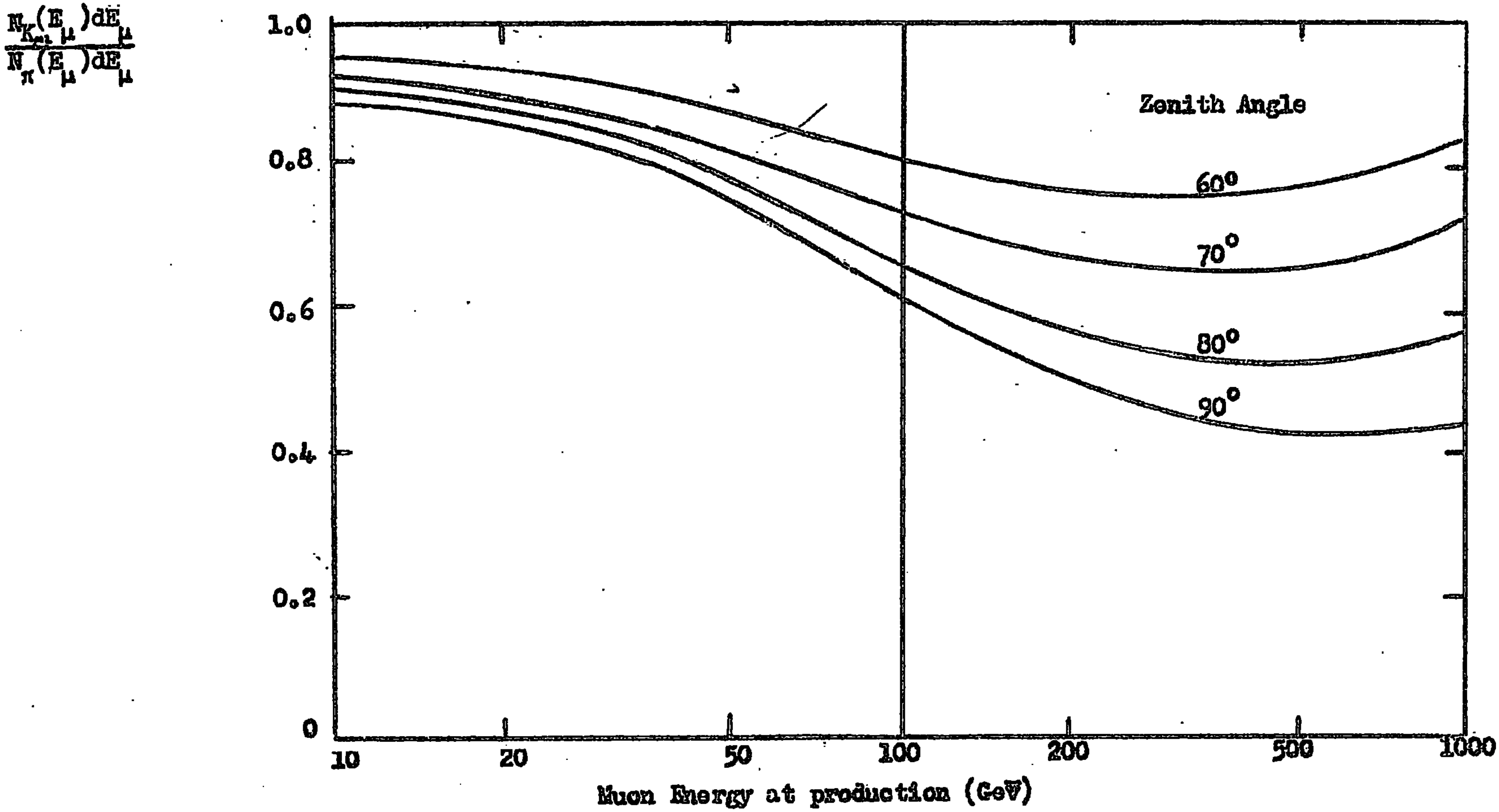

Fig. 4.8 Ratio of the muon production spectra as a function of energy at production for various zenith angles.

Decay Mode	Branching Ratio
$K^{\pm}_{\mu 2} \to \mu^{\pm} + \nu$	58%
$K^{\pm}_{\pi 2} \to \pi^{\pm} + \pi^{0}$	26%
$K^{\pm}_{\pi 3} \to \pi^{\pm} + \pi^{+} + \pi^{-}$	6%
$K^{\pm}_{\pi 3} \to \pi^{\pm} + \pi^{0} + \pi^{0}$	2%
$K^{\pm}_{\mu 3} \to \mu^{\pm} + \pi^{0} + \nu$	4%
$K^{0}_{\pi 2} \to \pi^{+} + \pi^{-}$	34.5%
$K^{0}_{\mu 3} \to \mu^{\pm} + \nu + \pi^{\mp}$	16%
$K^{0}_{e 3} \to e^{\pm} + \nu + \pi^{\mp}$	17%
$K^{0}_{\pi 3} \to \pi^{+} + \pi^{-} + \pi^{0}$	6.5%

Table 4.6 The decay modes of K-mesons considered by Osborne (§4.3)

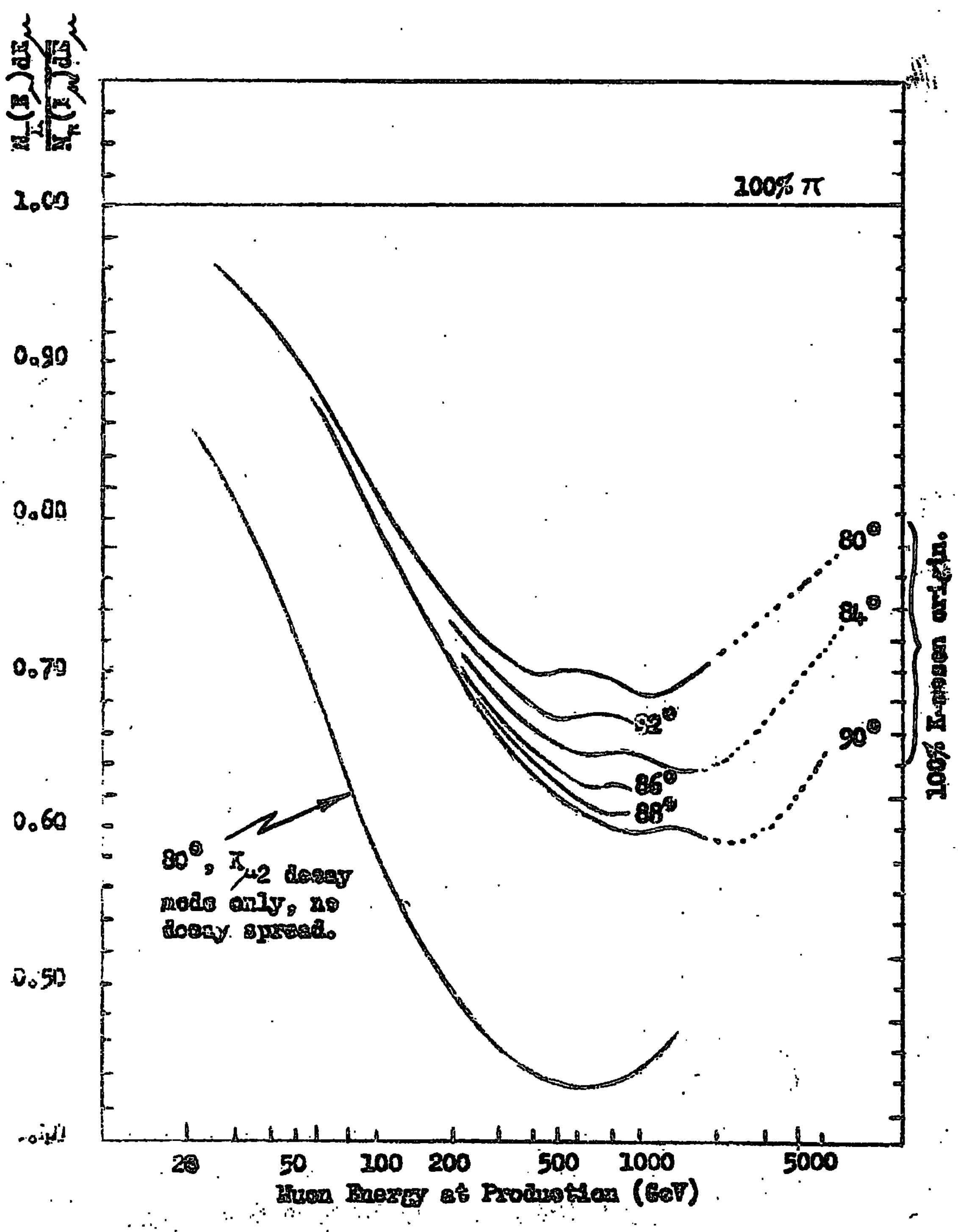

Fig. 4.9 Ratio of muon production spectra at large zenith angles.

Osborne has assumed that the frequency of production of the four K-meson states is given by $N(K^+) = N(K^o)$, $N(K^-) = N(\overline{K}^o)$, and has derived the K-meson production spectrum. From this the muon production spectrum has been calculated, and the final ratio of Muons from all K-mesons to muons from all pions, $\frac{N_K(\mathcal{E}_\mu)\,d\mathcal{E}_\mu}{N_\pi(\mathcal{E}_\mu)\,d\mathcal{E}_\mu}$, is shown in figure 4.9 with zenith angle as parameter. Also included in the calculation is an estimate of the effect of "decay spread" (§4.2). A horizontal line through $\frac{N_K(\mathcal{E}_\mu)\,d\mathcal{E}_\mu}{N_\pi(\mathcal{E}_\mu)\,d\mathcal{E}_\mu} = 1$ represents the case for 100% pions as parents of muons. It is interesting to note that, as the number of different decay modes of K-mesons considered is increased, so the ratio, $\frac{N_K(\mathcal{E}_\mu)\,d\mathcal{E}_\mu}{N_\pi(\mathcal{E}_\mu)\,d\mathcal{E}_\mu}$, becomes closer to unity, calling for a higher degree of statistical accuracy before any conclusions concerning muon origin can be made. (c.f. the curve for a zenith angle of 90^o in figures 4.8, 4.9).

4.4 The acceptance characteristics of the spectrograph

In order to compare the theory with the experimental observations, the method adopted was to predict the number of events expected during the running time of the experiment for particular momentum bands in various zenith angular ranges (the selected momentum bands and zenith angular ranges being shown in Table 3.1). These predictions were compared with the observed number of events and the observed intensities were then calculated.

Before this can be done, however, a knowledge of the acceptance characteristics of the spectrograph is required. The probability of a particle being accepted by the spectrograph has been found graphically, the quantity determined being called the "acceptance function" measured in units of "cm.^{2}sterad." The expected rate of events recorded then follows as the product of this function and the intensity.

The acceptance function can be written as the product

$$A_o(p,\theta).\eta.G. \quad \text{where}$$

$A_o(p,\theta)$ is the geometric function determined by the overall size of the geiger counter trays, η is the probability of none of the appropriate counters in the instrument being quenched at the instant when the particle (of momentum, p, at zenith angle, θ) passes through them, and G is the average probability of a particle not traversing an insensitive region in any counter tray on its passage through the instrument.

In the present case, η = 87.3% and G = 54.6%.

To obtain the function, $A_o(p,\theta)$, the following procedure was adopted. A cursor describing the trajectory of a particle of momentum, p, was placed on a scale diagram of the side elevation of the spectrograph such that the particle arrived at an incident zenith angle, θ, and passed through a point in geiger tray D. Keeping this latter point fixed the incident zenith angle was allowed to vary by $\pm\delta\theta$, and the extreme values of the position in geiger tray A were noted. This was repeated for the whole of geiger tray D for particles deflected both upwards and downwards, and the whole process was repeated for various incident momenta and zenith angles. The vertical range in geiger tray A which is limited by the extreme edges of the geiger trays B and C and the magnet (and sometimes by the extent of A itself), was plotted against position in tray D as

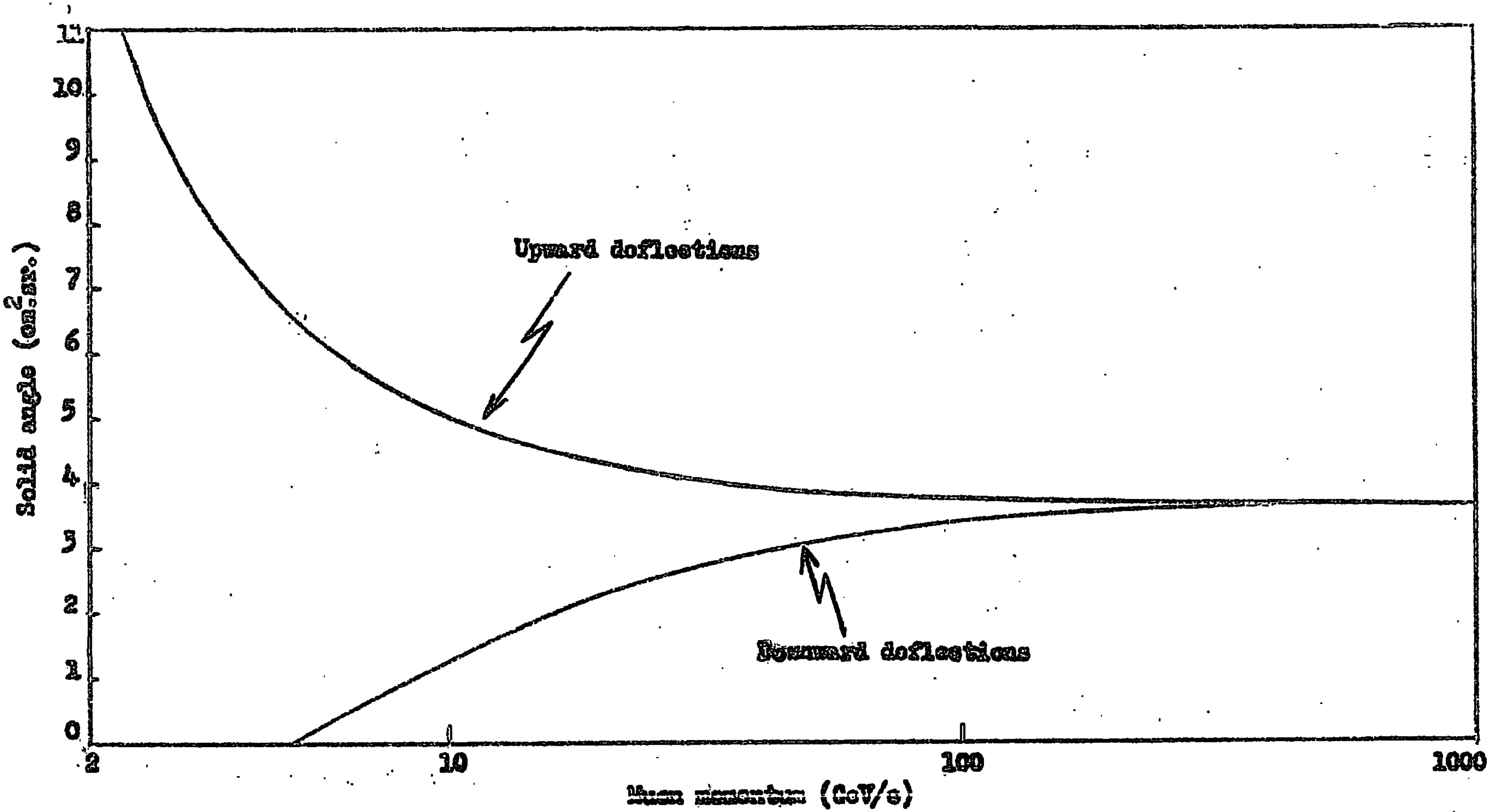

Fig. 4.10 The acceptance function, $A_{\theta}(p,\theta)$, for the spectrograph over the zenith angular range 77.5°-80°.

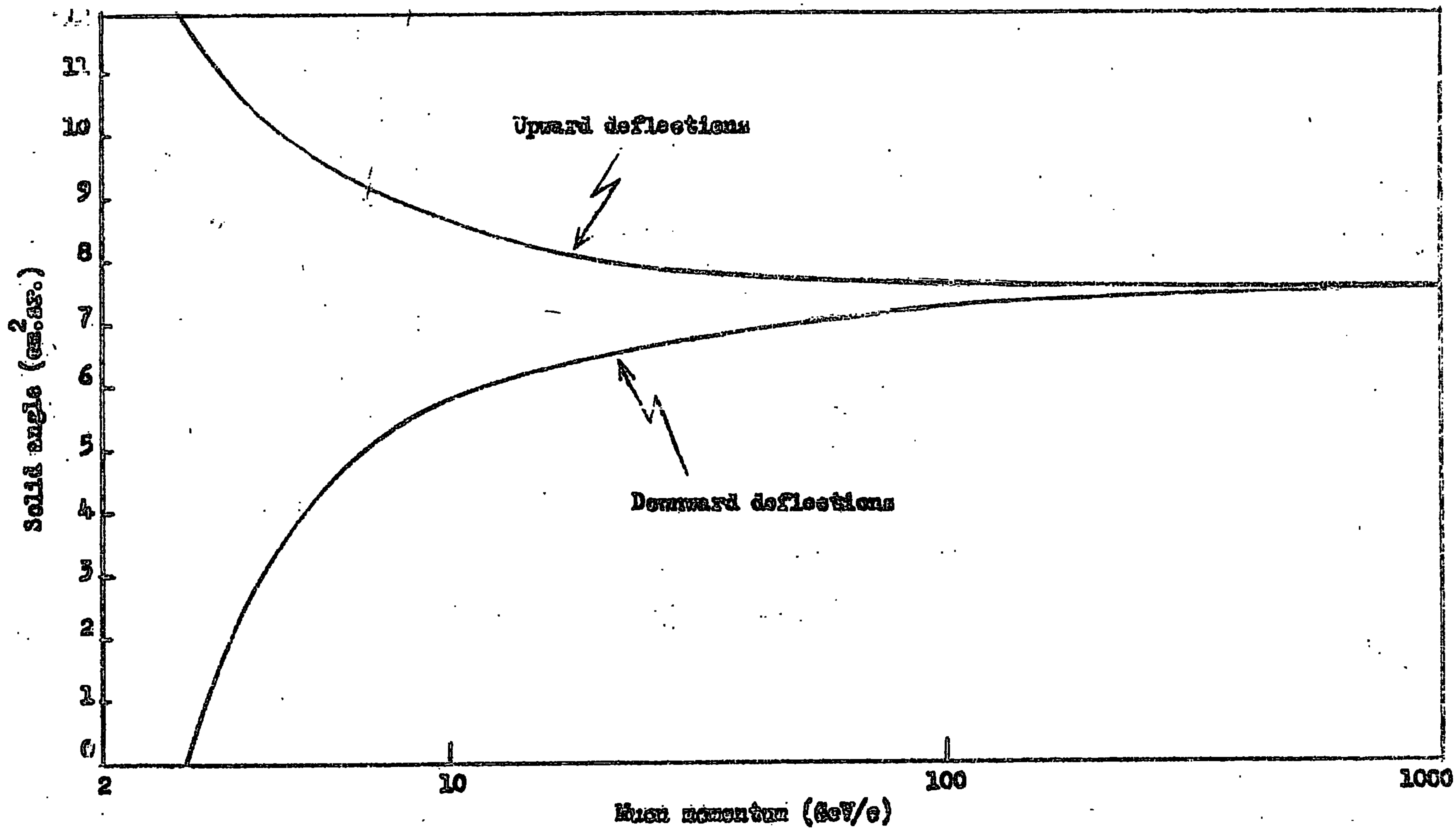

Fig.4.11 The acceptance function, $A_o(p,\theta)$, for the spectrograph over the zenith angular range 80°–82.5°.

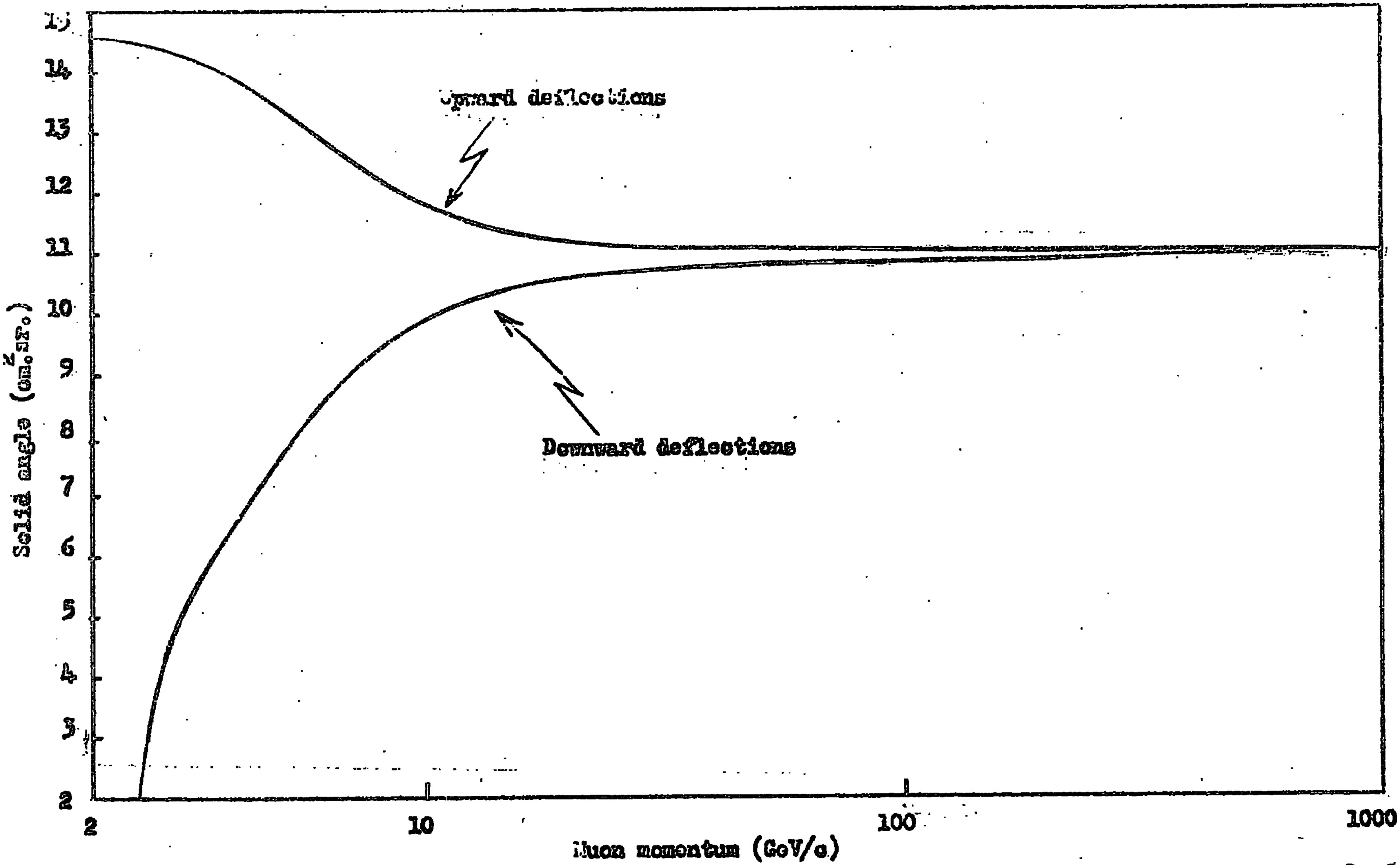

Fig. 4.12 The acceptance function, $A_o(p,\theta)$, for the spectrograph over the zenith angular range 82.5°-85°

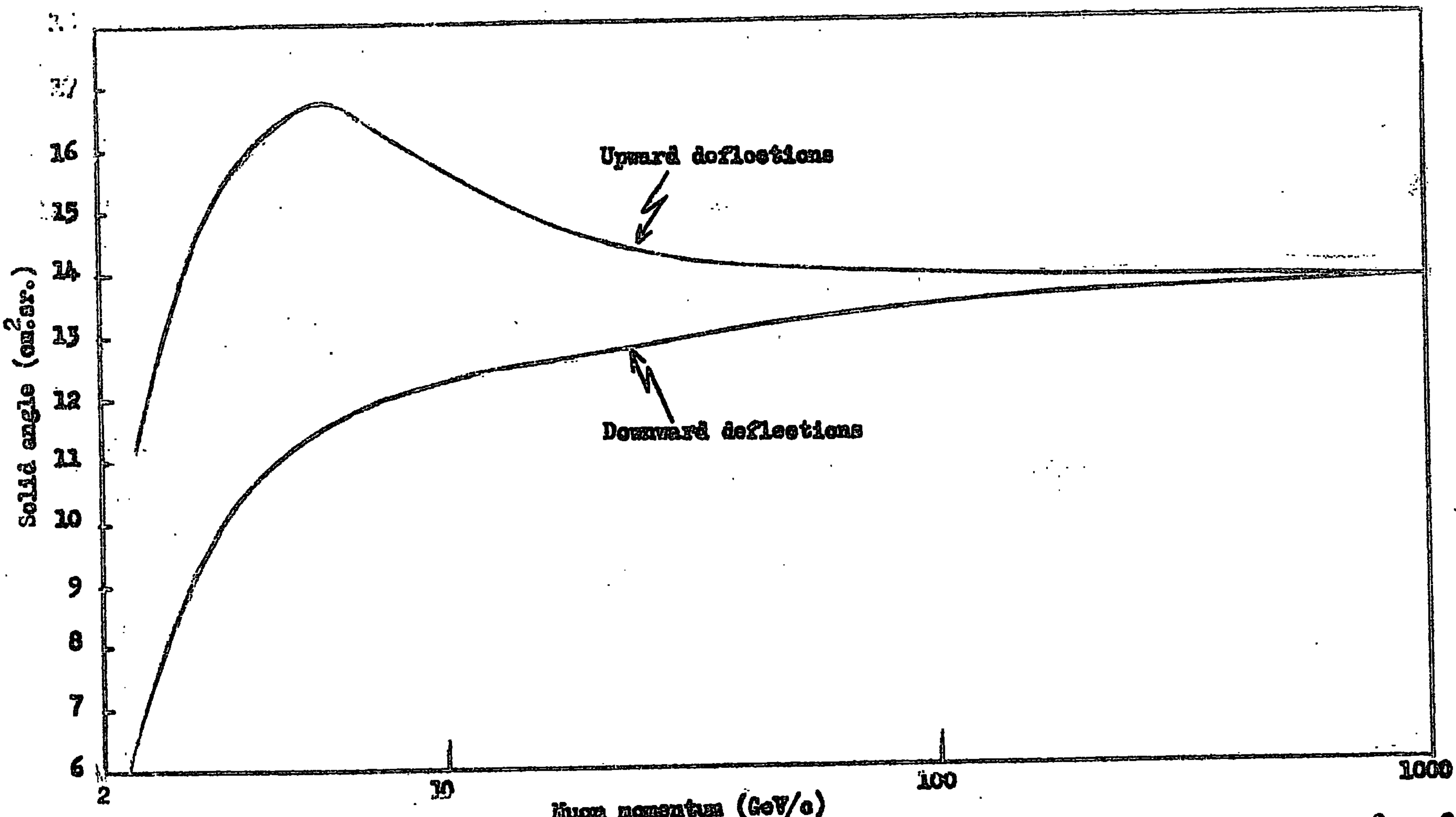

Fig. 4.13 The acceptance function, $A_c(p,\theta)$, for the spectrograph over the zenith angular range 85°-87.5°

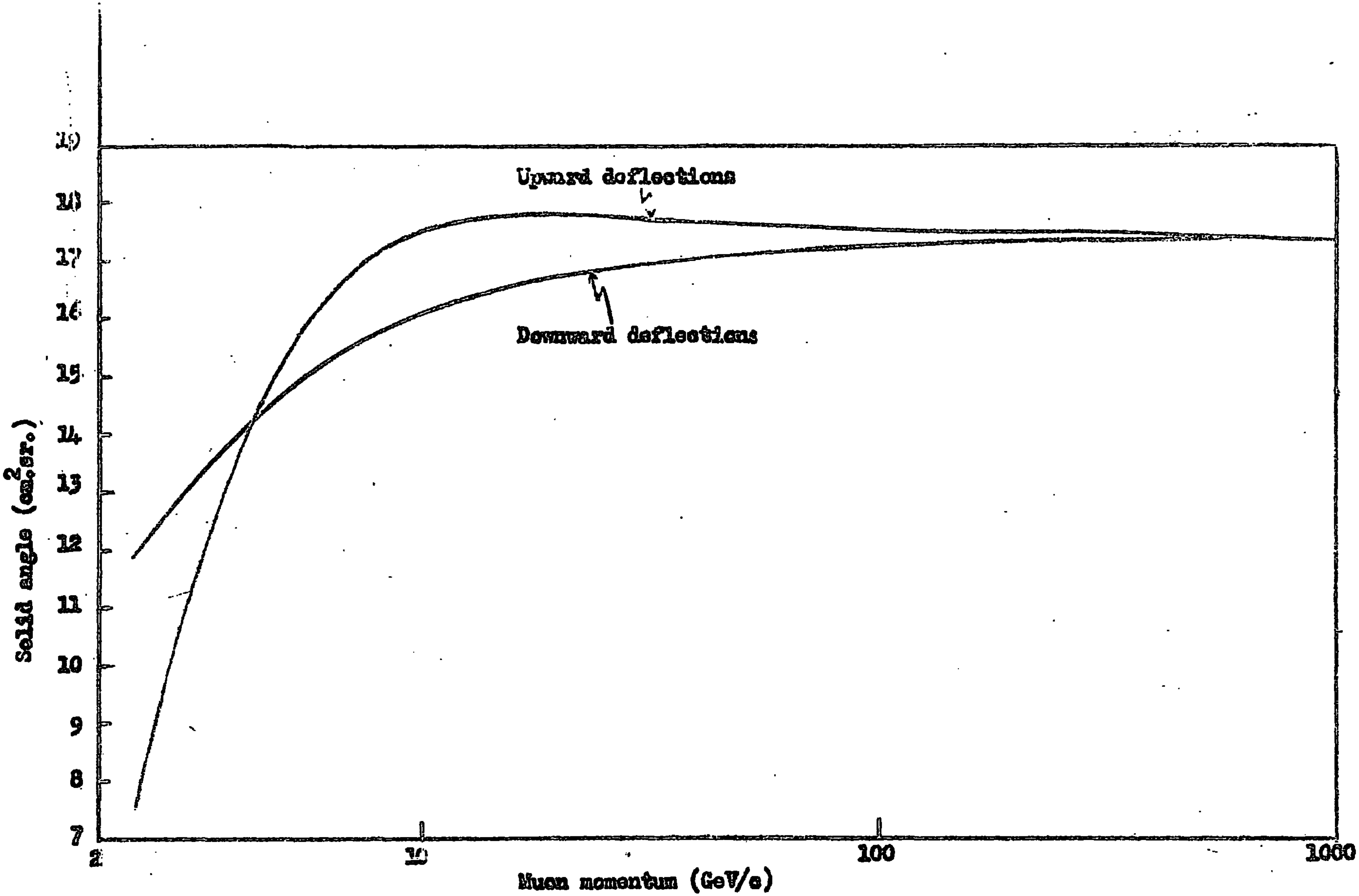

Fig. 4.14. The acceptance function, $A_o(p,\theta)$, for the spectrograph over the zenith angular range 87.5°–90°.

a function of momentum for each value of θ. Five values of θ were selected, namely 78.75°, 81.25°, 83.75°, 86.25°, and 87.75° with $\delta\theta = \pm 1.25^\circ$ so that the acceptance was found over the zenith angular range 77.5° to 90° at intervals of 2.5°. The area under these curves was plotted against angular deflection for each range of zenith angle and hence the acceptance function, $A_o(p,\theta)$, was obtained. The acceptance functions are shown in figures 4.10-4.14 where they are plotted against incident sea-level momentum.

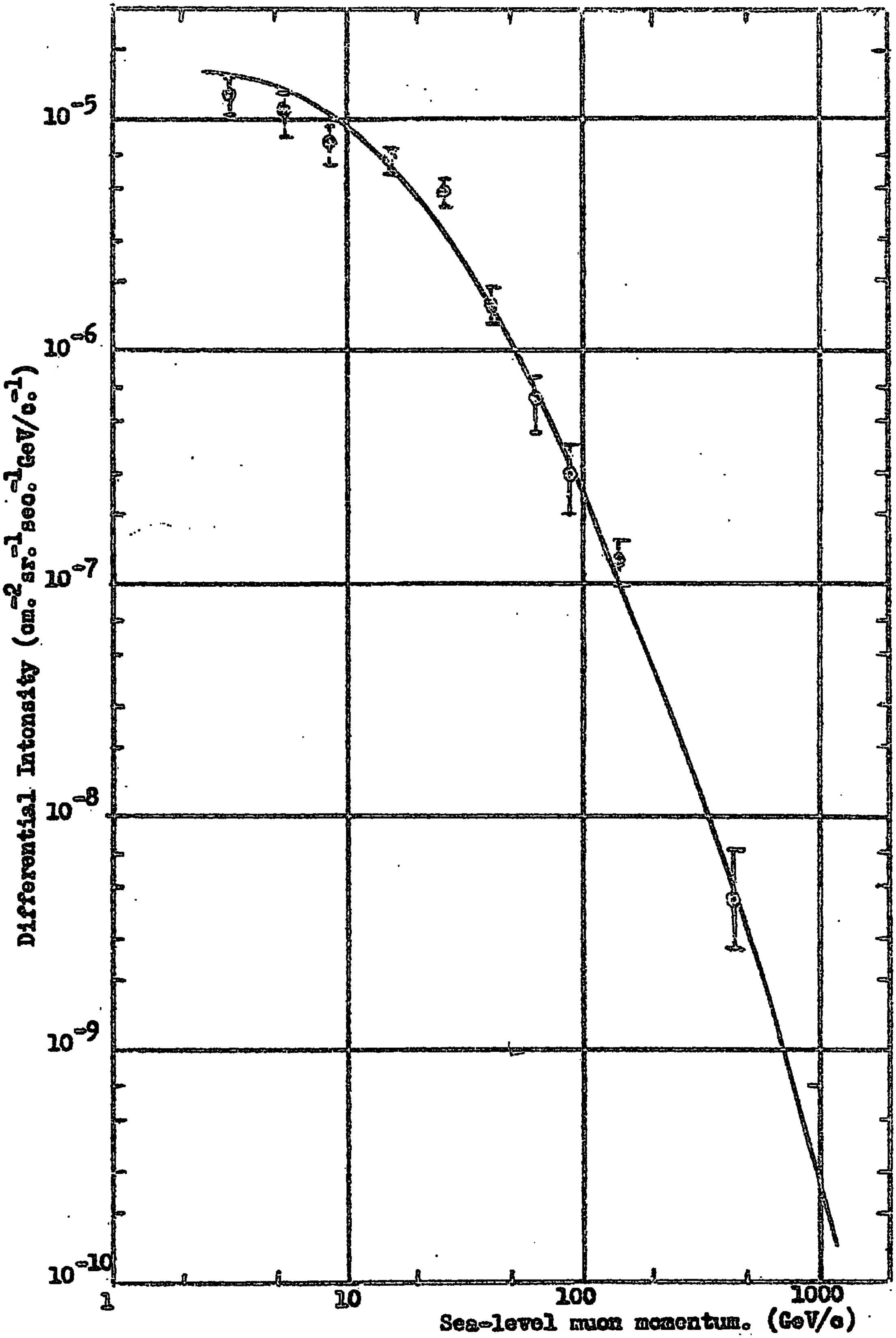

Fig. 5.1 The measured muon momentum spectrum in the zenith angular range 77.5°-80°. (Also shown is the theoretical spectrum.)

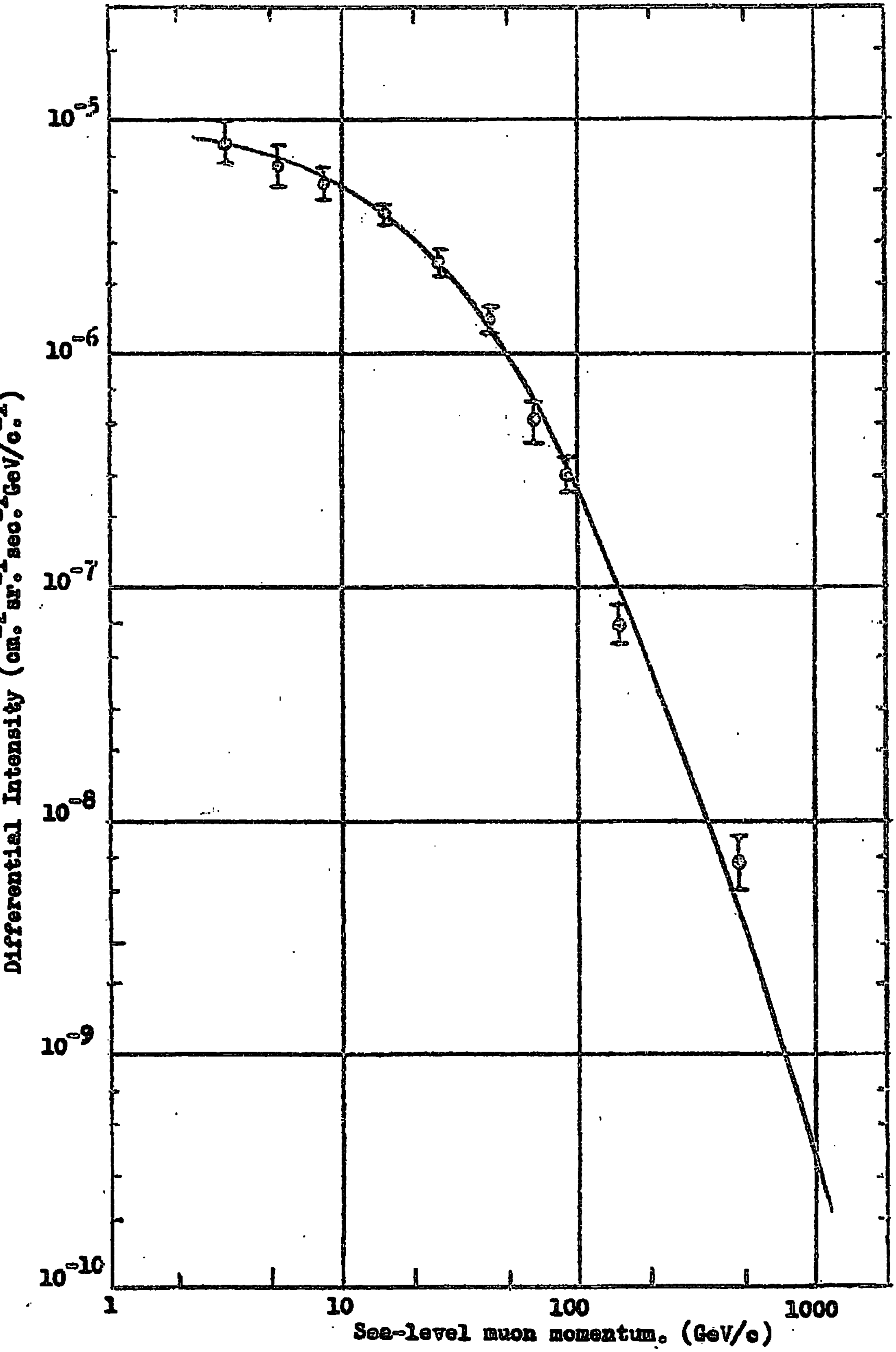

Fig. 5.2 The measured muon momentum spectrum in the zenith angular range 80°-82.5°. (Also shown is the theoretical spectrum.)

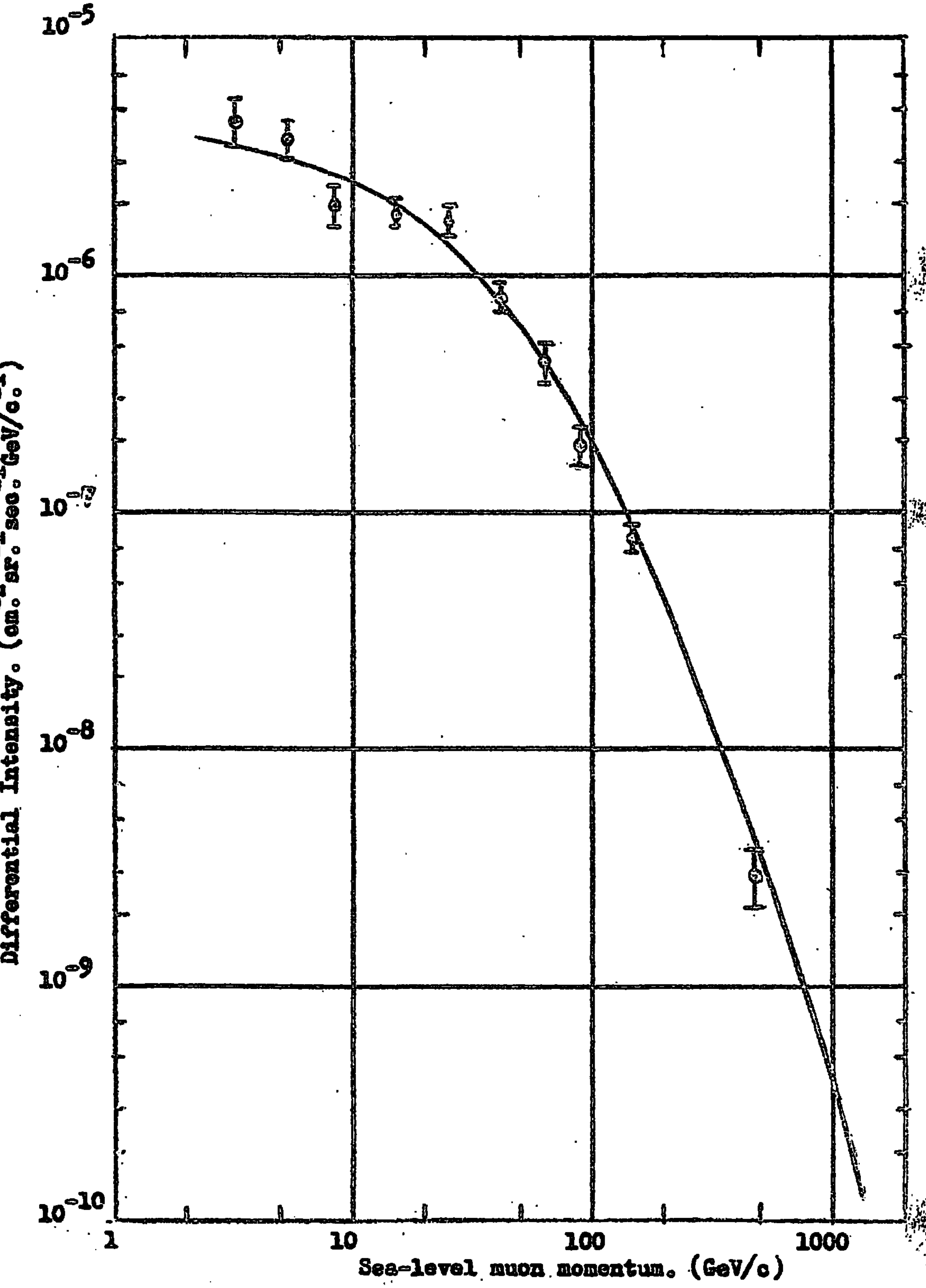

Fig. 5.3 The measured muon momentum spectrum in the zenith angular range 82.5°-85°. (Also shown is the theoretical spectrum.)

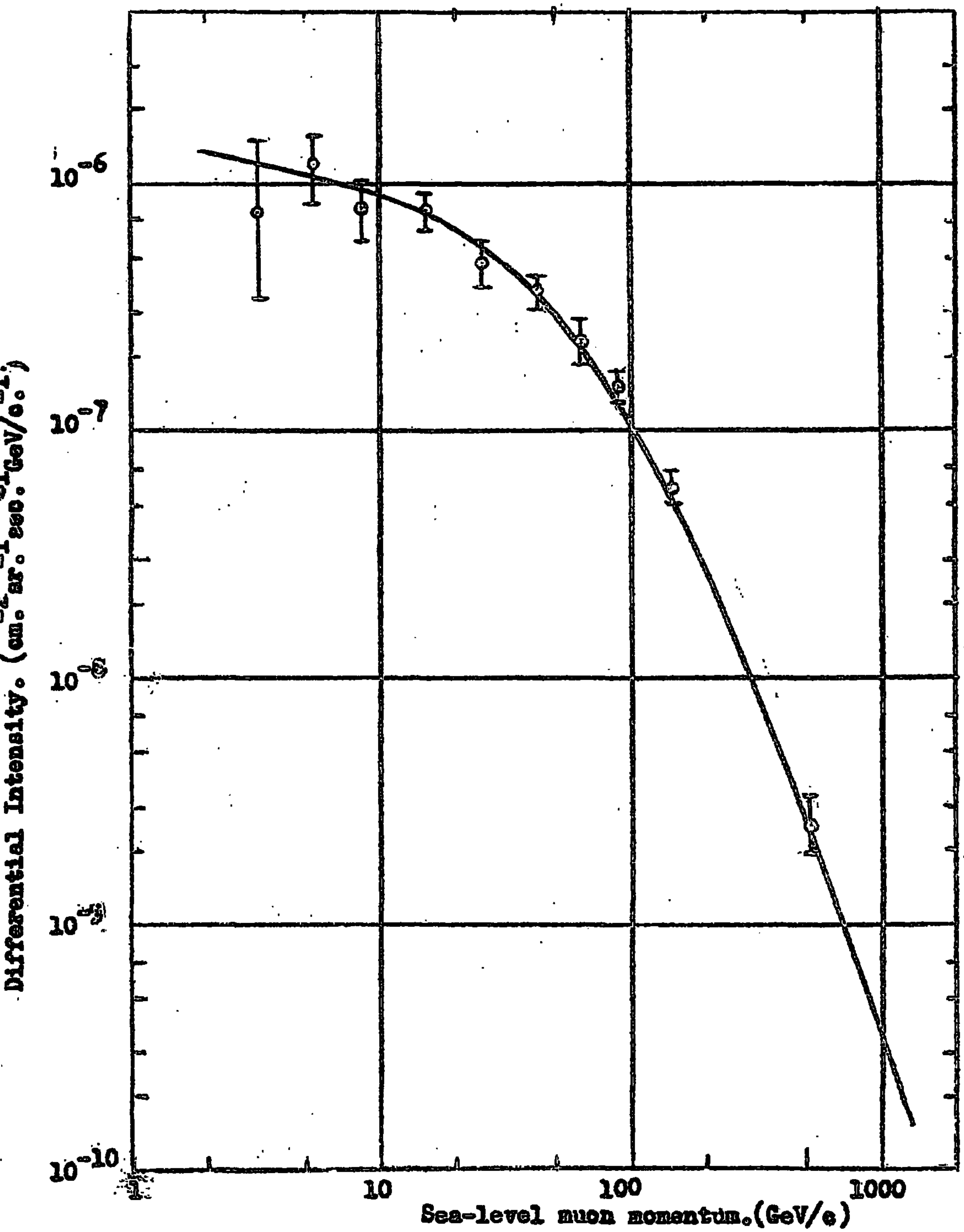

Fig. 5.4 The measured muon momentum spectrum in the zenith angular range 85°–87.5°. (Also shown is the theoretical spectrum.)

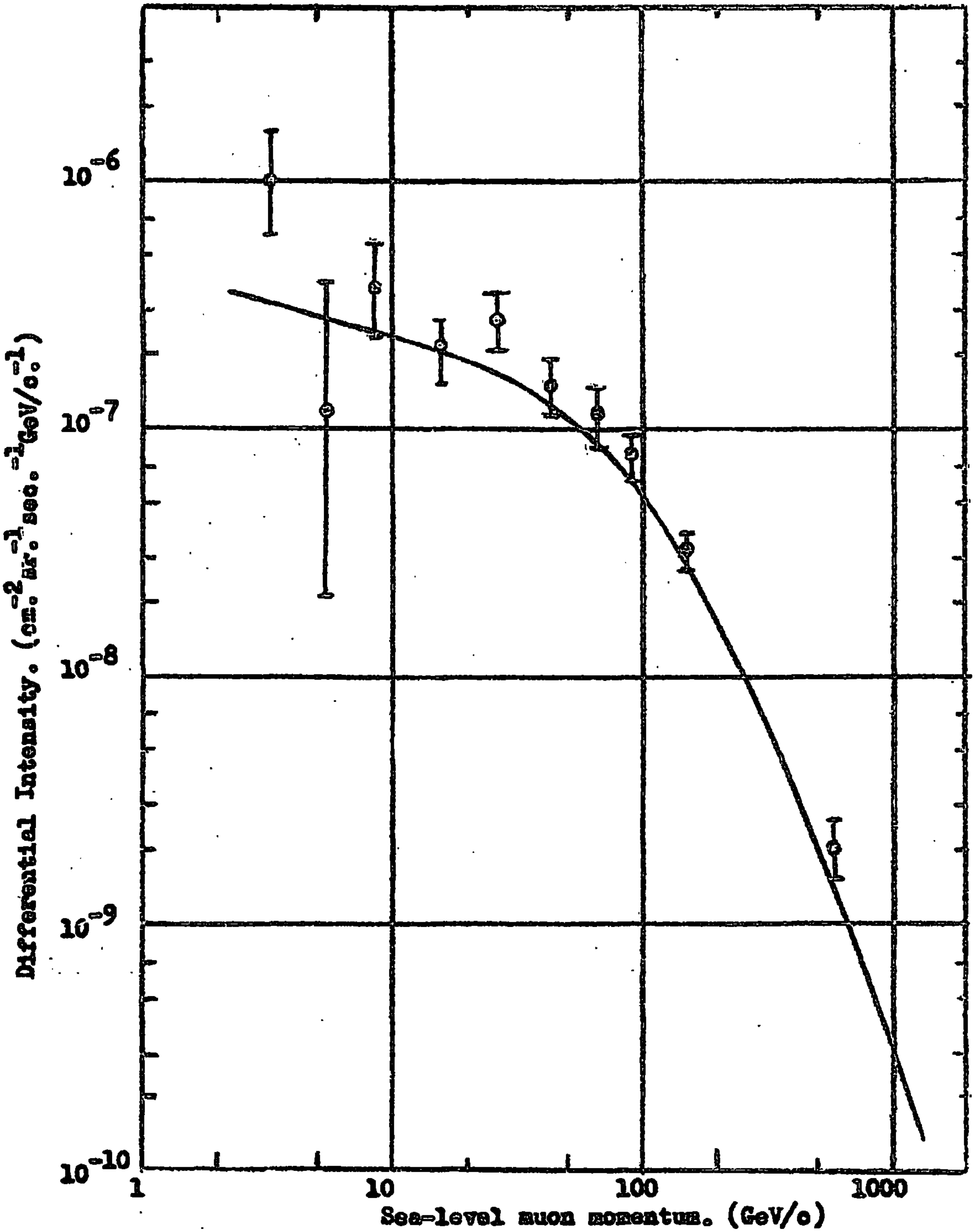

Fig. 5.5 The measured muon momentum spectrum in the zenith angular range 87.5°-90°. (Also shown is the theoretical spectrum.)

Chapter V

THE MEASURED MOMENTUM SPECTRA OF SEA-LEVEL MUONS AT LARGE ZENITH ANGLES

5.1 The expected rate of events

As mentioned earlier (§4.4) the expected rate of events for a particular interval of momentum and angular range is the integral of the product of the acceptance function, $A_o(p,\theta).\eta.G$, and the predicted intensity $N(p,\theta)dp$. Comparison of the expected rate and the observed rate of events gives the measured momentum spectra.

The measured momentum spectra for intervals of 2.5^o over the zenith anglular range 77.5^o-90^o are shown in figures 5.1 - 5.5. The solid curves are the expected spectra assuming all muons come from pions only. For momenta below 74 GeV/c, the measured intensities refer to the normal measuring technique whilst for momenta above 74 GeV/c the measured intensities are obtained using track simulator measurements (cf. §3.4).

Corrections for "noise" i.e. the errors in determining the trajectories have been applied following the technique due to Lloyd and Wolfendale (1955). The corrections are small downward displacement of the measured intensities at high momenta.

Tables 5.1 - 5.3 show the theoretical and measured differential intensities at large zenith angles as a function of momentum.

Before interpreting these data the results on the charge ratio will be considered.

Zenith Angular Range	Momentum (GeV/c)	Theoretical Differential Intensity ($cm^{-2}st^{-1}sec^{-1}GeV/c^{-1}$)	Measured Differential Intensities ($cm^{-2}st^{-1}sec^{-1}GeV/c^{-1}$)
77.5°–80°	3.2	1.58×10^{-5}	$(1.27 \pm 0.24)10^{-5}$
	5.3	1.40×10^{-5}	$(1.09 \pm 0.24)10^{-5}$
	8.4	1.09×10^{-5}	$(7.97 \pm 1.48)10^{-6}$
	15.1	6.20×10^{-6}	$(6.72 \pm 0.83)10^{-6}$
	25.7	3.50×10^{-6}	$(4.90 \pm 0.69)10^{-6}$
	41.2	1.57×10^{-6}	$(1.61 \pm 0.29)10^{-6}$
	62.6	6.80×10^{-7}	$(6.21 \pm 1.68)10^{-7}$
	88.4	3.12×10^{-7}	$(3.02 \pm 1.01)10^{-7}$
	143	9.80×10^{-8}	$(1.28 \pm 0.28)10^{-7}$
	446	4.70×10^{-9}	$(4.54 \pm {}^{2.70}_{1.80})10^{-9}$
80°–82.5°	3.2	8.00×10^{-6}	$(8.26 \pm 1.69)10^{-6}$
	5.3	7.00×10^{-6}	$(6.37 \pm 1.25)10^{-6}$
	8.4	5.70×10^{-6}	$(5.26 \pm 0.80)10^{-6}$
	15.1	3.88×10^{-6}	$(3.88 \pm 0.42)10^{-6}$
	25.7	2.37×10^{-6}	$(2.42 \pm 0.31)10^{-6}$
	41.2	1.32×10^{-6}	$(1.37 \pm 0.18)10^{-6}$
	62.6	6.50×10^{-7}	$(5.09 \pm 1.04)10^{-7}$
	88.4	3.12×10^{-7}	$(2.99 \pm 0.53)10^{-7}$
	143	9.60×10^{-8}	$(6.77 \pm 1.27)10^{-8}$
	464	4.10×10^{-9}	$(6.50 \pm 1.55)10^{-9}$

Table 5.1 The theoretical and measured intensities of muons in the zenith angular range 77.5°-82.5°

Zenith Angular Range	Momentum (GeV/c)	Theoretical Differential Intensity ($cm^{-2} st^{-1} sec^{-1} GeV/c^{-1}$)	Measured Differential Intensities ($cm^{-2} st^{-1} sec^{-1} GeV/c^{-1}$)
82.5°-85°	3.2	3.42×10^{-6}	$(4.53 \pm 1.01)10^{-6}$
	5.3	3.00×10^{-6}	$(3.80 \pm 0.77)10^{-6}$
	8.4	2.58×10^{-6}	$(2.00 \pm 0.40)10^{-6}$
	15.1	1.95×10^{-6}	$(1.82 \pm 0.24)10^{-6}$
	25.7	1.32×10^{-6}	$(1.69 \pm 0.22)10^{-6}$
	41.2	8.10×10^{-7}	$(8.09 \pm 1.14)10^{-7}$
	62.6	4.31×10^{-7}	$(4.26 \pm 0.78)10^{-7}$
	88.4	2.31×10^{-7}	$(1.90 \pm 0.33)10^{-7}$
	143	8.80×10^{-8}	$(7.81 \pm 1.16)10^{-8}$
	468	4.00×10^{-9}	$(2.87 \pm 0.79)10^{-9}$
85°-87.5°	3.2	1.20×10^{-6}	$(7.70 \pm {}^{7.49}_{4.18})10^{-7}$
	5.3	1.07×10^{-6}	$(1.21 \pm 0.38)10^{-6}$
	8.4	9.40×10^{-7}	$(7.98 \pm 2.22)10^{-7}$
	15.1	7.60×10^{-7}	$(7.83 \pm 1.38)10^{-7}$
	25.7	5.70×10^{-7}	$(4.82 \pm 1.07)10^{-7}$
	41.2	3.68×10^{-7}	$(3.61 \pm 0.59)10^{-7}$
	62.6	2.16×10^{-7}	$(2.29 \pm 0.51)10^{-7}$
	88.4	1.29×10^{-8}	$(1.50 \pm 0.25)10^{-7}$
	143	5.40×10^{-8}	$(5.86 \pm 0.87)10^{-8}$
	518	2.55×10^{-9}	$(2.59 \pm 0.70)10^{-9}$

Table 5.2 The theoretical and measured intensities of muons in the zenith angular range 82.5°-87.5°

Zenith Angular Range	Momentum (GeV/c)	Theoretical Differential Intensity ($cm^{-2}st^{-1}sec^{-1}GeV/c^{-1}$)	Measured Differential Intensities ($cm^{-2}st^{-1}sec^{-1}GeV/c^{-1}$)
87.5°-90°	3.2	3.20×10^{-7}	$(9.96 {+5.89 \atop -3.95})10^{-7}$
	5.3	2.70×10^{-7}	$(1.16 {+2.66 \atop -0.96})10^{-7}$
	8.4	2.41×10^{-7}	$(3.67 {+1.96 \atop -1.34})10^{-7}$
	15.1	2.03×10^{-7}	$(2.13 \pm 0.64)10^{-7}$
	25.7	1.67×10^{-7}	$(2.79 \pm 0.72)10^{-7}$
	41.2	1.28×10^{-7}	$(1.50 \pm 0.39)10^{-7}$
	62.6	9.30×10^{-8}	$(1.16 \pm 0.33)10^{-7}$
	88.4	6.50×10^{-8}	$(7.81 \pm 1.69)10^{-8}$
	143	2.93×10^{-8}	$(3.27 \pm 0.59)10^{-8}$
	561	1.58×10^{-9}	$(2.06 \pm 0.56)10^{-9}$

Table 5.3 The theoretical and measured intensites of muons in the zenith anglular range 87.5°-90°

5.2 The charge-ratio of muons

The charge ratio, K, of the number of positive muons, $N(\mu^+)$, to the number of negative muons, $N(\mu^-)$ is defined simply by

$$K = \frac{N(\mu^+)}{N(\mu^-)}$$

whereas the positive excess is $N(\mu^+) - N(\mu^-)$ and the relative positive excess, η, is defined by

$$\eta = \frac{N(\mu^+) - N(\mu^-)}{N(\mu^+) + N(\mu^-)} = \frac{K-1}{K+1}$$

An excess of positive muons is to be expected when one remembers that the primary radiation is almost entirely positively charged. If a proton suffers a catastrophic collision such that it undergoes charge exchange (and emerges as a neutron) and if x pions are created, then $\frac{1}{2}(x + 1)$ will be positively charged and $\frac{1}{2}(x - 1)$ will be negatively charged, where x is odd in order that the charge conservation law should be obeyed. As the probabilities of π-μ decay and pion interaction are independent of the sign of the charge, the positive excess of pions results in an excess of positive muons. The pion multiplicity at production is therefore reflected in the sea-level positive excess for muons, and a study of the positive excess at high energies gives information on the variation of multiplicity with energy (e.g. if the multiplicity increased with primary energy the charge ratio would decrease with increasing energy, whereas it would remain constant for a constant multiplicity).

The data from the present experiment have been combined and the measured ratios have been determined as a function of muon energy at

Energy Range at production GeV	Field A		Field B		Positive-Negative Ratio
	$N(\mu+)$	$N(\mu^-)$	$N(\mu+)$	$N(\mu^-)$	
10 - 20	3	67	96	1	1.46 ± 0.23
20 - 30	33	95	84	24	0.99 ± 0.13
30 - 40	43	44	67	40	1.31 ± 0.19
40 - 55	45	62	64	54	0.94 ± 0.13
55 - 75	46	41	54	36	1.30 ± 0.20
75 - 100	31	30	51	31	1.34 ± 0.23
100 - 150	28	23	40	16	1.74 ± 0.35
150 - 200	15	11	13	11	1.27 ± 0.36

Table 5.4 The Positive-Negative Ratio as a Function of Muon Energy at Production

(A and B refer to opposite field directions)

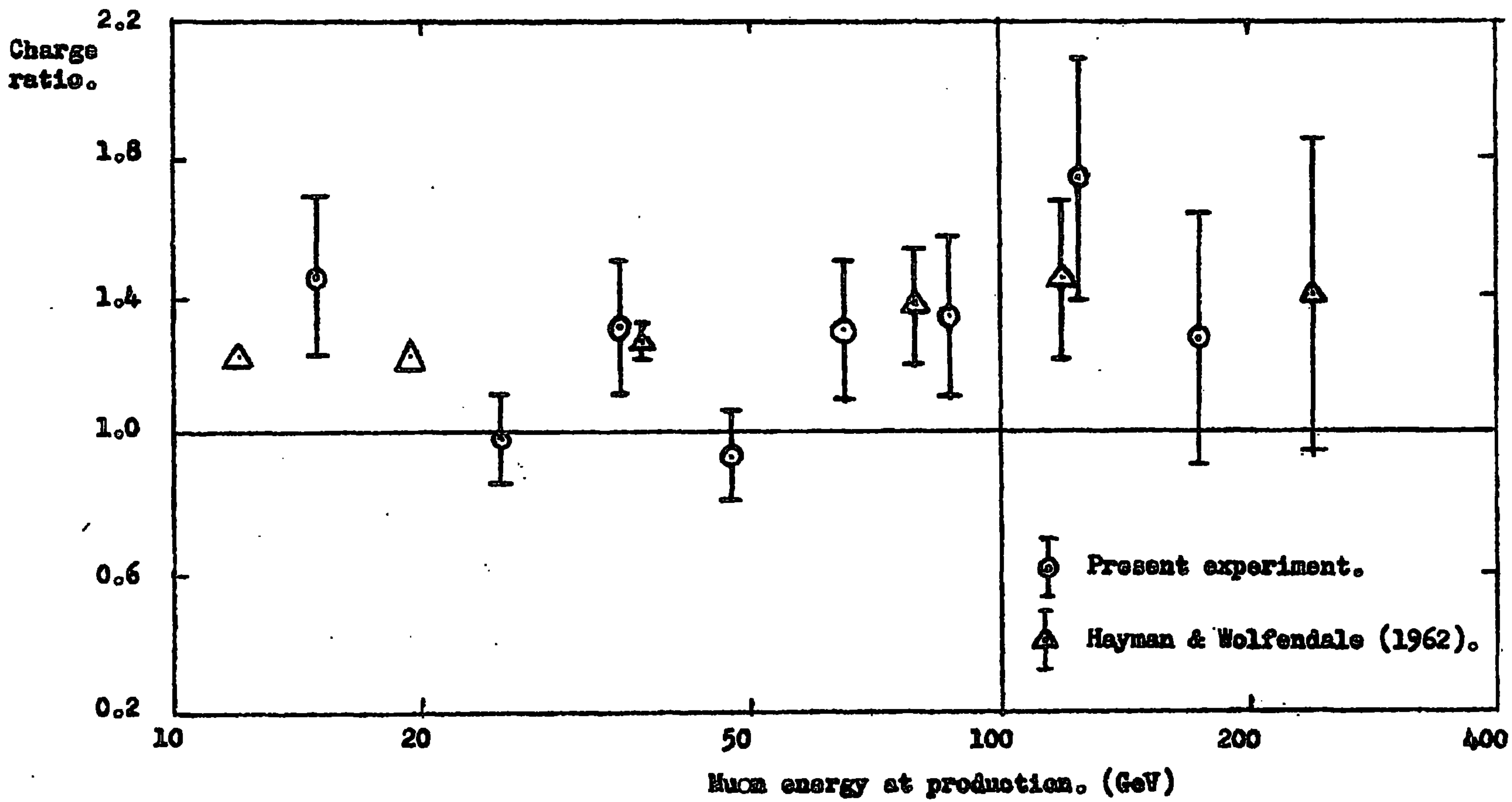

Fig. 5.6 The positive-negative ratio as a function of muon energy at production.

production (i.e. the sea level energies have been converted to energies at production). The data are given in Table 5.4, and the ratios are plotted in figure 5.6. Also shown in figure 5.6 are the recent results of Hayman and Wolfendale (1962); these measurements were made with the Vertical Spectrograph at Durham, and the measured energies have also been converted to energy at production.

In the present work, the effects of instrumental bias were reduced by defining the charge ratio K by

$$K^2 = \left[\frac{N(\mu^+)}{N(\mu^-)}\right]_A \left[\frac{N(\mu^+)}{N(\mu^-)}\right]_B$$

where A and B refer to opposite field directions.

Although the statistical accuracy of the present data is low, the results are of importance in that they confirm the conclusion of Hayman and Wolfendale that the charge ratio does not tend to unity, at least before several hundred GeV. This fact was interpreted by these authors as showing that the fluctuations in the multiplicity of high energy pions increases with increasing energy.

5.3 Interpretation of the momentum spectra

5.3(i) Statement of the problem

The basic problem is to derive information about the characteristics of high energy nuclear interactions from the measurements on sea level muon spectra. Of the characteristics accessible to study, the most significant is the relative production of particles in high energy collisions which give rise eventually to muons. As mentioned earlier (§4.1) the most convenient approach is to take the measured vertical spectrum as the starting point and from it calculate the production spectra of the parent particles for different assumed masses of these particles. The production spectra are then used to predict the sea-level spectra at large zenith angles and, by comparison with the observed spectrum, conclusions can be drawn about the most likely parent particle (or combination of particles).

Prior to the present work it was not clear that the inclined muon spectrum was, in fact, sensitive to the mass of the parent particle. The early work of Jakeman (1956) showed that a large sensitivity existed but the values taken for the masses and lifetimes of the relevant particles were, at that time, necessarily imprecise. Pak et al (1961) implied a sensitivity, but quantitative estimates were not given. The theoretical studies of Allen and Apostolakis (1961), however, showed that the inclined spectrum should be comparatively insensitive to the mass of the parent particle. The present work shows that there is, in fact, considerable sensitivity (see, for example, figures 4.8 and 4.9).

5.3 (ii) Determination of the K/π ratio from the measurements of inclined spectra

The spectra (figures 5.1 - 5.5) in the zenith angular range 77.5°-80° have been converted to spectra at production, and the data combined to give the ratios of muon intensities at production. These ratios are shown in figure 5.7. Also shown on this figure are the ratios expected on the basis of 100% pions or 100% $K_{\mu 2}$-mesons as parents, together with the ratio expected on the basis of 100% K-mesons after the treatment of Osborne (cf. §4.3). In addition, the experimental points corrected for the effect of decay spread after the treatment of Osborne are also shown.

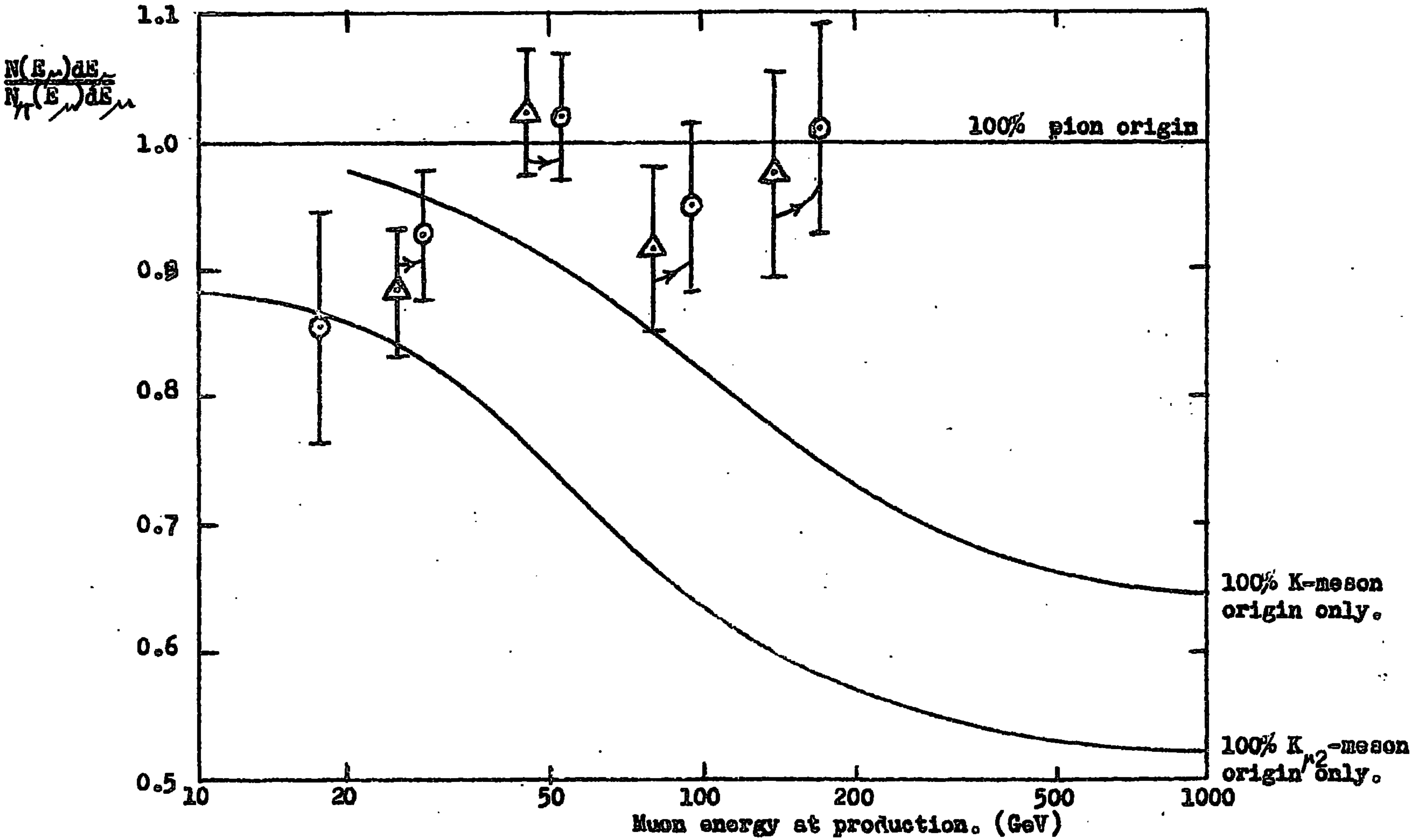

Fig. 5.7 The ratio of the muon production spectra for the present experiment.
(The circular points should be compared with the curve for $K_{\mu2}$-meson origin, and the triangular points, which are displaced, with the curve for K-meson origin. The points at 565 GeV are not shown, (cf. Table 5.5).)

Muon Production Energy. (GeV)	$\dfrac{N_{obs}(E_\mu)dE_\mu}{N_\pi(E_\mu)dE_\mu}$ ($K_{\mu 2}$)	$\dfrac{N_{obs}(E_\mu)dE_\mu}{N_\pi(E_\mu)dE_\mu}$ (K)
17.5	0.855 ± 0.090	
28.2	0.926 ±0.050	0.882 ±0.049
52.9	1.019 ±0.048	1.022 ±0.049
95.2	0.948 ±0.066	0.915 ±0.065
171	1.009 ±0.082	0.973 ±0.081
565	1.405 ±0.173	1.426 ±0.179

Table 5.5 The measured ratios of muon intensities at production, for $K_{\mu 2}$ decay mode only, and all K-meson decay modes (a correction for decay spraead is included).

The experimental values are given in table 5.5. At the lowest energy a further acceptance function correction has been applied. This is necessary to account for the particles lost by virtue of there being insufficient track length near the top of flash tube tray A or near the bottom of D for such tracks to be accepted during measurement. It is not though that the point plotted at 17.5 GeV will in fact be accurate, as it is in this region that large corrections are made for the effects of scattering in the atmosphere, energy loss in the magnet etc.

It is possible, by interpolation, to make an estimate of the fraction, $F_{K_{\mu 2}}$, of $K_{\mu 2}$-mesons or fraction, F_K, of all K-mesons giving rise to muons, required to give aggeement with experiment.

Thus, $$F_{K_{\mu 2}} = \frac{N(K_{\mu 2})}{N(\pi) + N(K_{\mu 2})}$$

and it can easily be shown that

$$F_{K_{\mu 2}} = \frac{1-R}{1-P_{K_{\mu 2}}}$$

where R is the observed ratio plotted in figure 5.7, and $P_{K_{\mu 2}}$ is the ratio expected for 100% $K_{\mu 2}$ production of muons only. The error in $F_{K_{\mu 2}}$ is given by $\delta F_{K_{\mu 2}} = \dfrac{\delta R}{1-P_{K_{\mu 2}}}$. Similar expressions exist for the case when all K-meson muon-producing modes are considered.

The fractions $F_{K_{\mu 2}}$, F_K for the present work are summarized in table 5.6. Discussion of the work at zenith angles 80° and 65°-85° is deferred until chapter 6. The fraction, F_K, for the present experiment is shown in figure 5.8, together with the approximate best curve through the experimental points, and the approximate 16% upper limit to F_K (i.e. one standard deviation).

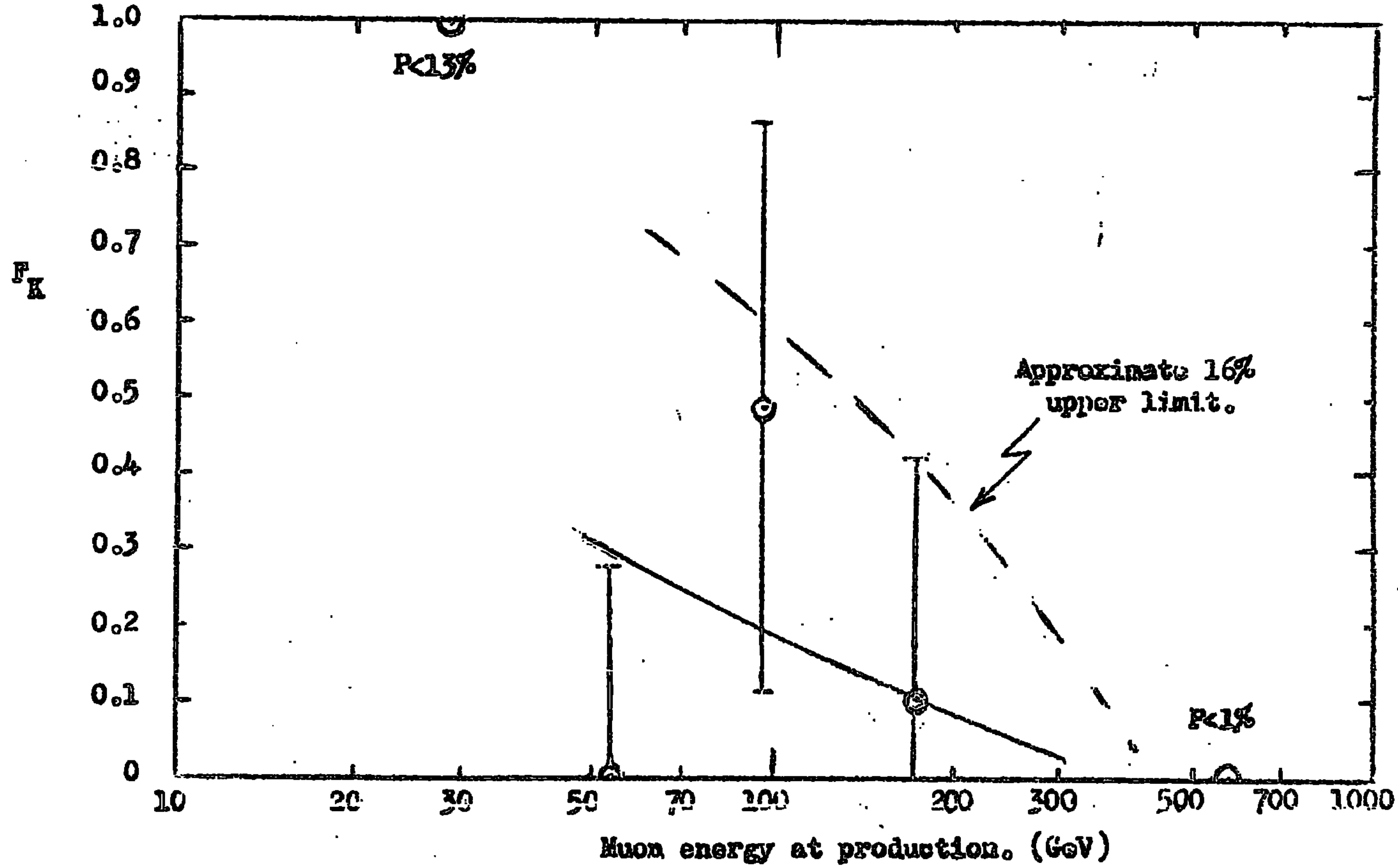

Fig. 5.8 The fraction, F_K, of all K-mesons giving rise to muons for the present experiment.

Experiment	Muon Energy (GeV)	$F_{K_{\mu 2}}$	F_K
Durham, 80°	36	0.25 ± 0.23	
	44	0.22 ± 0.20	
Durham 77.5°-90°	17.5	>0.410	
	28.2	0.433 ± 0.292	$P<13.4\%$ for $F_K<1$
	52.9	<0.111	<0.281
	95.2	$0.145 {+0.184 \atop -0.145}$	0.491 ± 0.376
	171	<0.173	$0.106 {+0.319 \atop -0.106}$
	565	$P<1\%$ for $F_{K_{\mu 2}}>0$	$P<1\%$ for $F_K>0$
Durham (Emulsion) 65°-85°	28	<0.23	
	55	<0.72	
	108	<0.28	

Table 5.6 $F_{K_{\mu 2}}$ (F_K) as a function of muon energy at production.

It can be shown that the ratio, (K/π), of the production of all charged K-mesons to charged pions is given as follows:

$$(K/\pi) = \frac{1 - N_m/N_\pi}{N_m/N_\pi - R} \cdot \frac{F_K}{F_\pi}$$

where N_m/N_π is the measured ratio

R is the theoretical ratio

and F_K, F_π are the charged K-meson and pion production spectra respectively.

The results of the analysis of the K/π ratio from the present data are summarized in table 5.7. Also shown in this table are the K/π ratios derived from other work. The discussion of the K/π ratios is deferred until the next chapter.

Experimental Source	Muon Energy (GeV)	K/π Ratio
Accelerator	0.21-1.4	$\lesssim 0.10$
Polarization	3	0.54 ± 0.31
65°-85°	14.2	$0.65 {+18.74 \atop -0.65}$
80°	18	< 0.85
80°	21	$0.28 {+\infty \atop -0.28}$
65°-85°	28	< 0.32
80°	36	$0.38 {+0.52 \atop -0.32}$
80°	44	$0.31 {+0.39 \atop -0.26}$
77.5° - 90°	52.9	< 0.42
65° -85°	55	$0.42 {+2.36 \atop -0.42}$
77.5° - 90°	95.2	$0.97 {+5.53 \atop -0.84}$
65° -85°	108	< 0.45
77.5° - 90°	171	$0.09 {+0.50 \atop -0.09}$
77.5° - 90°	565	Probability <1% for K/π > 0
Jets	300-7000	< 0.40

Table 5.7 K/π ratios for muon energies < 7000 GeV.
(The large zenith angle results refer to the following:
65°-85° Allen and Apostolakis (1961)
80° Ashton and Wolfendale (1963)
77.5°-90° Present work).

Chapter VI

COMPARISON WITH THE RESULTS OF OTHER WORKERS AND CONCLUSIONS

6.1 Sea-level spectra at angles greater than 65° to the zenith

Before the addition of the neon flash tubes the present instrument was used (Ashton and Wolfendale, 1963) as a geiger counter spectrograph to measure the momentum spectrum of sea-level muons at 80° to the zenith over the momentum range 1.5 to 40 GeV/c, with the axis of the apparatus pointing in a direction $55^{\circ}36'$ east of magnetic north. The results of this experiment are shown in figure 6.1 and a discussion of their significance is given later.

Using nuclear emulsion in the air gap of a permanent magnet Allen and Apostolakis (1961) measured the absolute cosmic ray intensity in the momentum range 1 to 100 GeV/c at angles between 65° and 85° to the zenith. They determined a pion production spectrum from the vertical sea-level muon spectrum of Ashton et al (1960) using equation 4.2. With this spectrum and the appropriate values of x/p, energy loss, survival probability and the various corrections applied in §4.2 they computed sea-level muon spectra for a range of zenith angles. However, a more accurate measurement of the vertical sea-level muon spectrum has since been made by Hayman and Wolfendale (1962) and, as a consequence, the theoretical predictions due to Allen and Apostolakis are inaccurate and in disagreement with the predictions presented in chapter 4. Consideration of the experimental data of Allen and Apostolakis is deferred until the next section.

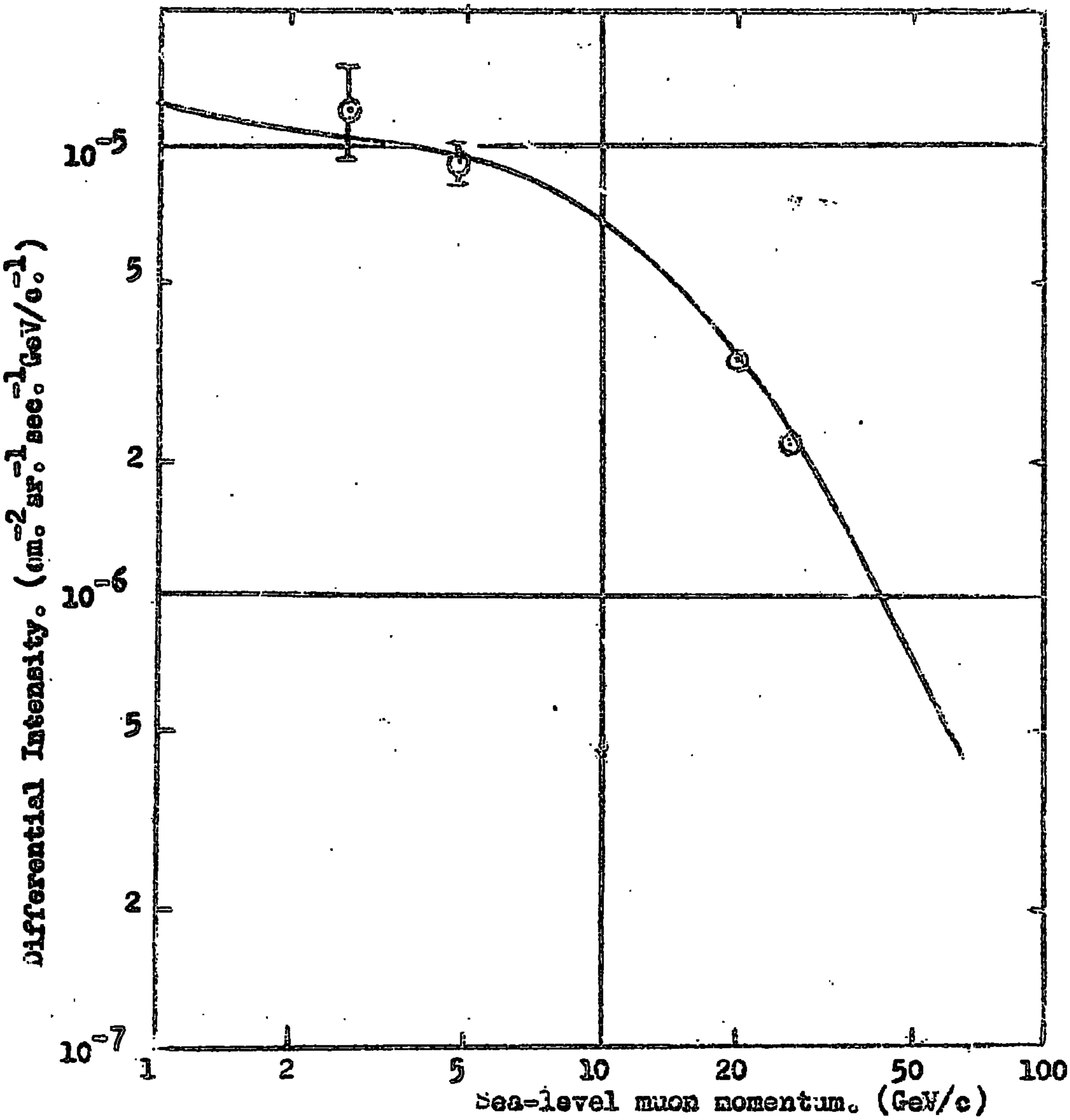

Fig. 6.1 The measured sea-level intensity spectrum at 80° to the zenith. (Ashton and Wolfendale, 1963.)

Pak et al (1961) have tilted the Cornell spectrograph and have measured the differential spectrum at 68^{o} to the zenith. Their measurements are compared with the present calculations in figure 6.2, where it is seen that there is good agreement.

Sheldon and Duller (1962) have measured the intensity of muons at various depths underground in inclined directions and these workers have derived an integral energy spectrum at 69^{o} with the aid of therange-energy relation given by Barrett et al (1952). Their integral spectrum is given in figure 6.3. Also shown in figure 6.3 is the theoretical integral spectrum from the present work. There is seen to be a significant difference between the two spectra. Sheldon and Duller find good agreement between their spectrum and the spectrum measured by Pak et al, but this is after the latters' spectrum has been integrated and normalised to the intensity found by Sheldon and Duller at 68 GeV. Since the original spectrum of Pak et al was absolute this normalization procedure is considered by the present author to be invalid.

More recently, Smith and Duller (private communication, 1962) have used the apparatus of Sheldon and Duller at larger zenith angles underground and have derived the integral energy spectra shown in figure 6.4. Some of these measured intensities are compared in figure 6.5 with the theoretical integral spectra (and the measured intensities) found in the present work. There is again a systematic difference in the results, the intensities found in the underground measurements being higher than

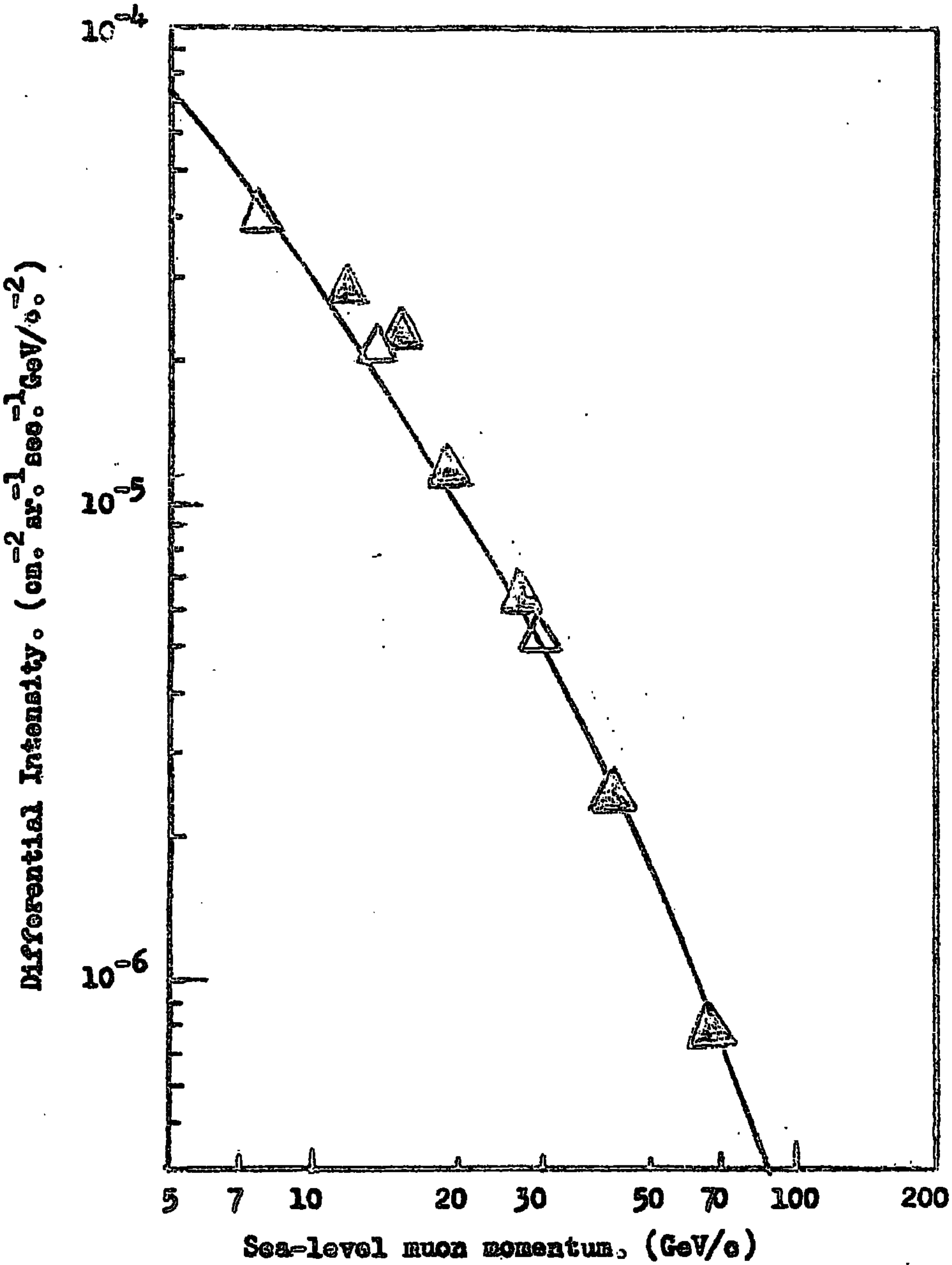

Fig. 6.2 Comparison of the theoretical spectrum at 68° to the zenith from the present work, and the measured intensities of Pak et al (1961).

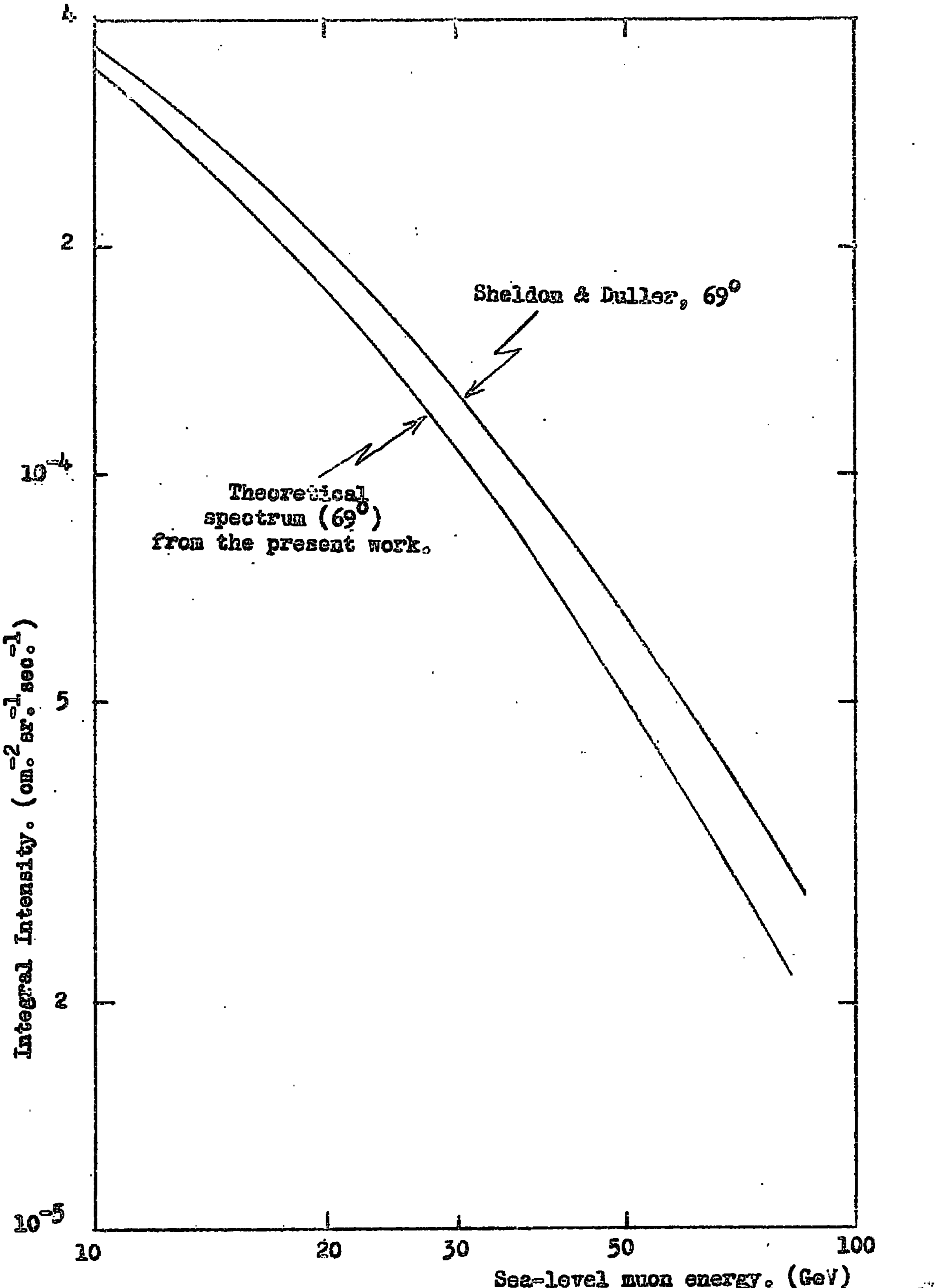

Fig. 6.3 The measured (Sheldon & Duller, 1962) and predicted intensities (present work) at 69° to the zenith.

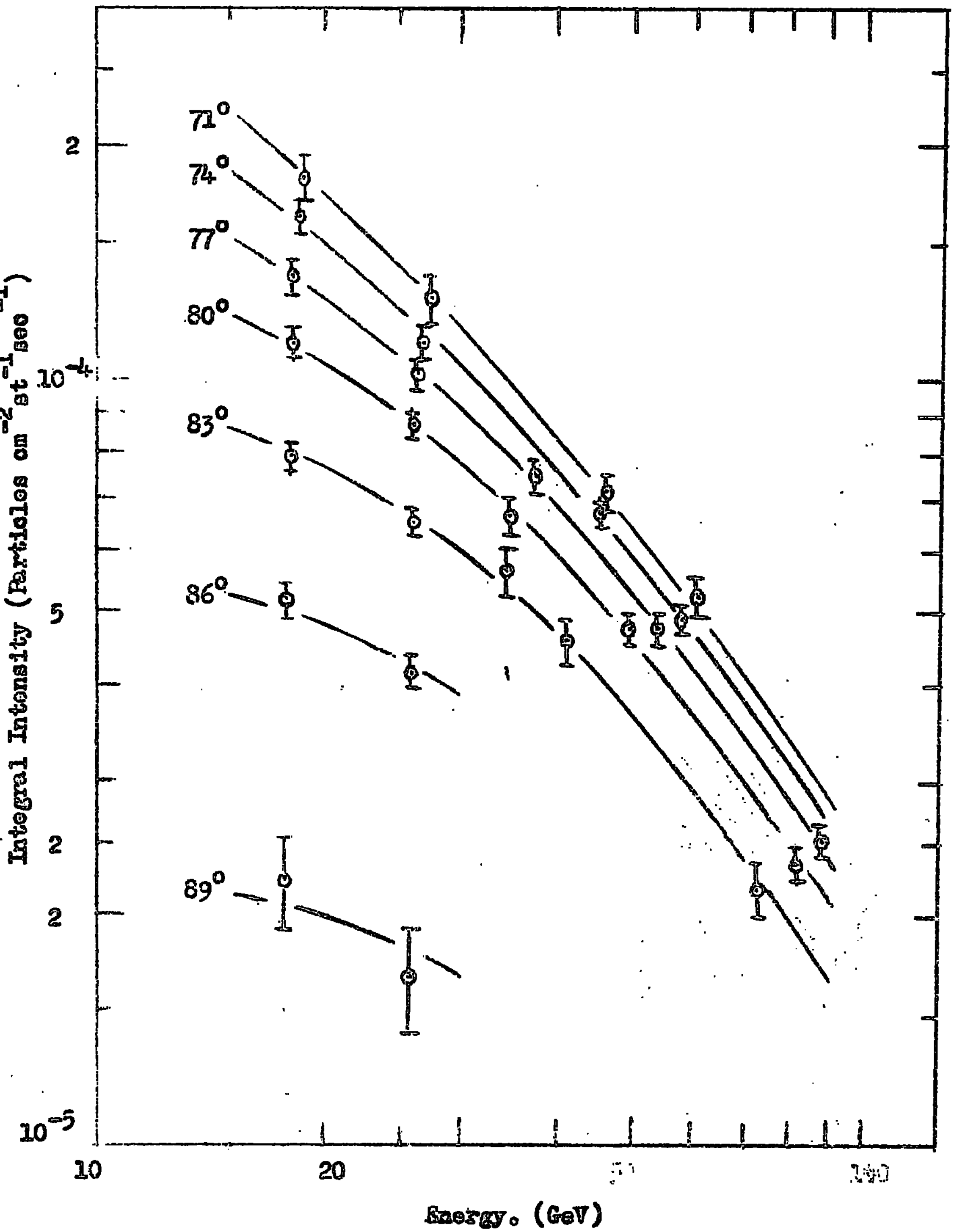

Fig. 6.4 The inferred sea-level integral energy spectra at large zenith angles. (Smith and Duller, 1962.)

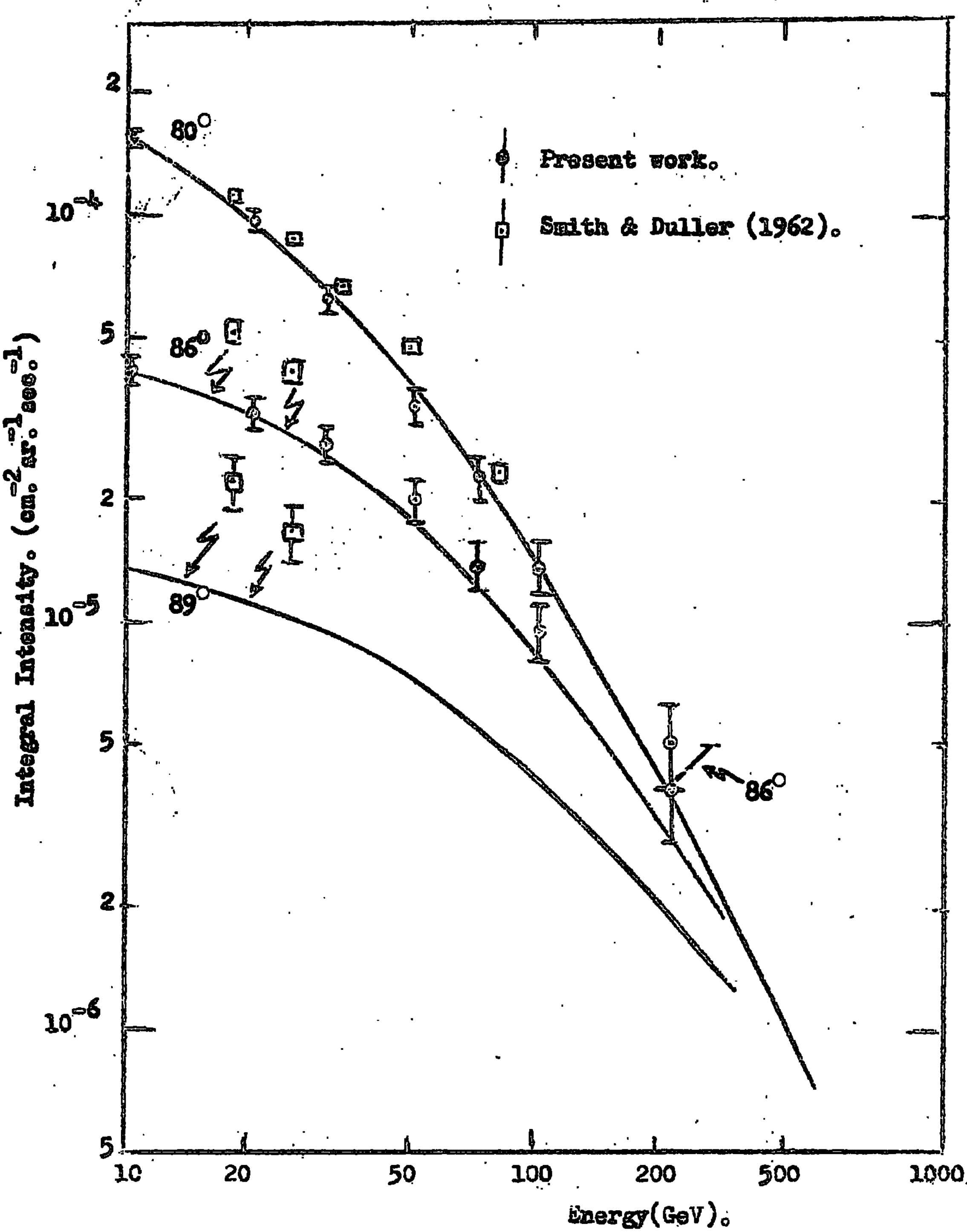

Fig. 6.5 Comparison of the measured sea-level muon integral intensities from the present work, and those from the underground experiment of Smith and Duller (1962). (The solid curves are those expected from the present work.)

predicted, and measured, in the present work. The fact that the difference between the intensities found in the two experiments increases as the zenith angle increases would appear to preclude an error in the acceptance (i.e. solid angle x area) of the underground telescope. The most likely explanation for the difference is that there is an increasing enhancement of the underground intensites through scattering in the rock as the zenith angle increases.

Other work (e.g. Coates and Nash, 1962) has shown that the simple propagation model used in the present analysis, and exemplified by equation 4.2, is valid for zenith angles less than 65°. The conclusion that can be drawn, therefore, is that this model is valid for all angles between 0° and 90°.

6.2 The K/π ratio

From the point of view of comparison of the results of various experiments on the derivation of the K/π ratio it is easiest to compare the ratios calculated under the assumption that only the $K_{\mu 2}$ mode is effective in producing muons.

Ashton and Wolfendale (1963) have measured the muon spectrum at 80° to the zenith and the ratios of the muon intensities are shown in figure 6.6. The values of $F_{K_{\mu 2}}$ derived by the authors are shown in figure 6.7.

Allen and Apostolakis (1961) did not analyse their results with respect to the determination of $F_{K_{\mu 2}}$, but this analysis has been carried out here. The data for the zenith angular range 65°–85°

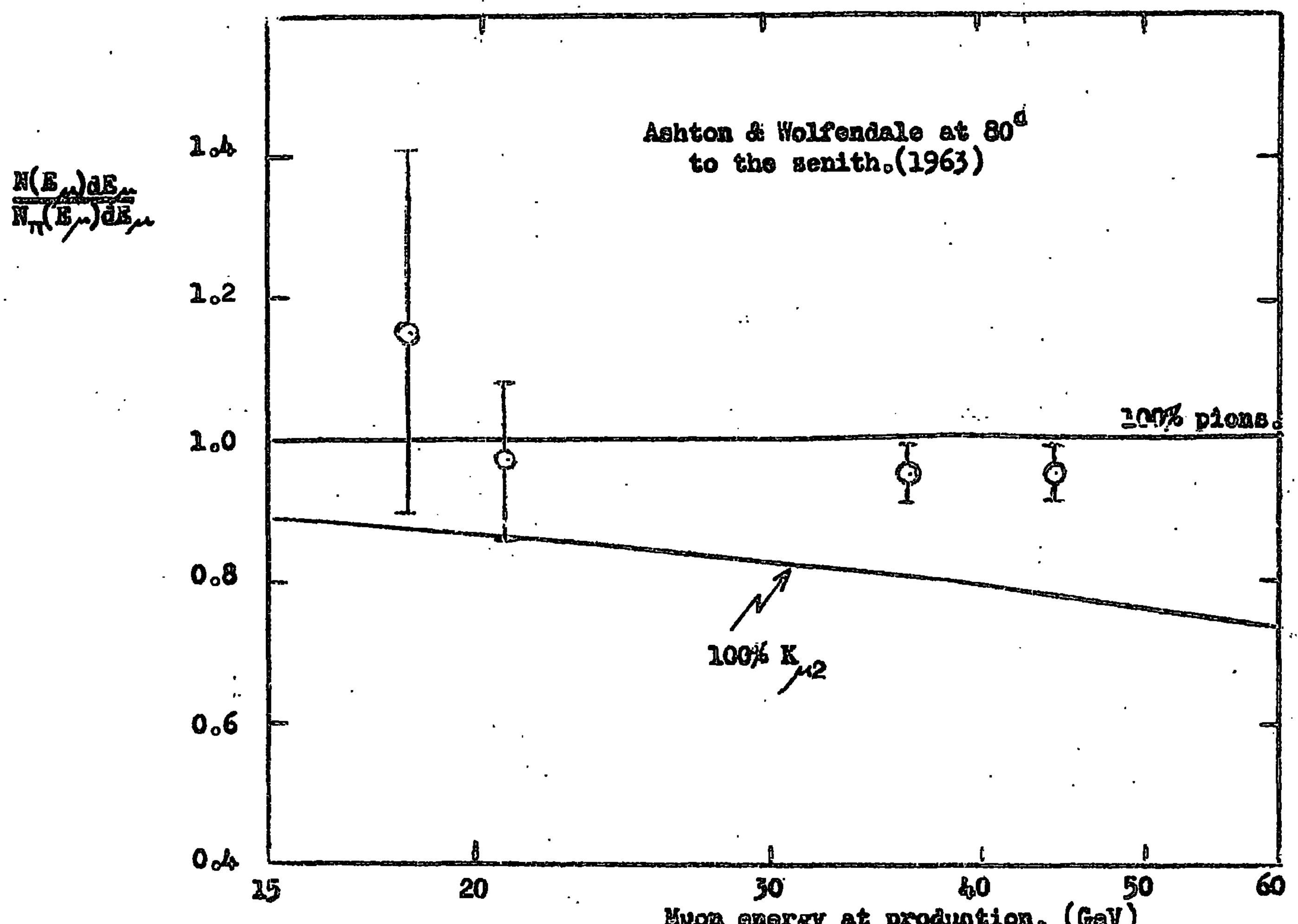

Fig. 6.6 The ratio of the measured muon intensities, at production, with the intensities expected for the case of pions only as the parent particles. (Also shown are the ratios of expected intensities for 100% $K_{\mu 2}$ origin only, and 100% pion origin only.)

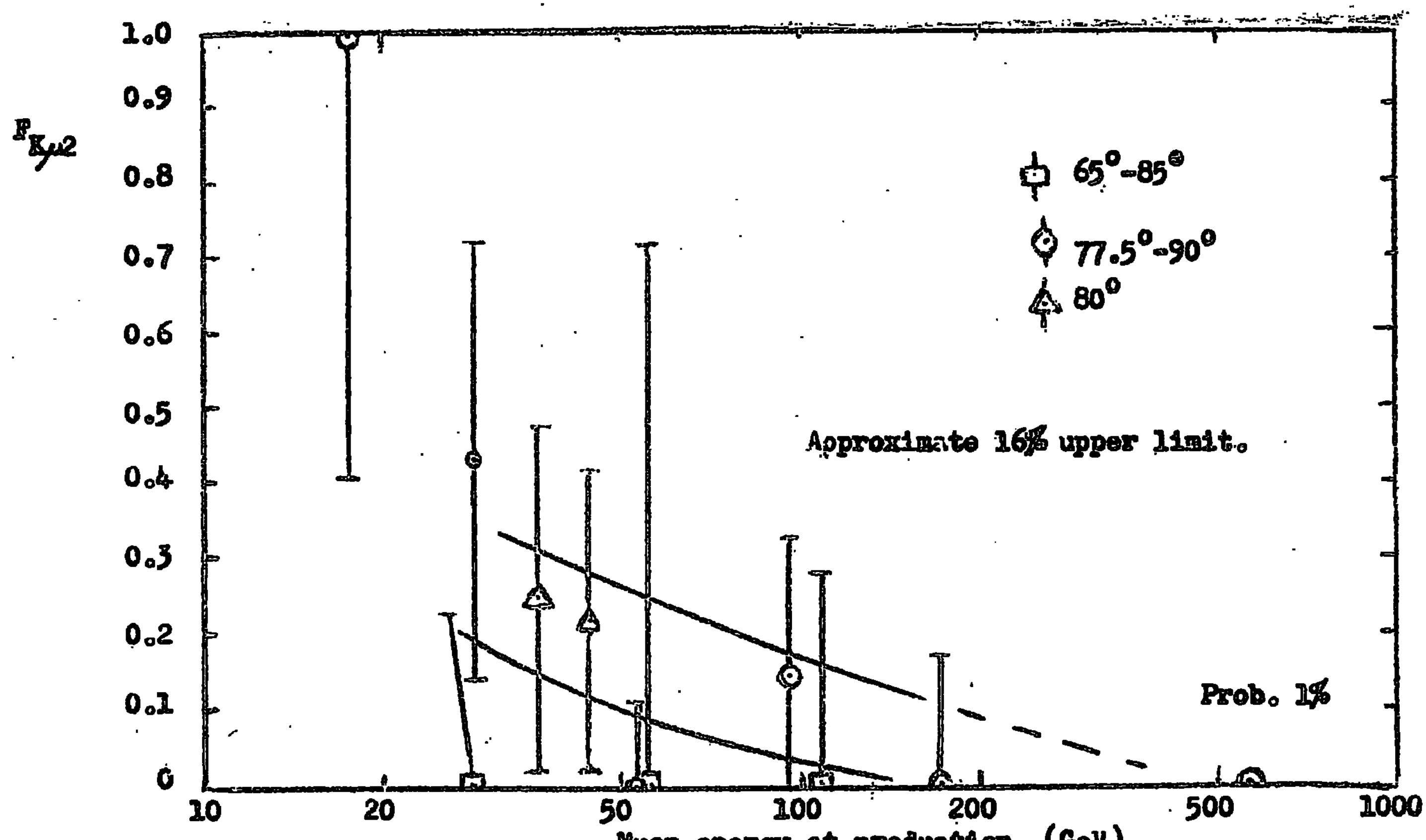

Fig. 6.7 The fraction, $F_{K\mu 2}$, of $K_{\mu 2}$-mesons giving rise to muons as a function of muon energy at production in the zenith angular range 65°-90°. (65°-85°, Allen & Apostolakis, 1961; 77.5°-90°, present experiment; 80°, Ashton & Wolfendale, 1963.)

have been combined and the ratio of the observed to expected intensities of muons at production. These results are presented in figure 6.8. (a summary of the ratios for the experiments at 80° and 65°-85° to the zenith is shown in table 5.6). The corresponding values of $F_{K\mu 2}$ are shown in figure 6.7.

It is clear that there is consistency between the values of $F_{K\mu 2}$ found in the various experiments, and a best estimate can be made from all the data taken together. The best curve through the points is given together with an estimate of the 16% upper limit (one standard deviation). The 16% lower limit clearly lies along the axis at $F_{K\mu 2} = 0$.

The upper limit can be transposed to a limit on the value of the K/π ratio for the case where all decay modes are considered, F_K. Although the relative frequencies of production of the other K-meson states ($K^+, K^-, K^0, \overline{K}^0$) is not accurately known it is considered that the ratio F_K will be more realistic than $F_{K\mu 2}$.

An approximate analysis has been made to convert the upper limit on $F_{K\mu 2}$ from figure 6.7 to an upper limit on F_K, and this is plotted on figure 6.9.

Comparison is also made in figure 6.9 with the values of F_K found in other experiments. The machine results are those of von Dardel et al. (1960) using 25 GeV protons from the CERN proton-synchrotron. The mean K/π ratio was found to be 0.1. Analysis of the results of polarization studies of muons by Bradt and Clark (1962) and Alikhanyan et al, (1962) yields a K/π ratio (0.538 ±

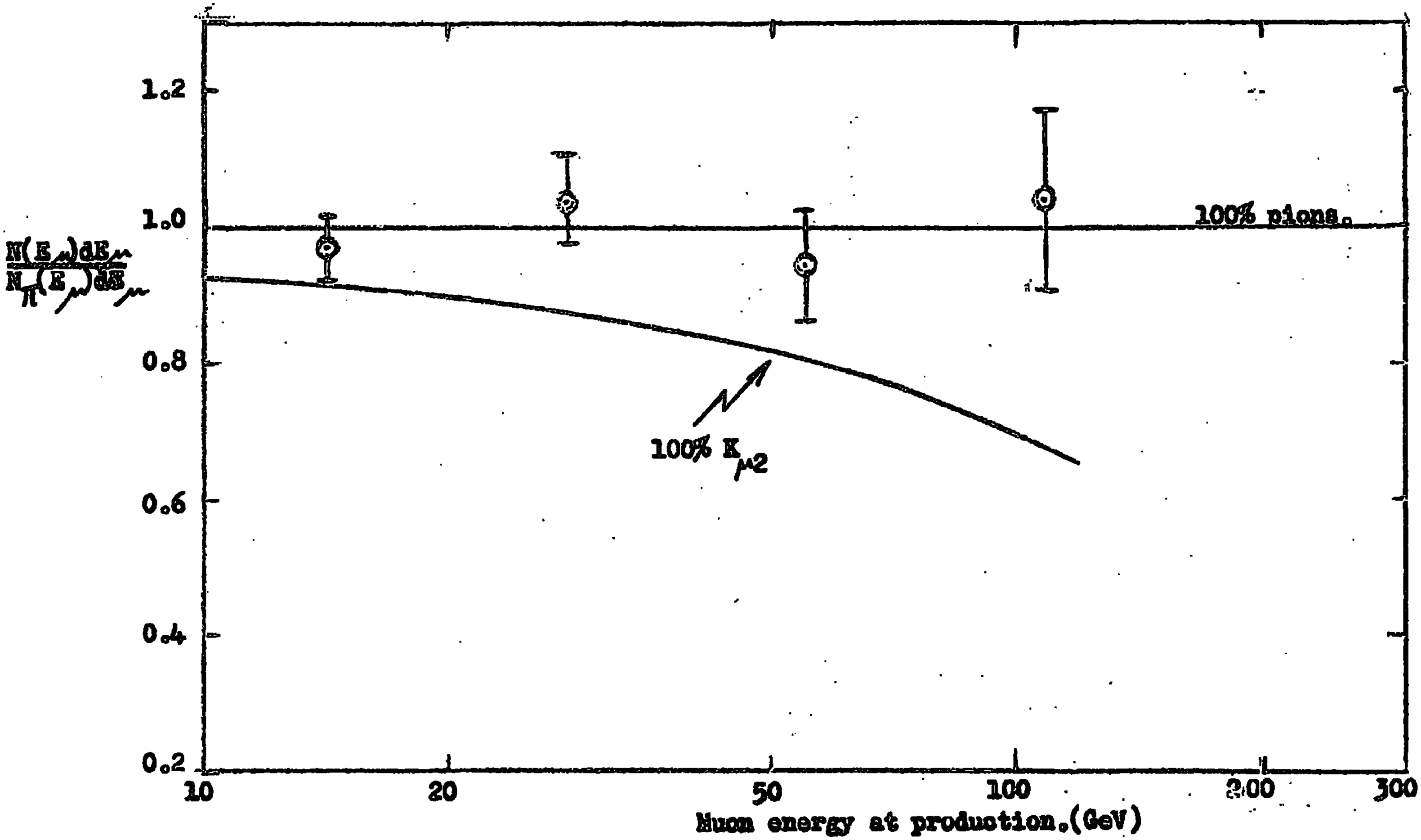

Fig. 6.8 The ratios of the measured muon intensities at production, with the intensities expected for the case of pions only as the parent particles in the zenith angular range 65°-85°, (Allen & Apostolakis, 1961). (Also shown are the ratios of the expected intensities for 100% $K_{\mu 2}$-meson origin only, and 100% pion origin only.)

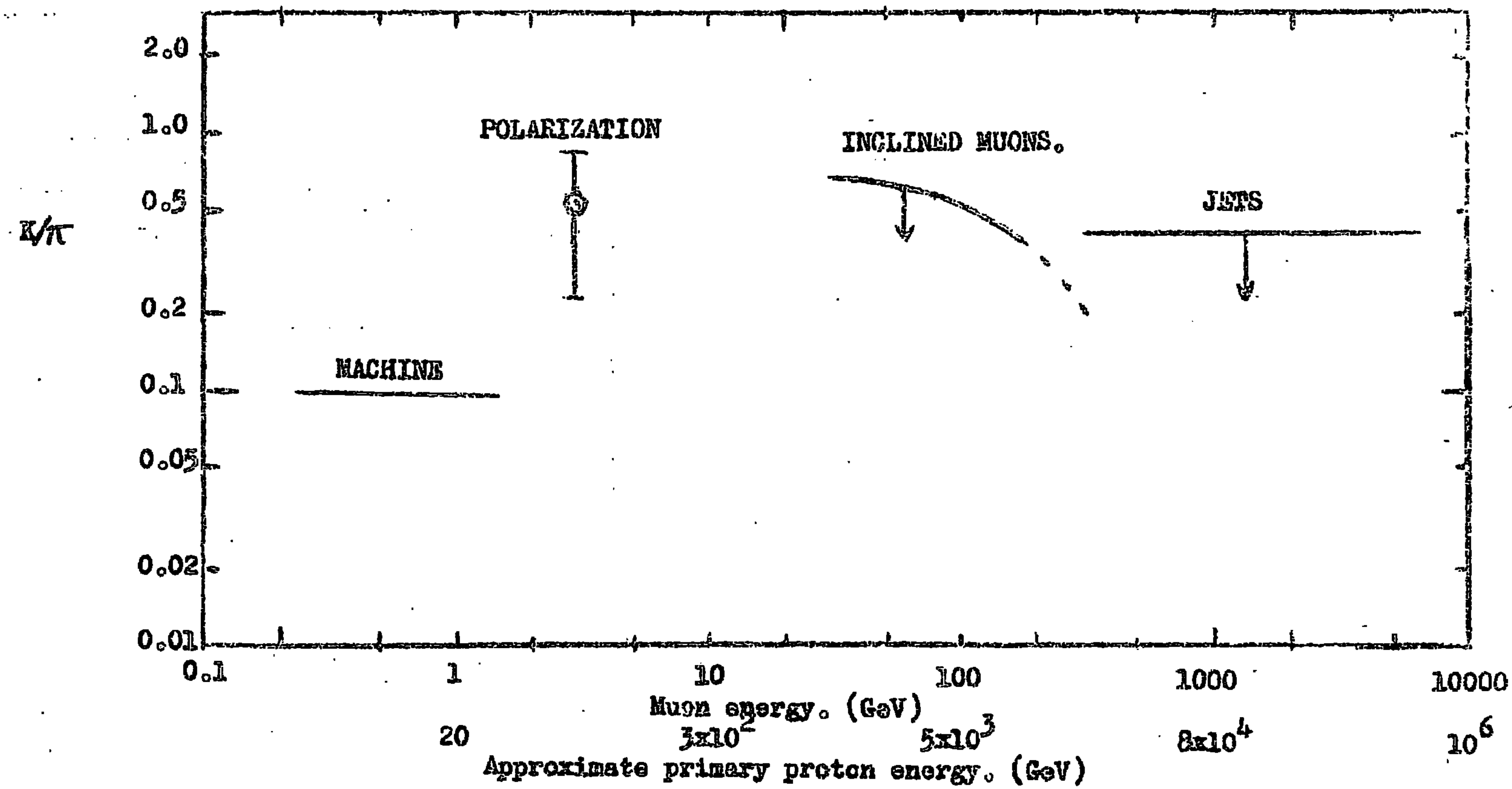

Fig. 6.9 The variation of the K/π ratio with energy.

0.310) for muons of mean energy 3 GeV (Osborne, private communication). At much higher energies studies of cosmic ray jets have shown that the K/π ratio is still comparatively low. Thus Bowler et al. (1962) find $K/\pi < 0.4$ for the range of energy of produced muons 300 - 7000 GeV.

In addition to the energy scale for the resulting muons an estimate is made of that for the primary protons.

The conclusion to be drawn is that there is no evidence to suggest a rapid increase in the K/π ratio with increasing proton energy. In particular, the studies on inclined muons show that the upper limit to the ratio is as would have been expected by interpolating between the results from polarization and jet measurements; thus there is clearly no pronounced maximum in the K/π ratio in the hitherto unexamined proton energy range 100 - 10,000 GeV.

Under the assumption of a constant K/π ratio over the proton energy range 50 - 10^6 GeV the data indicate the limits to be 0.23 - 0.40. It must be borne in mind, however, that the lower limit comes from the rather indirect polarization measurements and the actual K/π ratio could in fact be even lower than 0.23.

6.3 Conclusions

It has been shown that the application of neon flash-tubes to the magnetic spectrograph of Ashton and Wolfendale (1963) has resulted in an instrument capable of making more accurate momentum determinations. The instrument has potentialities not only for studying momentum spectra in greatly inclined directions but also for examining the local interactions of high energy muons.

The sea-level intensity spectra of muons incident at large zenith angles have been measured and compared with theoretical spectra under the assumption that pions only are the parent particles. Comparison has also been made with the expected production spectra of muons from the $K_{\mu 2}$ decay mode as well as from all muon-producing K-meson decay modes and it is found that there is no evidence for a large contribution to the muon flux at sea-level from particles other than pions.

A quantitative estimate of the ratio of the number of charged K-mesons to pions (of the same energy) produced in proton-air nucleus collisions has been made in the present work. It is found that the lower limit is effectively zero and the upper limit falls from 0.65 at a proton energy of 10^3 GeV to 0.2 at 2.10^4 GeV. Taken together with the results of other experiments it is clear that there is no evidence for a rapid increase in the K/π ratio over an energy range of primary protons extending from a few GeV to some 500,000 GeV; it is likely that the ratio is less than 0.4 over all energy ranges.

The measured charge ratio of muons shows consistency with the recent results of Hayman and Wolfendale (1962) although the statistical accuracy of the present experiment is low. The main conclusion is that the charge ratio does not tend to unity at least before several hundred GeV, indicating that the fluctuation in the multiplicity of high energy pions increases with increasing energy.

The type of experiment described in this thesis is important in that the conclusions about the K/π ratio are made with a minimum of assumptions about nuclear processes. In this respect it is superior to both the polarization studies and jet studies.

More extended measurements on both the inclined spectrum and the positive-negative ratio should enable closer limits to be put on the K/π ratio and an examination to be made of fluctuations in the multiplicity of produced particles at ultra-high energies. It is therefore important that the linear dimensions of the spectrograph be extended so that higher momenta can be determined.

The usefulness of the instrument as a source of very energetic muons has been demonstrated and experiments are being carried out at the present time to study the energy loss of these particles in a liquid scintillator. Further interaction experiments are being planned.

It is in this field that instruments similar to that described here are expected to reign supreme over particle accelerators for a long time to come.

Acknowledgments

The author wishes to thank Professor G.D. Rochester, F.R.S., for the facilities provided for the work and for his interest at all times.

It is with gratitude that the author thanks his supervisor, Dr. A.W. Wolfendale, for his continual guidance and help throughout the whole of this work. Further thanks are also extended to Dr. F. Ashton for his close co-operation and useful advice.

Other colleagues and members of the Staff of the Physics Department, in particular Dr. A.J. Apostolakis, Dr. P.J. Hayman and Mr. J.L. Osborne, are thanked for their advice and useful discussions.

The technical staff of the Physics Department, in particular Mr. P.J. Finley, Mr. E.W. Lincoln, Miss C.A. Guyll, Mrs. E.M. Graham, Mr. R. White and Mr. E. Nicholls, are thanked for their willing help and co-operation.

Miss P. Stewart has helped considerably with the typing of this thesis and her patient assistance is acknowledged with thanks.

Finally, thanks are expressed to the European Office, Aerospace Research, United States Air Force for financial support in the award of a Research Studentship throughout the period of the work.

References

Alikhanyan, A. L., Asatiani, T. L., Krishchyan, V. M., Matevosyam, E. M. and Sharkhatunyan, O. C., Proc. Int. Conf. on Cosmic Rays and the Earth Storm, Kyoto, 1961, J. Phys. Soc. Japan, (Suppl.AIII), 17, 304.

Allen, J. E. and Apostolakis, A. J., Proc. Roy. Soc. A265, 117, 1961.

Ashton, F., Brooke, G., Gardener, M., Hayman, P. J., Jones, D. G., Kisdnasamy, S., Lloyd, J. L., Taylor, F. E., West, R. H. and Wolfendale, A. W., Nature, 185, 364, 1960.

Ashton, F., O'Connor, P.V. and Wolfendale, A. W. U.S.A.F. Technical Note 3. 1961.

Ashton, F. and Wolfendale A. W. Proc. Phys. Soc. 81, 593, 1963.

Barrett, P. H., Bollinger, L. M., Cocconi, G., Eisenberg, Y. and Greisen, K. Rev. Mod. Phys. 24, 133, 1952.

Bennett, H. W. and Nash, W. F. Il Nuovo Cimento, Supp. 15, 193, 1959.

Bernardini, G., Conversi, M., Pancini, E., Serocco, E. and Wick, G. C. Phys. Rev. 68, 109, 1945.

Bowler, M., Duthie, J., Fowler, P., Kaddoura, A., Perkins, D. H., Pinkau, K. and Wolter, W. Proc. Int. Conf. on Cosmic Rays and the Earth Storm, Kyoto, 1961, J. Phys. Soc. Japan, (Suppl.AIII), 17, 424

Bradt, H. V. and Clark, G. W. Proc. Int. Conf. on Cosmic Rays and the Earth Storm, Kyoto, 1961, J. Phys. Soc. Japan, (Suppl. AIII), 17, 300.

Coates, D. W. and Nash, W. F. Aust. Journ. of Phys. 15, 420, 1962.

Conversi, M., Pancini, E. and Piccioni, O. Phys. Rev., 68, 232, 1945.

Coxell, H. Ph.D. Thesis (Durham) 1961.

Coxell, H., Scull, P. S. and Wolfendale, A. W. Proc. Phys. Soc. 81, 604, 1963.

von Dardel, G., Mermod, R. M., Weber, G. and Winter, K. Proc. 10th High Energy Nuclear Physics Conf., Rochester, 1960 (New York, Interscience), p.837.

Hayman, P. J. and Wolfendale, A. W. Proc. Phys. Soc., 80, 710, 1962.

Holmes, J. E. R., Owen, B. G. and Rodgers, A. L. Proc. Phys. Soc., 78, 496 and 505, 1961.

Jakeman, D. Canad. J. Phys. 34, 432, 1956.

Lloyd, J. L. and Wolfendale, A. W. Proc. Phys. Soc. A68, 1045, 1955.

Nash, W. F., Bull, R. M., Rastin, B. C. (Private communication, 1962).

O'Connor, P. V. and Wolfendale, A. W. Il Nuovo Cimento, Suppl.(2), 15, 202 1960.

Pak, W., Ozaki, S., Roe, B. P. and Greisen, K. Phys. Rev. 121, 905, 1961.

Perkins, D. H. CERN Conference on Very High Energy Phenomena (Geneva, CERN) 99, 1961.

Pine, J., Davisson, R. J. and Greisen, K. Il Nuovo Cimento 14, 1181, 1959.

Powell, C. F., Fowler, P. H. and Perkins, D. H. The Study of Elementary Particles by the Photographic Method, Pergamon Press Ltd., (1959).

Rossi, B. Nature, London, 128, 300, 1931.

Rossi, B. and Greisen, K. Rev. Mod. Phys. 13, 240 (1941).

Sheldon, W. R. and Duller, N. M. Il Nuovo Cimento X, 23, 63, 1962.

Sitte, K. Handbuch der Physik 46/1, 157, 1961. (Berlin, Springer).

Smith, O. L. and Duller, N. M. private communication (1962).